7-12-2014

The Effect of Dynamical Image Forces on The Transport Properties of Charge Carriers and Excitons in Metal-Semiconductor Nanostructures

Charles Cherqui

Charles Cherqui

Candidate

Physics

Department

This dissertation is approved, and it is acceptable in quality and form for publication:

Approved by the Dissertation Committee:

Dave Dunlap , Chairperson

Andrei Piryatinski

Wolfgang Rudolph

Hua Guo

The Effect of Dynamical Image Forces on The Transport Properties of Charge Carriers and Excitons in Metal-Semiconductor Nanostructures

by

Charles Cherqui

B.S., Loyola University Chicago, 2008

DISSERTATION

Submitted in Partial Fulfillment of the

Requirements for the Degree of

Doctor of Philosophy

Physics

The University of New Mexico

Albuquerque, New Mexico

May, 2014

Dedication

This thesis is dedicated to my wife, my sister, and my parents.

Acknowledgments

I would like to thank my advisers, Professor David Dunlap and Dr. Andrei Piryatinski, for their support and guidance. I would also like to thank Prof. Kenkre and Prof. Cahill for many thought provoking conversations throughout the years.

I would also like to acknowledge the financial support I received from the University of New Mexico, the Center for Nonlinear Studies at Los Alamos National Labratory and The New Mexico Consortium.

The Effect of Dynamical Image Forces on The Transport Properties of Charge Carriers and Excitons in Metal-Semiconductor Nanostructures

by

Charles Cherqui

B.S., Loyola University Chicago, 2008

PH.D, Physics, University of New Mexico, 2014

Abstract

We examine coupled metal nanoparticle/semiconductor hybrid nano-stuctures and analyze the effect that the surface response metal nanoparticles (MNP) has on the transport properties of the system. This analysis is accomplished by treating surface plasmons as quantum oscillators. We find that charge carriers traveling in the nearby semiconductors experience a repulsion due to the ground state energy of the quantum SP (QSP). This effect is shown to be the quantum analogue of the ponderomotive effect found in plasma physics. We then extend the theory to examine the transport properties of carbon nano-tube excitons in the presence of localized SPs and show that this system maps onto a Fano-Anderson Hamiltonian. Through numerical simulation, we show that the emission patterns of the system are severely modified by the presence of localized surface plasmons.

Contents

Chapter 1

Introduction

Understanding the dynamics of charge carriers and energy at the nano-scale has been the focus of an immense amount of research over the last few decades. Manufacturing capabilities of material scientists have improved to the point where researchers may design systems that had once been considered simple toy models, but are now realizable in a laboratory setting. This opens up the possibility to test novel effects that in the past had been discounted as unrealistic or washed out in an ensemble average. There is a need to reexamine our description of how objects and energy interact with matter in light of a new generation of precision instrumentation. Of interest to us are hybrid nano-structures consisting of metal nano-particles (MNPs) capable of carrying localized surface plasmons (LSP) and low dimensional semi-conductors, such as single-walled carbon nanotubes (SWNT) or quantum dots (QD). The aim of this thesis is to study low dimensional semi-conductors coupled to MNPs.

The understanding of how charge carriers interact with metal surfaces has a long history that reaches back to the earliest days of physics. From a modern perspective, the study of these types of interactions has its roots in the theory of bulk plasmons by Bohm and Pines formulated in the early 1950's [PB52, Pin56] . Bulk plasmons are the quanta of the collective oscillation of a many body interacting electron gas. They are

a consequence of electron screening effects, which make electrons blind to each other in the short range, but leave a residual long range interaction. This long range part of the coulomb force leads to a collective mode of the system [PB52, Pin56]. Another type of plasmon mode appears when the electron gas is bounded by a surface. The effect of the surface on the electron system is to also allow for the excitation of electron density waves on the surface. As it turns out, these surface modes often dominate the electromagnetic response of a metal. Their quanta are called surface plasmons (SP). They can propagate or become localized, depending on the material and its geometry. Since they were theoretically predicted by Ritchie in 1957 [BRB55], SPs have had a far reaching effect in the theoretical modeling, prediction, and execution of experiments in the fields of condensed matter and surface physics.

Ritchie invoked the notion of SPs in order to explain the quantization of the energy-loss spectra observed when passing a beam of low energy electrons through a thin metallic foil [BRB55]. He based his theory on the prior work of Pines and Bohm [PB52, Pin56] on bulk plasmons. Their theory, outlined in a set of four seminal papers, was successfully used to explain experiments on the interaction of fast electrons with metal films [Rut48, Rut42]. Ritchie extended this work to include surface effects [Rit57]. Experimental verification of the existence of SPs came only a few years later from a series of experiments by Powell and Swan [PS59a, PS59b], who found definitive proof of their existence and subsequently gave them their name [SF60].

Ever since their discovery, SPs have played an important role in the understanding of the fundamental properties of solid state matter. They have been used to explain the nature of van der Waals forces [Ger71], energy loss spectra of electrons moving past a metal surface [ERBI81, SOF67, BH70, Pow68], image potential states [EU91], and the enhancement of energy transfer between molecules [CPS78]. They have also been successfully used to model low energy electron diffraction [NEC70] and to determine the thickness of thin films [Sta70]. In the early days of the field,

many experiments focused on proving the existence of SPs in a variety of materials [MML$^+$69, JS69], but potential applications of the discovery did not take long to materialize. Of particular importance was the prediction [Fer58] and the subsequent observation [SS69, ER70] of radiating SPs on planar surfaces. This discovery, combined with further experiments [HB70] and theory [RACH68], explored the interaction of light with surface modes on rough surfaces and gratings, and led to the design of measurement devices based on the effect [Rae67].

This set the groundwork for the field known today as plasmonics [Sto11], a field that has enjoyed a golden age due to the development of nanoscale manufacturing capabilities. The resonant driving of SPs by an external electric field, usually in the form of a laser, has allowed for the sustained creation of highly localized intense electric field amplitudes near metal surfaces. These field enhancements, known as hotspots, are used to magnify a variety of resonance phenomena. The field of plasmonics, which is just an extension of SP theory, has been responsible for some of the most exciting advancements in nanoscale physics. The enhancement of Raman scattering by resonantly driven SPs has made it possible to probe single molecules [KWK$^+$97, NE97, GN80, TKB79]. SPs have been exploited to create SP lasers (spasers), which excite coherent near field radiation in a manner that is completely analogous to a traditional laser [GZ13, Gat12, Sto08]. Also, since the SP resonance condition occurs for negative values of the dielectric constant in most metals, it is possible to create materials with a negative index of refraction, leading to novel effects such as an induced transparency in metamaterials [NLON09, ZGW$^+$08, HLO07, AE05]. The effective plasmonic response of an assembly of nanoparticles has also been used to create optical frequency magnetic fields [AD12, LLL$^+$09, LWM$^+$09]. For more information, we refer the reader to the many books and review articles that survey the advancements of this rapidly evolving field [Mai07, Sto11].

We will explore both resonant and non-resonantly driven SPs and study their

subsequent effect on the transport properties of energy and charge carriers in coupled semiconductors nanosystems. The motivation for studying non-resonantly driven effects is based on recent advances in nano-mechanical/electronic device fabrication [MKZ+08, Cle03] and force measurement techniques capable of mapping out the charge distribution in an individual molecule [MGMM12]. In these systems, slow dynamics in the presence of high frequency SPs can play an important role. Central to understanding these systems is the image force and its relation to the response function of the plasmonic system [Mah12, Mah10, MPP86]. The interaction of SPs with the charge carriers of nearby semiconductors leads to a dynamical back and forth interaction that can be difficult to analyze. Generally, the approach has been to treat SPs classically. This is in spite of the fact that the quantum nature of SPs was addressed in the first few decades of the theory [Boy68, CA74, LŠ76, Bar77, Das77, HB80, Hal86]. Over time it was found that a semi-classical description of SPs was adequate to describe experiment and the quantum nature of SPs was mostly abandoned in everything but the name, which still carried the suffix of a quantum quasi-particle. But the growth of nanotechnology in recent years has ushered in a new generation of experiments that indicate a need for a quantum theory of SPs [Kum13, TMÖ+13, LTLL12, MKN+12, SMNG12, VAP+12, JS11, Sto11, RDSF+10, ZPN10]. Part of this is due to the ability of modern day researchers to design simple nanoparticle systems that at one time could have only existed in a large ensemble setting, if at all. More than 40 years have passed since the first work on quantum SPs was carried out, and the work presented here is part of a growing trend to re-examine, test, and often re-discover the theory. In this thesis, we provide a unique approach to this problem that differs from others found in the literature. This is used to explore the dynamics of simple systems with a unique set of parameters afforded to us by current nano-manufacturing technology. This allows us to gain insight into plasmonic systems and predict novel effects that have yet to be observed.

This thesis has the following layout. Chapter 2 reviews the basics of SPs in the

near field. We calculate properties of plasmons for a few geometries of interest to theorists and experimentalists. In Chapter 3, we discuss Förster energy transfer in the presence of localized SPs between neighboring QDs. This will provide an overview of the field of plasmonics and allows us to familiarize ourselves with the nature of localized SP modes on metal nanoparticles (MNPs). This sets the stage for Chapter 4, where we formally develop a self-consistent dynamical image response theory for a charge moving above a semi-infinite metal slab. In Chapter 5, we study the motion of a charge carrier confined to a carbon nanotube and explore the classical and quantum dynamical image force interaction between it and a MNP. We derive an expression for a quantum correction to the classical electrostatic image force by using a time independent adiabatic decoupling scheme based on the use of canonical transformations. We explore the consequences of these quantum corrections and discuss their classical analogue as a means of building intuition. Chapter 6 examines exciton dynamics in a single-walled carbon nanotube (SWNT) coupled to a Ag metal tip. We report a general theoretical approach to study exciton transport and emission in a SWNT in the presence of a localized SP. We derive a set of quantum mechanical equations of motion along with approximate rate equations to account for the exciton, SP, and environment degrees of freedom. For this system, we find that the radiation distribution is dominated by SP emission.

Chapter 2

Surface Plasmons Resonance

2.1 Introduction

In this Chapter, we will provide a short review of SP theory and derive some basic quantities that will be used in later chapters. We will derive the SP polariton dispersion relation, obtain an expression for the Drude-Lorentz response functions, and calculate the localized SP modes for a select set of geometries of special interest.

2.2 Dielectric Response Functions

We will begin by deriving the classic expression for the frequency-dependent relative permittivity of a metal. Much of the behavior of elementary and collective excitations in solids can be modeled by a linear harmonic oscillator, and the approach found here can be found in any good textbook on the subject [JF99, SDMT98]. First, we derive the relative permittivity of a polarizable media through the use of the Lorentz model. Then we will introduce the Drude model of metals and briefly discuss its limitations in correctly describing the characteristics of metals.

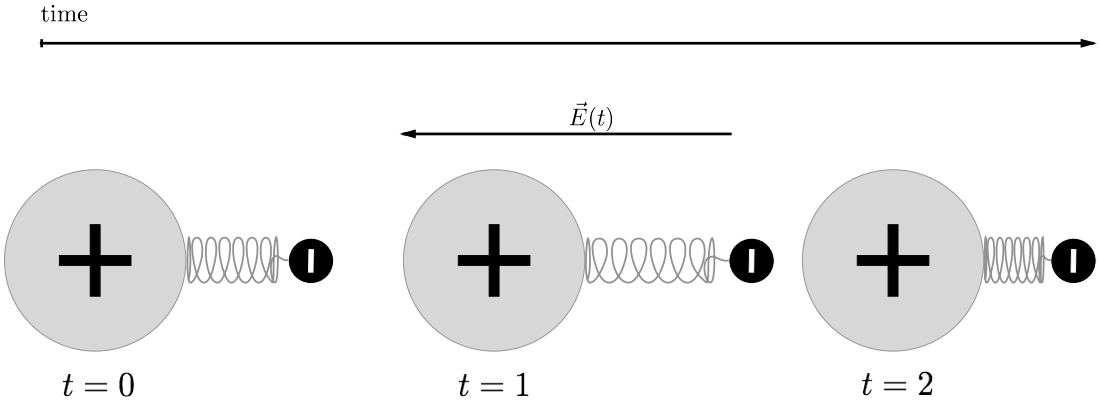

Figure 2.1: The Lorentz model of an atom under the influence of an electromagnetic pulse. At $t = 0$ the oscillator is at rest about its equilibrium. At $t = 1$, a perturbing electric field is turned on and the electron is forced in the opposite direction of the applied field. At $t = 2$, the field is turned off and the electron is brought back to equilibrium by the restoring force of the spring, but due to its inertial mass, it overshoots its mark. In the absence of damping this oscillation would continue indefinitely.

2.2.1 Lorentz Model

In the Lorentz model of dielectric response, the solid is treated as a fine-grained assembly of non-interacting molecular oscillators. Each oscillator, with spring constant k, is meant to represent an electron bound to a positive ion.

Let us now focus our attention on the dynamics of a single oscillator. We are interested in how the system responds to external forces and therefore want to analyze the following equation,

$$m\ddot{x} + B\dot{x} + kx = F(\boldsymbol{r}, t). \tag{2.1}$$

Here, m is the mass of the electron, k is the spring constant, B is the damping coefficient, and x the displacement of the electron about equilibrium.

If the driving term on the rhs of Eq. (2.1) is taken to be an electric field then the dipole moment of the atom is,

$$\ddot{p} + \omega_0 p + \gamma \dot{p} = \frac{e^2}{m} E(\boldsymbol{r}, t) \tag{2.2}$$

where $p = ex$ is the dipole moment of the atom and ω_0 is its natural frequency, and γ is the damping coefficient. The total polarization per unit volume is,

$$P = nP, \tag{2.3}$$

where n is the number of atoms per unit volume. Taking a Fourier transform and solving for P gives,

$$P(\omega) = \frac{ne^2}{\varepsilon_0 m} \frac{1}{(\omega_0^2 - \omega^2 - i\omega\gamma)} E(x, \omega) = \chi(\omega)\varepsilon_0 E(\boldsymbol{r}, \omega) \tag{2.4}$$

where $\chi(\omega)$ is the relative electric susceptibility. Thus the dielectric constant is,

$$\varepsilon(\omega) = (1 + \chi(\omega)) = 1 + \frac{\omega_p^2}{(\omega_0^2 - \omega^2 - i\omega\gamma)} \tag{2.5}$$

where $\omega_p = \sqrt{\frac{ne^2}{\varepsilon_0 m}}$ is the plasma frequency.

2.2.2 Drude Model

The dielectric constant of a metal can be obtained by simply taking the limit of $\omega_0 \to 0$ in Eq.(2.5). However, it is illustrative to derive the response of a metal from the perspective of a free electron gas. Following a standard textbook approach [AM05], we assume that the valence band electrons constitute a non-interacting gas and electrons except for when they infrequently scatter off an ion or another electron. We subject our system to an external driving force to quantify the response, and write down an equation for electron's average momentum $m^* < \mathbf{v} >$,

$$m^* < \dot{\mathbf{v}} > + m^* \gamma < \mathbf{v} > = F(\boldsymbol{r}, t). \tag{2.6}$$

Since $\gamma = 1/\tau$ is due to collisions, reciprocal of the rate, τ, characterizes the time between collisions. In Fourier space the current density is,

$$\mathbf{j} = ne < \mathbf{v} >= \frac{ne^2}{m^*}\frac{\tau E(\boldsymbol{r})}{1 - i\omega\tau} = \sigma(\omega)E(\boldsymbol{r}). \tag{2.7}$$

In Eq. (2.7) we have introduced the electrical conductivity,

$$\sigma(\omega) = \frac{\sigma_0}{1 + i\omega\tau} = \frac{\sigma_0}{1 + \omega^2\tau^2} - i\omega\tau\frac{\sigma_0}{1 + \omega^2\tau^2} \tag{2.8}$$

where $\sigma_0 = \frac{ne^2\tau}{m^*}$.

In the limit of $\tau \to \infty$, the response of free non-interacting electrons is entirely characterized by the mass. Inserting the current density Eq. (2.7) into Eq. (2.6), we can solve for the polarization per unit volume,

$$\mathbf{P} = -ne\mathbf{x} = -\frac{ne^2}{m^*\omega^2}\mathbf{E} \tag{2.9}$$

leading to the Drude dielectric function,

$$\varepsilon(\omega) = 1 - \frac{\omega_p^2}{\omega^2}. \tag{2.10}$$

The oscillator model is useful in describing many of the properties of solids and can easily be modified to create a qualitative and often quantitative description of a number of the elementary properties of solid state systems. But they are not without limitation. Let's reflect on some of the approximations made in the Drude model of metals. Central to the Drude model is the assumption of a free electron gas. Given the strength of Coulomb repulsion between like charges, it might seem unlikely that a model that simply ignores them would provide an accurate description of a metal. Surprisingly, this is the case as long as the system's response to external perturbations is linear. For example, the Drude model correctly predicts that metals reflect light at frequencies below ω_p.

To understand why this model is so successful requires a microscopic description of metals, such as the "quasiparticle" picture of Landau's Fermi liquid theory [NP58]

or the more comprehensive techniques of quantum field theory [Mah00]. The Drude model fails when features such as inter-band transitions or electron electron correlation become important. In such a case, the Drude model will not suffice and must be modified or replaced with a quantum mechanical treatment of the dielectric function [KMK89].

2.2.3 Experimental Data for Dielectric Response

The Drude model fits the optical response of metals quantitatively, but in many cases experimental data deviates significantly from its predictions. This is particularly true of gold. Gold is a favorite material for nano-particle synthesis due to the fact that it's easy to manipulate and resistant to effects such as oxidation [WIN$^+$10]. Unfortunately, the effects of inter-band transitions are particularly pronounced around the SP resonance. This not only means that a SP will have a shorter lifetime, but also that other energy loss channels are enhanced when the system is resonantly driven. This conspires to reduce the near field enhancements that are at the heart of plasmonics, and much effort is spent to either avoid, or exploit this behavior. In many cases, the Drude model can simply be expanded to include a new set of oscillators that model inter-band transitions. Alternatively, experimental data for the dielectric function exists for most materials in the visible range [JC72], the data can be tabulated and used as a look-up table for the purposes of modeling. Figures 2.3 and 2.2 show experimental data taken by Johnston and Christy [JC72] compared to the Drude model.

2.3 Surface Plasmons

In this section we derive the SP modes for a few geometries of special interest. We also review the basic theory of SPs. We begin with a classical description of SP

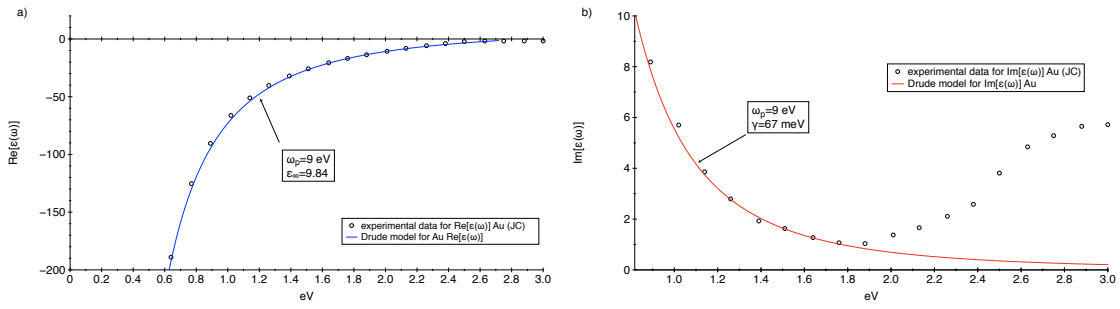

Figure 2.2: Johnston and Christy experimental data compared to Drude model for Au. The blue line is $RE[\varepsilon(\omega)]$ and the red curve is $IM[\varepsilon(\omega)]$ as a function of frequency. Gold is poorly described by the Drude model in the optical range since inter-band transitions begin to play an important role at these energies.

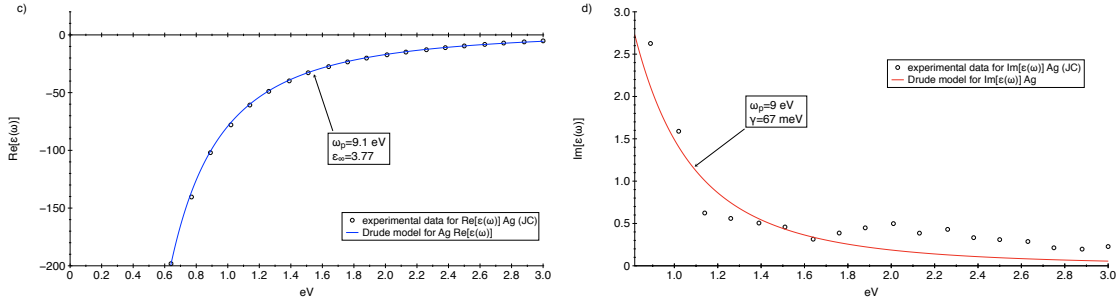

Figure 2.3: Johnston and Christy experimental data compared to Drude model for Ag. The blue line is $RE[\varepsilon(\omega)]$ and the red curve is $IM[\varepsilon(\omega)]$ as a function of frequency.

polaritons.

2.3.1 SP Polaritons

The systems we are concerned with here, and in later chapters, are smaller than the wavelength of light at the SP frequency (visible). This allows us to perform our calculations in the quasi-static near field approximation, which neglects the delay effects due to the speed of light. In order to justify the use of this approximation, we begin by deriving the energy dispersion relation for SP polaritons (SPP). The derivation

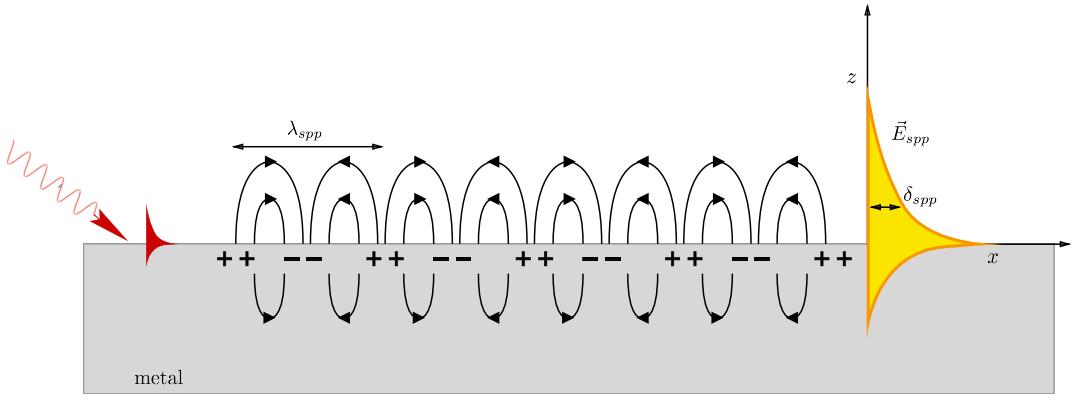

Figure 2.4: Schematic of a SP polariton (SSP). The gray slab represents a semi-infinite metal slab surrounded by air. The red arrow on the left indicate the exciting field; since electromagnetic radiation can not excite SPP's something must be done to an incoming source to create an evanescent wave at the surface. Once the SPP is excited, it propagates some distance forward with an electric field that has exponential tales inside and outside of the metal. Outside the surface the field is highly localized leading to intense near fields. As the wave propagates forward it induces a polarization of the matter underneath it. When the wave passes by, the charge distribution grows to a maximum value and undergoes under-damped harmonic motion.

presented here can be found in the review article by Pitarke et al. [PSCE07].

Consider a system consisting of two semi-infinite dielectric slabs that are pressed against each other, creating an interface at $z = 0$. Maxwell's equations for this system are,

$$\nabla \times \mathbf{H}_i = \frac{\varepsilon_i}{c}\frac{\partial}{\partial t}\mathbf{E}_i \tag{2.11}$$

$$\nabla \times \mathbf{E}_i = -\frac{1}{c}\frac{\partial}{\partial t}\mathbf{H}_i \tag{2.12}$$

$$\nabla \cdot (\varepsilon_i \mathbf{E}_i) = 0 \tag{2.13}$$

$$\nabla \cdot \mathbf{H}_i = 0 \tag{2.14}$$

where $i = 1, 2$, depending on which medium we are in. The solutions to this set of equations are propagating waves.

These waves represent the bound oscillations of an electron density at the interface. In order for these modes to exist on the surface they must be transverse, meaning that some component of the electric field must be normal to the interface. This, combined with the knowledge that SP modes have a characteristic exponential decay of the electric field for $z \pm 0$, inspires us to write down the following ansatz for the electric and magnetic fields;

$$\mathbf{E}_i = \mathbf{E}_0 e^{-k_i|z|} e^{q_i x - \omega t} \tag{2.15}$$

$$\mathbf{H}_i = \mathbf{H}_0 e^{-k_i|z|} e^{q_i x - \omega t}. \tag{2.16}$$

Here, $\mathbf{E}_0$ and $\mathbf{H}_0$ are the polarization vectors for the electric field polarized perpendicular to the interface and the magnetic field polarized parallel to it. Plugging these back into Eq. (2.11) gives,

$$ik_1 H_1^y = \frac{\omega}{c}\varepsilon_1 E_1^x \tag{2.17}$$

$$ik_2 H_2^y = -\frac{\omega}{c}\varepsilon_2 E_2^x \tag{2.18}$$

$$k_i = \sqrt{q_i^2 - \varepsilon_i \frac{\omega^2}{c^2}} \tag{2.19}$$

When combined with the usual boundary conditions, these lead to set of equations for the magnetic field:

$$\frac{k_1}{\varepsilon_1} H_1^y = \frac{k_2}{\varepsilon_2} H_2^y \tag{2.20}$$

$$H_1^y = H_2^y \tag{2.21}$$

$$q_1 = q_2 = q. \tag{2.22}$$

This system can only be satisfied if

$$\frac{\varepsilon_1}{k_1} = -\frac{\varepsilon_2}{k_2}, \tag{2.23}$$

which gives us the condition for the existence of SP polaritons. Imposing this condition on Eq. (2.19) allows us to write down the dispersion relation,

$$q = \frac{\omega}{c}\sqrt{\frac{\varepsilon_1\varepsilon_2}{\varepsilon_1+\varepsilon_2}}. \tag{2.24}$$

Let us take region 1 to be a metal described by the Drude model Eq. (2.10) and region 2 to be the vacuum. Inserting Eq. (2.10) into Eq. (2.26) gives,

$$\omega^4 - \omega^2(\omega_p^2 - 2c^2q^2) - c^2q^2\omega_p^2 = 0, \tag{2.25}$$

which when solved for ω^2 is,

$$\omega^2(q) = \frac{\omega_p^2}{2} + c^2q^2 \pm \sqrt{c^4q^4 + \frac{\omega_p^4}{4}}. \tag{2.26}$$

This is the retarded SPP dispersion relation. Where the $\pm$ sign in the expression is for the upper and lower branch of the dispersion relation. The dispersion relation is plotted in Fig.(2.5). The upper curve is polariton branch and the bottom curve is the SP branch. We have chosen ω_p to be 15 eV, a typical value for metals. When q is low, the SPP hugs the light line (dashed diagonal line) and behaves like a photon. It propagates at high group velocities along the surface, but does not radiate since there is still a momentum mismatch between it and the upper branch. The horizontal dashed line is the SP line that bounds the bottom band of the dispersion curve. In the limit that for $q >> \omega_{sp}/c$ we approach the dispersionless SP limit of $\omega_p/\sqrt{2}$ This is a standing wave and not a propagating wave. Figure 2.4 shows a schematic of the SPP excitation mechanism.

2.4 The Quasi-Static Approximation

Almost all the systems of interest in this thesis are localized to distances within a wavelength of optical light. In this limit we can neglect delay effects due to the speed of light and only consider delay due to the inertial response of the metal.

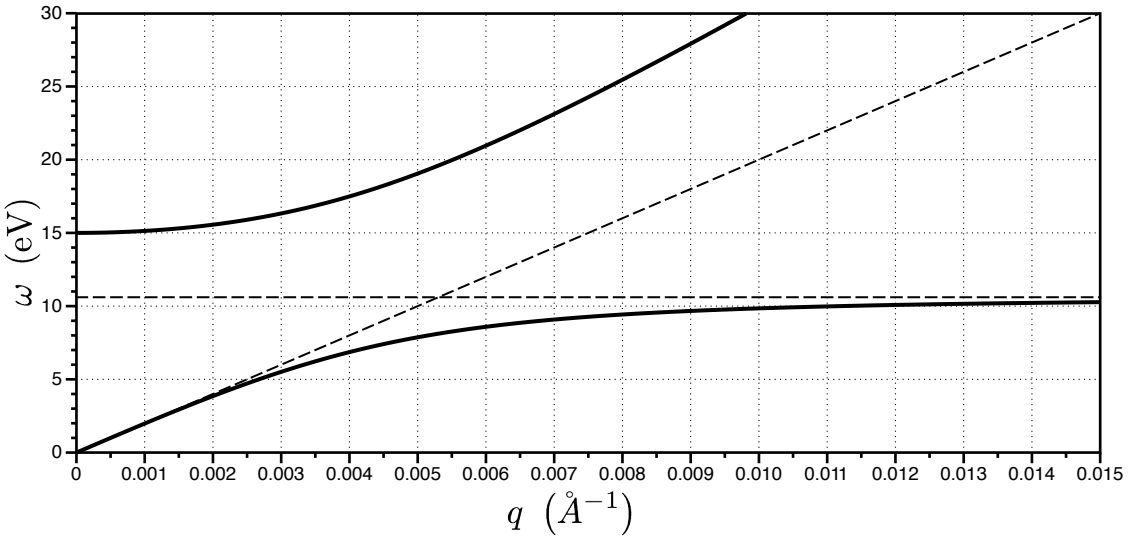

Figure 2.5: SP polariton dispersion relation plotted as a function of wave vector q.

This is known as the quasistatic approximation [KF74]. All information about the dispersionless limit of SPs can be obtained by solving the time dependent Poisson equation in frequency space. We solve for the Green function by solving the Poisson equation with a delta function describing the location of a moving point charge,

$$\boldsymbol{\nabla} \cdot \int_{-\infty}^{t} dt' \tilde{\varepsilon}\,(t-t')\,\mathbf{E}\,(\boldsymbol{r},\boldsymbol{r}',t') = e\delta(\boldsymbol{r}-\boldsymbol{r}'(t)), \tag{2.27}$$

or by noting the relation between the electric field and the potential, $\boldsymbol{E} = -\boldsymbol{\nabla}\phi$ we may recast this equation,

$$\boldsymbol{\nabla} \cdot \int_{-\infty}^{t} dt' \tilde{\varepsilon}\,(t-t')\,\boldsymbol{\nabla}\phi\,(\boldsymbol{r},\boldsymbol{r}',t') = e\delta(\boldsymbol{r}-\boldsymbol{r}'(t)), \tag{2.28}$$

Transforming into frequency space we get,

$$\boldsymbol{\nabla} \cdot \varepsilon(\omega)\boldsymbol{\nabla}\phi(\boldsymbol{r},\boldsymbol{r}',\omega) = e\mathcal{F}[\delta(\boldsymbol{r}-\boldsymbol{r}'(t))], \tag{2.29}$$

where $\mathcal{F}$ is the formal Fourier transform of the δ-function. In the discussion that follows, we will be solving this equation for some simple systems. In the context of these examples we will introduce the Green function notation and how its singularity structure is connected to the existence of SP modes on the surface of MNPs.

Planar SP Modes

The first example we consider is the case of a charge moving above a dielectric slab. We begin with the electrostatic solution for a charge placed in above a dielectric slab s depicted in Fig.2.6.

We know that when a negative charge distribution is placed above a dielectric slab, the presence of the charge causes a reorganization of the molecules in the dielectric. To find the Green function we follow the standard image approach [SDMT98]. This allows us to uniquely solve the problem by finding the image charge distribution inside the plane which correctly mimics the boundary conditions at the surface. When the location and weight of the image is properly characterized, the principle of superposition allows us to write down the complete solution. We will refer to the charge distribution above the plane as the source and the one below as the image. Figure 2.6 shows a schematic of the method of images method for a charge above a plane.

We begin by placing a single source charge q', a distance z' above the slab, and an image charge q, a distance z inside the dielectric. As an ansatz, we take the potential to be,

$$\varphi = \frac{1}{4\pi\varepsilon_0}\left(\frac{q'}{R'} + \frac{q}{R}\right) \quad , z' > 0 \tag{2.30}$$

$$\tag{2.31}$$

above the slab to be the superposition from two point charges, as is R and R'. Applying the usual boundary conditions, we find that;

$$q = -\frac{\varepsilon_2 - \varepsilon_1}{\varepsilon_2 + \varepsilon_1} q' \tag{2.32}$$

$$z = z' = d \tag{2.33}$$

$$R' = \sqrt{x^2 + y^2 + (z-d)^2} \tag{2.34}$$

$$R = \sqrt{x^2 + y^2 + (z+d)^2}, \tag{2.35}$$

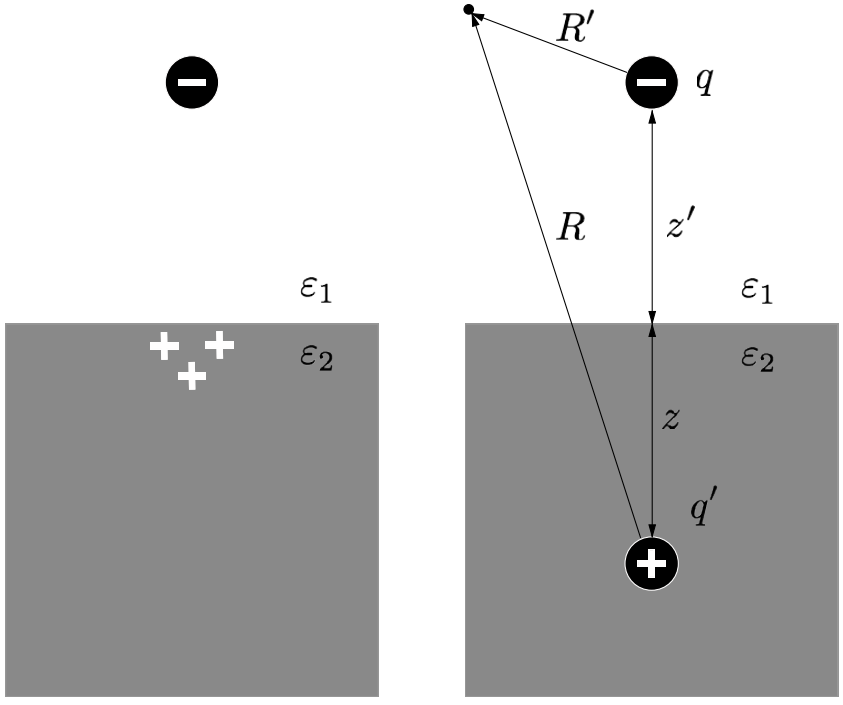

Figure 2.6: Method of images for a dielectric slab. The left constitutes a "realistic" schematic of the polarization of the matter underneath the charge. The right hand side is the image problem we solve in its place. $R' = \sqrt{x^2 + y^2 + (z-d)^2}$ is the location of the source charge q', and $R = \sqrt{x^2 + y^2 + (z+zd)^2}$ is the location of the image charge q.

Here, ε_1 is the relative permitivitty outside the slab, and ε_2 is the relative permitivitty inside. Thus, the total electric potential is the sum of the potentials of the source charge and its image.

$$\varphi = \frac{q}{4\pi\varepsilon_0}\left(\frac{1}{R'} - \frac{\varepsilon_2 - \varepsilon_1}{\varepsilon_2 + \varepsilon_1}\frac{1}{R}\right) \quad z' > 0 \tag{2.36}$$

Introducing dynamics in the quasi-static limit, we make the following substitution;

$$\varepsilon_2 = \varepsilon(\omega) \tag{2.37}$$

Thus the total potential is,

$$\varphi(R, R') = \frac{q}{4\pi\varepsilon_0}\left(\frac{1}{R'_1} - \frac{\varepsilon(\omega) - \varepsilon_1}{\varepsilon(\omega) + \varepsilon_1}\frac{1}{R_1}\right) \quad z' > 0. \tag{2.38}$$

To introduce the Green function we recast Eq. (2.38) into the form,

$$\frac{q}{4\pi\varepsilon_0}G(R,R') = \frac{q}{4\pi\varepsilon_0}\left(G_0(z-d) - g(\omega)G_0(z+d)\right) \quad z' > 0. \tag{2.39}$$

where we have defined,

$$G_0(\boldsymbol{r},\boldsymbol{r}') = \frac{1}{\sqrt{(x-x')^2+(y-y')^2+(z-z')^2}}. \tag{2.40}$$

and,

$$g(\omega) = \frac{\varepsilon(\omega)-\varepsilon_1}{\varepsilon(\omega)+\varepsilon_1}. \tag{2.41}$$

Here, $G_0(\boldsymbol{r},\boldsymbol{r}')$ is proportional to the solution of Poison equation of point charge in free space, and $G(\boldsymbol{r},\boldsymbol{r}')$ is the total Green function for the charge placed outside the dielectric slab. In this form we see that the source and image charge are related by a proportionality factor $g(\omega)$; this factor is called the response function. The singularity structure of the response function defines the bound state eigenspectrum of the nanoparticle. To understand why this is the case, recall how the SP dispersion relation in Eq. (2.24) was derived. We assumed a surface wave solution to Maxwell's equations and then determined what conditions needed to be satisfied for that solution to exist. Bound states correspond to oscillation that remain after the passing of a delta-function impulse. These are the solutions for which $G(\boldsymbol{r},\boldsymbol{r}')$ is finite even while $G_0(\boldsymbol{r},\boldsymbol{r}') \to 0$. This can only happen if $g(\omega) \to \infty$, and this will only be the case if ω corresponds to a pole [Mor81]. Response functions play a central role in understanding SP's and will be used extensively throughout this thesis.

For the form of the response function in Eq. (2.41), we find that the SP frequency for $\varepsilon_1 = 1$ is

$$\omega_{sp} = \omega_p/\sqrt{2}, \tag{2.42}$$

which is the same as the $q \to 0$ limit of Eq. (2.24).

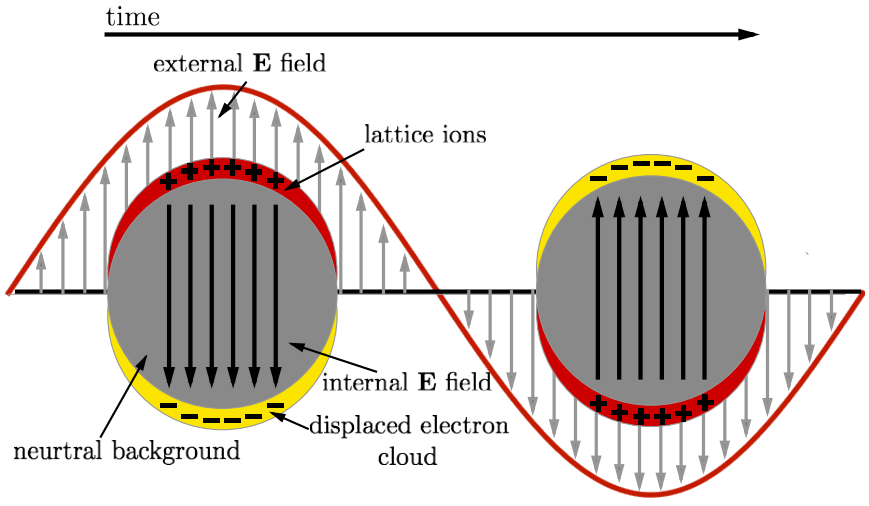

Figure 2.7: Schematic of a resonantly driven localized SP. The red curve is an oscillating external field. The grey circles represent the neutral background, and the yellow portions are the displaced electron cloud. The red portion is the ionic background and the source of the restoring force. Time moves from left to right and takes us through one cycle of oscillation. During the first half of the cycle the field pushes the electron cloud away, during the second half of the cycle it pushes in the opposite direction. If this is done in resonance with the natural frequency of the electron cloud then the near fields located around the sphere are greatly enhanced.

2.4.1 Spherical Nanoparticles

Spherical nanoparticles are of interest because they support localized SPs. We review the quasi-static derivation of SP modes for spherical geometries of a sphere, a layered sphere, and a spheroid.

SP Modes of a Metallic Nanosphere

For a sphere of radius a, the Green function is determined from the following system of equations;

$$\begin{aligned} r < a : -\nabla^2 G(\mathbf{r}, \mathbf{r}') &= 0 \\ r > a : -\nabla^2 G(\mathbf{r}, \mathbf{r}') &= 4\pi\delta(\mathbf{r} - \mathbf{r}'). \end{aligned} \tag{2.43}$$

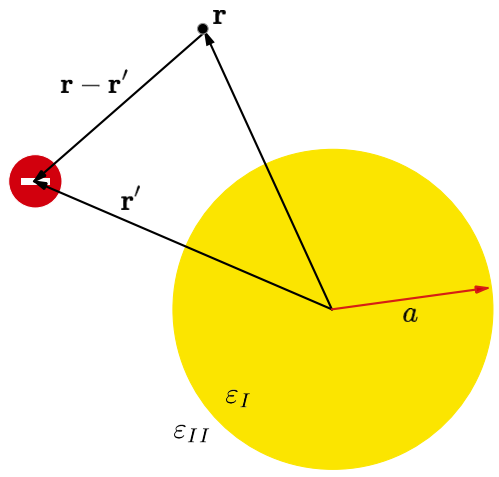

Figure 2.8: Charge placed outside an isolated dielectric sphere.

The coordinate r' is the position of the source, and r is the position where we require knowledge of the potential. Taking into account the expected behavior of the solution at the center of the sphere and at ∞, we write the eigenfunction expansion of the Green function in spherical harmonics. For the three sections of space that include a boundary we write,

$$G_I(r,\theta,\varphi) = \sum_{l=0}^{\infty}\sum_{m=-1}^{l} A_{lm} r^l Y_{lm}(\vartheta,\varphi) \qquad r<a \tag{2.44}$$

$$G_{II}(r,\vartheta,\varphi) = \sum_{l=0}^{\infty}\sum_{m=-1}^{l} \left(B_{lm} r^l + \frac{C_{lm}}{r^{l+1}}\right) Y_{lm}(\vartheta,\varphi), \qquad a<r<r' \tag{2.45}$$

$$G_{III}(r,r_i\phi) = \sum_{l=0}^{\infty}\sum_{m=-1}^{l} \frac{D_{lm}}{r^{l+1}} Y_{lm}(\vartheta,\varphi) \qquad r>r' \tag{2.46}$$

Here, $\cos\gamma = \cos\vartheta\cos\vartheta' + \sin\vartheta\sin\vartheta'\cos(\varphi-\varphi')$ is the angle between r and r'. We apply the usual boundary conditions at the surface of the sphere.

$$\left[-\frac{\partial G}{\partial r}\right]_{r=a+0} = \left[-\varepsilon\frac{\partial G}{\partial r}\right]_{r=a-0} \tag{2.47}$$

At the location of the source, $r=r'$, we have,.

$$\left[-r^2\frac{\partial G}{\partial r}\right]_{r=a+0}^{r=r'+0} = \frac{4\pi}{\sin\vartheta}\delta(\vartheta-\vartheta')\delta(\varphi-\varphi'). \tag{2.48}$$

Expanding the delta function source in spherical harmonics and solving for the coefficients,

$$A_{lm} = \frac{4\pi Y^*_{lm}(\vartheta',\varphi')}{l(\varepsilon+1)+1}\frac{1}{r'^{l+1}} \tag{2.49}$$

$$B_{lm} = \frac{4\pi Y^*_{lm}(\vartheta',\varphi')}{(2l+1)}\frac{1}{r'^{l+1}} \tag{2.50}$$

$$C_{lm} = -\frac{(\varepsilon-1)l}{l(\varepsilon+1)+1}\frac{4\pi Y^*_{lm}(\vartheta',\varphi')}{(2l+1)}\frac{a^{2l+1}}{r'^{l+1}} \tag{2.51}$$

$$D_{lm} = C_{lm} + \frac{4\pi Y^*_{lm}(\vartheta',\varphi')}{(2l+1)}\frac{a^{2l+1}}{r'^{l+1}} \tag{2.52}$$

The addition theorem for spherical harmonics we find,

$$P_l(\cos\gamma) = \sum_{m=-1}^{l}\frac{4\pi}{2l+1}Y_{lm}(\vartheta,\varphi)Y^*_{lm}(\vartheta',\varphi') \tag{2.53}$$

allows us to express the Green function in terms of Legendre polynomials,

$$G(\mathbf{r},\mathbf{r}') = \frac{1}{|\mathbf{r}-\mathbf{r}'|} - \sum_{l=1}^{\infty}\frac{(\varepsilon-1)l}{l(\varepsilon+1)+1}\left(\frac{a^{2l+1}}{r'^{l+1}}\right)\frac{1}{r^{l+1}}P_l(\cos\gamma). \tag{2.54}$$

Here we have set $\varepsilon_1 = 2$ and $\varepsilon_2 = \varepsilon$. To consider the frequency response of the metal, we the invoke quasistatic approximation and set $\varepsilon = \varepsilon(\omega)$. The response function is thus,

$$g(\omega;l) = \frac{l(\varepsilon(\omega)-1)}{l(\varepsilon(\omega)+1)+1}. \tag{2.55}$$

The roots of the denominator of the response function gives us the eigenspectrum of the SP modes. They are,

$$\omega_{sp} = \omega_p\sqrt{\frac{l}{2l+1}}, \tag{2.56}$$

for l between 0 and ∞, where ω_p is the bulk frequency. This gives a bound on possible values of ω_{sp},

$$\frac{\omega_p}{\sqrt{3}} \leq \omega_{sp} \leq \frac{\omega_p}{\sqrt{2}}: \tag{2.57}$$

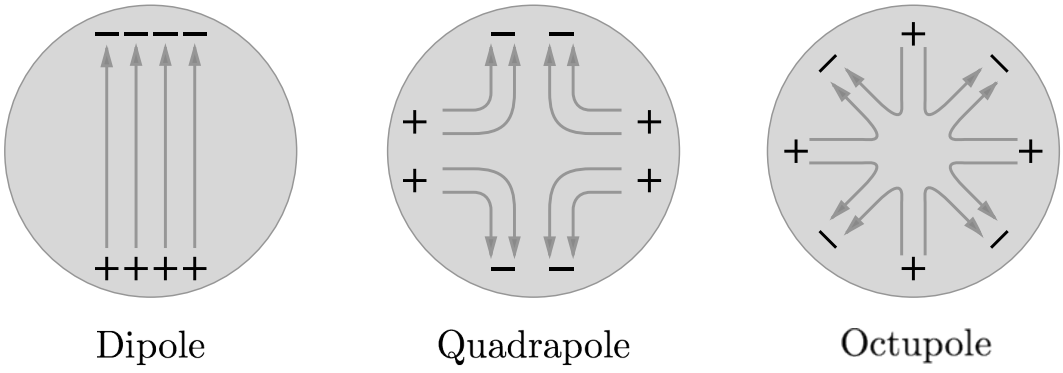

Figure 2.9: Multipole response of a metal sphere.

Each value of l labels an eigen-mode of the system, $l = 1$ corresponds to the dipole mode and $l = 2$ is the quadrupole mode. Notice that the upper bound of ω_{sp} as $l \to \infty$ is $\omega_p/\sqrt{2}$, which is the Ritchie frequency for planar SPs. Every mode of the sphere is a standing wave with $l - 1$ nodes. As $l \to \infty$, the oscillations associated with higher order modes become so dense that the SP standing wave does not distinguish the curvature of a sphere from that of a plane. In the quasistatic limit, the $l \to \infty$ limit is equivalent to the $a \to \infty$ limit of the sphere. Figure 2.7 describes SP resonance.

SP modes of core/shell and shell/core systems

We now consider the geometry of a nanoshell. When finding the SP modes, we will consider two cases. The case of a metal core with a dielectric shell (core/shell), and the case of a dielectric core with a metallic shell (shell/core).

Since the procedure for finding the Green function is the same as in earlier examples for shell geometries, we write down the solution directly;

$$G(\mathbf{r}, \mathbf{r}') = \frac{1}{|\mathbf{r} - \mathbf{r}'|} + \sum_{l=1}^{\infty} F(\varepsilon; l) \frac{R_{II}^{2l+1}}{(r'r)^{l+1}} P_l(\cos\gamma). \tag{2.58}$$

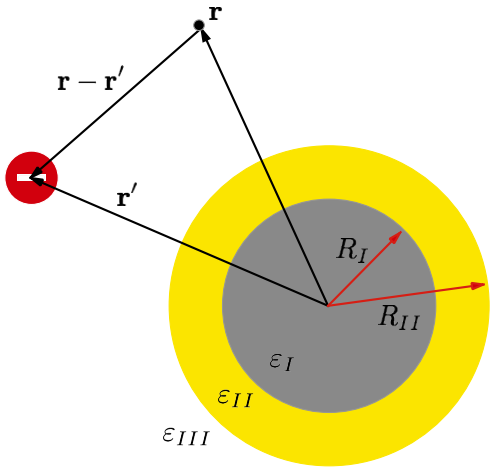

Figure 2.10: Charge placed outside a isolated shell.

Here, $F(\varepsilon; l)$ is the response function,

$$F(\varepsilon; l) = -\frac{(\beta_l + 1)/\varepsilon_{II} + \beta_l/\varepsilon_{III}}{1 + \alpha_l \beta_l \bar{r}^{2l+1}} \alpha_l R_I^{2l+1} + \frac{(\beta_l + 1)/\varepsilon_{II} - 1/\varepsilon_{III}}{1 + \alpha_l \beta_l \bar{r}^{2l+1}} R_{II}^{2l+1}. \quad (2.59)$$

In Eq. (2.59) we have introduced have also defined the following dimensionless parameters:

$$\alpha_l = \frac{l(\varepsilon_I/\varepsilon_{II} - 1)}{(l\varepsilon_I/\varepsilon_{II} + l + 1)} \quad (2.60)$$

$$\beta_l = \frac{(l+1)(\varepsilon_{II}/\varepsilon_{III} - 1)}{(l\varepsilon_{II}/\varepsilon_{III} + l + 1)} \quad (2.61)$$

$$\bar{r} = R_I/R_{II}. \quad (2.62)$$

Here, R_I is the radius of the inner shell, and R_{II} is the radius of the outer shell. The relative permittivity ε_I, ε_{II}, and ε_{III} correspond to inner, outer, and surrounding space respectively. We once again invoke the quasistatic approximation, but consider the core/shell and shell/core structures separately.

Core/Shell

The modes of a core/shell plasmon are obtained by setting $\varepsilon_{III} = \varepsilon(\omega)$ and solving for the roots of the response function, $F(\varepsilon, l)$. In this case the SP frequencies are

$$\left(\omega_{sp}^{\pm}\right)^2 = \omega_p^2 \frac{l\left((l+1)\bar{r}^{2l+1}(\varepsilon_{II}-\varepsilon_{III})+\varepsilon_{III}+l(\varepsilon_{II}+\varepsilon_{III})\right)}{l(l+1)\bar{r}^{1+2L}(1-\varepsilon_{II})(\varepsilon_{II}-\varepsilon_{III})+(l+\varepsilon_{II}+l\varepsilon_{II})(\varepsilon_{III}+l(\varepsilon_{II}+\varepsilon_{III}))} \tag{2.63}$$

The $l = 1$ mode is,

$$\omega_{sp} = \sqrt{\frac{\omega_p(\varepsilon_{II}+2\bar{r}^3(\varepsilon_{II}-\varepsilon_{III})+2\varepsilon_{III})}{2\bar{r}^3(1-\varepsilon_{II})(\varepsilon_{II}-\varepsilon_{III})+(1+2\varepsilon_{II})(\varepsilon_{II}+2\varepsilon_{III})}}, \tag{2.64}$$

and the $l = \infty$ mode is,

$$\omega_{sp} = \frac{\omega_p}{\sqrt{(1+\varepsilon_{II})}}. \tag{2.65}$$

SP modes of a metal shell with a dielectric core

$$(\omega_{sp}^{\pm})^2 = \omega_p^2 \frac{-\varepsilon_{III}+l\left(-2(1+\varepsilon_{III})-(l+1)\bar{r}^{2l+1}(-2+\varepsilon_I+\varepsilon_{III})-l(2+\varepsilon_I+\varepsilon_{III})\right)\pm\bar{\lambda}}{2l(l+1)\bar{r}^{2l+1}(\varepsilon_I-1)(\varepsilon_{III}-1)-2(1+l+l\varepsilon_I)(l+(l+1)\varepsilon_{III})}. \tag{2.66}$$

Here, we have defined the dimensionless parameter $\bar{\lambda}$ as,

$$\bar{\lambda}^2 = -4l^2(l+1)^2\left(\bar{r}^{2l+1}-1\right)^2\varepsilon_I\varepsilon_{III}+\left((2l+1)\varepsilon_{III}+l\left(l+(l+1)\bar{r}^{2l+1}\right)(\varepsilon_I+\varepsilon_{III})\right)^2 \tag{2.67}$$

By setting $\varepsilon_I = \varepsilon_{II} = \epsilon$ we get a simplified expression that maintains all orders of l,

$$\omega_{sp}^{\pm} = \sqrt{\frac{2l(l+1)(\varepsilon-1)r^{2l+1} + 2l(l+1)(\varepsilon+1) + \varepsilon \pm \lambda\varepsilon(2l+1)}{2\varepsilon - 2l(l+1)\left(r^{2l+1}(\varepsilon-1)^2 - (\varepsilon+1)^2\right)}}. \tag{2.68}$$

Here, $\lambda = \bar{\lambda}(\varepsilon_I = \varepsilon_{II} = \varepsilon)$.

In the $l \to \infty$ limit we obtain,

$$\omega_{sp}^{\pm} = \frac{\omega_p}{\sqrt{1+\varepsilon_I}}, \frac{\omega_p}{\sqrt{1+\varepsilon_{III}}}. \tag{2.69}$$

Here we have two values of ω_{sp} due to the two metal surfaces of a shell. This gives rise to two modes correspond to oscillation being in phase or out of phase.

Without assuming any values for the dielectric constant inside and outside of the shell, we find that the $l = 1$ SP mode is,

$$\omega_1^{\pm} = \omega_{sp}\frac{\sqrt{(\varepsilon_I + 4\varepsilon_{III} - 4 + 2\bar{r}^3(-2 + \varepsilon_I + \varepsilon_{III}) \pm \mathcal{A}]}}{4\bar{r}^3(\varepsilon_I - 1)(\varepsilon_{III} - 1) - 2(2+\varepsilon_I)(1+2\varepsilon_{III})} \tag{2.70}$$

Here we have defined a dimensionless parameter,

$$\mathcal{A} = \sqrt{(\varepsilon_I - 4\varepsilon_{III})^2 + 4\bar{r}^6(\varepsilon_I - \varepsilon_{III})^2 + 4\bar{r}^3\left(\varepsilon_I^2 + 13\varepsilon_I\varepsilon_{III} + 4\varepsilon_{III}^2\right)}.$$

Setting $\varepsilon_I = \varepsilon_{III} = \varepsilon$ simplifies this expression to give,

$$\omega_{sp}^{\pm} = 2\omega_p\sqrt{\frac{1-\bar{r}^3}{4 + 4\bar{r}^3(\varepsilon-1) + 5\varepsilon \pm 3\varepsilon\sqrt{1+8\bar{r}^3}}}. \tag{2.71}$$

Surface-plasmon Modes of Prolate Spheroid

To model anisotropic SP modes, we consider a metal nanoparticle in the shape of a prolate spheroid. Some liberty can be taken when defining the prolate spheroidal coordinate system and we follow the convention of Morse and Feshbach [Mor81]. We place the center of the prolate spheroid at the origin of a Cartesian coordinates

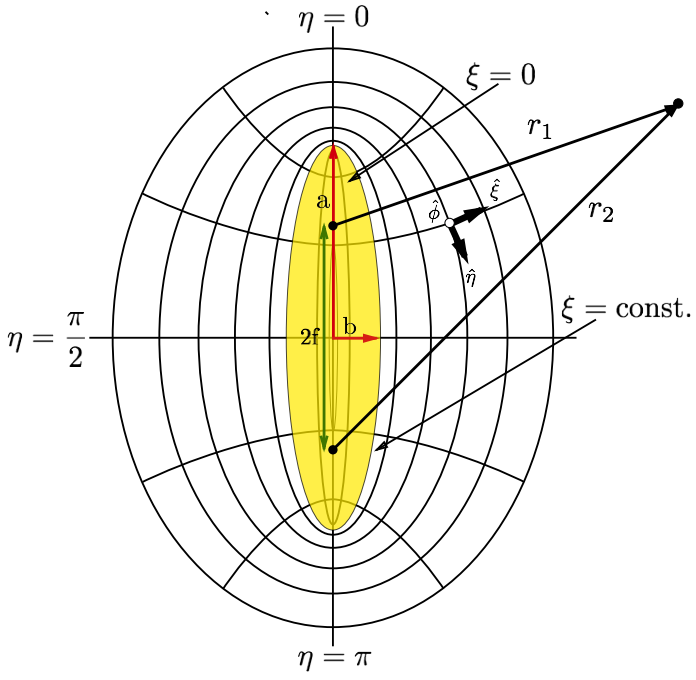

Figure 2.11: Prolate spheroidal coordinate system.

system and orient the spheroidal major axis along the z-axis and the minor axis in the (x, y) plane.

After denoting the length of the major and minor axis by a and b respectively, the prolate spheroidal coordinates are defined as,

$$\xi = (r_1 - r_2)/2f \tag{2.72}$$

$$\eta = (r_1 + r_2)/2f. \tag{2.73}$$

Here, $f = \sqrt{a^2 - b^2}$ is the distance to the focal points and $\eta = [1 - (a/b)^2]^{-1/2}$ is inverse eccentricity. With this we define distances that connect the focal points of the spheroid to any point in space,

$$r_1 = \sqrt{x^2 + y^2 + (z + f)^2}, \tag{2.74}$$

$$r_2 = \sqrt{x^2 + y^2 + (z - f)^2}. \tag{2.75}$$

The Cartesian coordinate representation in prolate spheroidal coordinates are,

$$x = f[(1-\xi^2)(\eta^2-1)]^{1/2}\cos\varphi, \tag{2.76}$$

$$y = f[(1-\xi^2)(\eta^2-1)]^{1/2}\sin\varphi, \tag{2.77}$$

$$z = f\xi\eta. \tag{2.78}$$

Spherical coordinates can be recovered as a limiting case by taking $\eta \to \infty$ and $\eta f \to r$. The Green function is sought by solving the boundary-valued problem for a point charge disturbance. The eigenfunction expansion in prolate spheroidal coordinates is given in terms of the associated Legendre polynomials P_n^m and Q_n^m of the first and the second kind, respectively [Mor81]. Following the approach of Morse and Feshbach [Mor81], we write the Green function for inside and outside the spheroid,

$$G(\boldsymbol{r}) = \frac{1}{f}\sum_{l=0}^{\infty}\sum_{m=0}^{n}\left(A_{nm}\cos m\varphi + B_{lm}\sin m\varphi\right)P_l^m(\xi)Q_l^m(\eta) \quad \eta > \eta_0 \tag{2.79}$$

$$G(\boldsymbol{r}) = \frac{1}{f}\sum_{l=0}^{\infty}\sum_{m=0}^{n}\left(C_{lm}\cos m\varphi + D_{lm}\sin m\varphi\right)P_l^m(\xi)P_l^m(\eta) \quad \eta < \eta_0 \tag{2.80}$$

Here η_0 is the boundary of the spheroid.

We also need the eigenfunction expansion of a point charge in spheroidal coordinates [Mor81] located at point $\boldsymbol{r}' = (\xi', \eta', \varphi')$:

$$\begin{aligned} G_s(\boldsymbol{r}, \boldsymbol{r}') &= \frac{1}{|\boldsymbol{r} - \boldsymbol{r}'|} \\ &= \frac{1}{f}\sum_{l=0}^{\infty}\sum_{l=0}^{n} H_{lm}\cos m(\varphi - \varphi')P_l^m(\xi)P_l^m(\xi')P_l^m(\eta_<)Q_l^m(\eta_>) \end{aligned} \tag{2.81}$$

Here,

$$H_{lm} = (2n+1)(2-\delta_{m0})(-1)^m\left[\frac{(l-m)!}{(l+m)!}\right] \tag{2.82}$$

and $\eta_< = \min(\eta, \eta')$ and $\eta_> = \max(\eta, \eta')$. Assuming that the charge is outside the spheroidal nanoparticle, we set $\eta_< = \eta$ and $\eta_> = \eta'$.

By matching the boundary conditions, we obtain the coefficients:

$$A_{nm} = -\frac{\Lambda_{nm}\cos m\varphi'\left[\varepsilon(\omega)/\varepsilon_d - 1\right]}{\left[Q_n^m(\eta_0)/P_n^m(\eta_0)\right]\varepsilon(\omega)/\varepsilon_d - \left[Q_n^{m\prime}(\eta_0)/P_n^{m\prime}(\eta_0)\right]} \tag{2.83}$$

$$B_{lm} = -\frac{\Lambda_{lm}\sin m\varphi'\left[\varepsilon(\omega)/\varepsilon_d - 1\right]}{\left[Q_l^m(\eta_0)/P_l^m(\eta_0)\right]\varepsilon(\omega)/\varepsilon_d - \left[Q_l^{m\prime}(\eta_0)/P_l^{m\prime}(\eta_0)\right]} \tag{2.84}$$

$$C_{lm} = A_{lm}\left[Q_l^m(\eta_0)/P_n^m(\eta_0)\right] + \Lambda_{lm}\cos m\varphi' \tag{2.85}$$

$$D_{lm} = B_{lm}\left[Q_l^m(\eta_0)/P_l^m(\eta_0)\right] + \Lambda_{lm}\sin m\varphi' \tag{2.86}$$

where

$$\Lambda_{lm} = H_{lm}P_l^m(\xi')Q_l^m(\eta'). \tag{2.87}$$

Solving for the SP eigenspectrum gives,

$$\omega_{sp}^2 = \omega_p^2\frac{\varepsilon_d P_n^{m\prime}(\eta_0)Q_n^m(\eta_0)}{P_n^{m\prime}(\eta_0)Q_n^m(\eta_0) - Q_n^{m\prime}(\eta_0)P_n^m(\eta_0)} \tag{2.88}$$

2.5 Conclusion

The purpose of this Chapter was to to provide a basic overview and create a reference. We have derived the near field SP eigenmodes for every geometry considered in later chapters and we have reviewed the basics of SP theory.

Chapter 3

Förster Transfer in the Presence of Metal Nanospheres

3.1 Introduction

Förster resonance energy transfer (FRET), is the non-radiative transfer of energy between neighboring molecules [För60, För48]. This process is enhanced by the presence of metal surfaces [GLK07, KBR$^+$08, KTS$^+$13]. In this chapter, we review the basics of Förster theory and show how to account for the presence of SPs. Specifically we consider the influence of MNPs on the FRET rate between two QDs.

Förster Theory

FRET describes nonradiative energy transfer from a donor molecule to an acceptor molecule. Since it is mediated by near field interactions, it does not involve the emission or absorption of real photons. FRET occurs when the donor has an induced dipole moment, which is resonant to the gap energy of the acceptor. The strength

of the interaction depends on the strength of the induced dipole and the respective orientation of the donor and acceptor. The Förster rate can be derived following a semi-classical approach or through quantum mechanics using Fermi's golden rule. We choose the latter to show how to derive the result. A derivation of the type presented here can be found in any standard textbooks on the subject [Bir70, NH12].

We model the donor and acceptor molecules as two-level systems shown in Fig.3.1, with allowed dipole transitions, and write a Hamiltonian for the system in which they are coupled through dipole-dipole interaction.

$$
\begin{aligned}
H &= H_0 + H_1 && (3.1)\\
H_0 &= |D^*A\rangle\, H_D\, \langle D^*A| + |A^*D\rangle\, H_A\, \langle A^*D| && (3.2)\\
H_1 &= -\boldsymbol{\mu}_D \cdot \mathbf{E}_D = \frac{3(\boldsymbol{\mu}_A \cdot \hat{\mathbf{r}})(\boldsymbol{\mu}_D \cdot \hat{\mathbf{r}}) - \boldsymbol{\mu}_A \cdot \boldsymbol{\mu}_D}{\mathbf{r}^3} && (3.3)
\end{aligned}
$$

The states $|D\rangle$ and $|A\rangle$ represents the donor and acceptor subsystems, respectively. The unit vector $\hat{\mathbf{r}}$ connects the center of mass of the donor and acceptor transition dipoles, $\boldsymbol{\mu}_D$ and $\boldsymbol{\mu}_A$, and $\mathbf{r}$ is the distance between them. H_0 is composed of H_D and H_A, which represent the excited state energy of the donor and acceptor parameterized by vibrational coordinates, respectively. H_1 is the dipole-dipole donor-acceptor interaction energy. High-multipole interactions are neglected and H_1 is taken as a small perturbation. H_D and H_A are taken to be displaced oscillator potentials in the Condon approximation [Bir70], meaning that the dipole operators act solely on the electronic states. Though we call this resonant energy transfer, the inclusion of the fast vibrational dynamics introduces intraband relaxation processes assisting in the energy flow from donor to acceptor. We apply this concept by always taking the acceptor to be slightly detuned from the excitation energy of the donor. This coincides with what is observed in experiment.

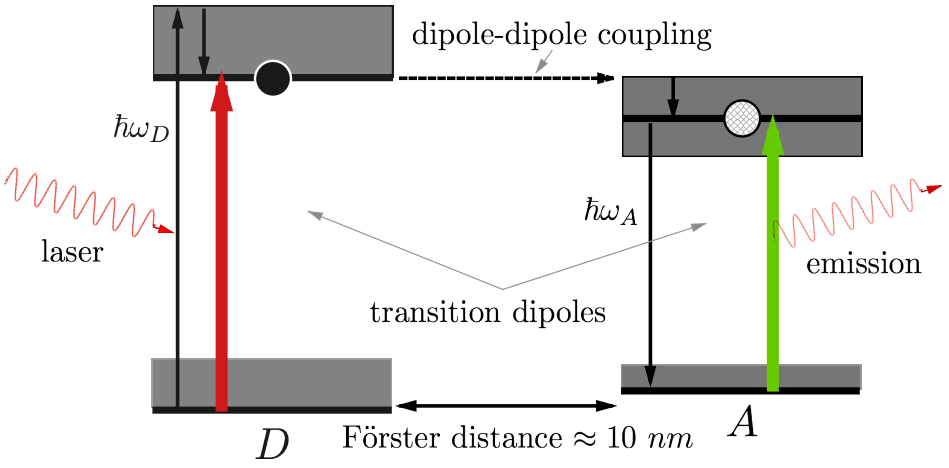

Figure 3.1: Schematic of Förster transfer mechanism. An incoming laser excites a "donor" molecule into an excited state, which quickly relaxes down to the bottom of the band and forms an exciton with energy $\hbar\omega_D$. This induces a transition dipole in a nearby "acceptor" molecule, which then interacts with the donor through a dipole-dipole coupling. The excitation hops from donor to acceptor through a non-radiative energy transfer and then quickly relaxes to the bottom of the band and emits the energy as radiation with energy $\hbar\omega_A$.

We begin by introducing acceptor and donor dipole operators as,

$$\boldsymbol{\mu}_A = |A\rangle \boldsymbol{\mu}_{AA^*} \langle A^*| + c.c., \tag{3.4}$$

$$\boldsymbol{\mu}_D = |D\rangle \boldsymbol{\mu}_{DD^*} \langle D^*| + c.c., \tag{3.5}$$

and recast the interaction term Eq. (3.3) to the following operator form,

$$H_1 = \mu_A \mu_D \frac{\kappa}{r^3} \left[|D^* A\rangle \langle A^* D| + |A^* D\rangle \langle D^* A| \right], \tag{3.6}$$

where an asterisk indicates the excited states and

$$\mu_D = |\, \boldsymbol{\mu}_d \,|^2, \tag{3.7}$$

$$\mu_A = |\, \boldsymbol{\mu}_A \,|^2, \tag{3.8}$$

$$\kappa = 3(\hat{e}_A \cdot \hat{r})(\hat{e}_D \cdot \hat{r}) - \hat{\mu}_A \hat{\mu}_D. \tag{3.9}$$

According to the Fermi's golden rule, the FRET rate associated with the Hamiltonian given by Eq. (3.6) is;

$$\begin{aligned} R_{f\leftarrow i} &= \frac{2\pi}{\hbar^2} \mid \langle f \mid H_1 \mid i \rangle \mid^2 \rho(\varepsilon_f) && (3.10)\\ &= \frac{2\pi}{\hbar^2} \sum_f \mid \langle A^*D \mid H_1 \mid D^*A \rangle \mid^2 \delta(\varepsilon_f - \varepsilon_i) && (3.11)\\ &= \frac{2\pi}{\hbar^2} \sum_f \mid \langle A^*D \mid \mu_A \mu_D \frac{\kappa}{r^3} \left[\mid D^*A \rangle \langle A^*D \mid + \mid A^*D \rangle \langle D^*A \mid \right] \mid D^*A \rangle \mid^2 \delta(\varepsilon_f - \varepsilon_i) \\ &= \frac{2\pi}{\hbar^2} \sum_f \mid \langle A^*D \mid \mu_A \mu_D \frac{\kappa}{r^3} \left[\mid D^*A \rangle \langle A^*D \mid + \mid A^*D \rangle \langle D^*A \mid \right] \mid D^*A \rangle \mid^2 \delta(\varepsilon_f - \varepsilon_i) \\ &= \frac{2\pi}{\hbar^2} \sum_f \mid \mu_A \mu_D \frac{\kappa}{r^3} \mid^2 \delta(\varepsilon_f - \varepsilon_i). \end{aligned}$$

In Eq. (3.11), the initial energy ε_i is the sum of the initial energy of the donor and the initial energy of the acceptor:

$$\varepsilon_i = \varepsilon_i^A + \varepsilon_i^D, \tag{3.12}$$

and the final energy ε_f is the sum of the final energy of the donor and the final energy of the acceptor:

$$\varepsilon_f = \varepsilon_f^A + \varepsilon_f^D, \tag{3.13}$$

The delta-function can be written as the integral of a product of delta functions. One for the donor, and one for the acceptor,

$$\int \delta\left(\varepsilon - \varepsilon_f^D + \varepsilon_i^D\right) \delta\left(\varepsilon - \varepsilon_f^A + \varepsilon_i^A\right) d\varepsilon \tag{3.14}$$

For each molecule, the energies are *sums* of the electronic state energies plus the vibrational state energies. In calculating the exciton hopping rate, we are interested in the rate for specific electronic state energies, without regard to the particular vibrational state energy the molecule happens to be in when they interact. For this reason, we introduce a thermal average over initial vibrational state energies;

$$\frac{1}{Z_A Z_D^*} \sum_{i(D),i(A)} e^{-\beta(\varepsilon_i^D + \varepsilon_i^A)} \int \delta\left(\varepsilon - \varepsilon_f^D + \varepsilon_i^{*D}\right) \delta\left(\varepsilon - \varepsilon_f^{*A} + \varepsilon_i^A\right) d\varepsilon. \tag{3.15}$$

The factorization of the partition function for the vibrational manifold, $Z = Z_A Z_D^*$ occurs under the assumption that the vibrational modes on each molecule are independent. The asterisk indicates that for the donor, it is the excited-state vibrational manifold that is averaged over. Similarly, for the acceptor, the final state is the excited-state vibrational manifold. The next ingredient is the square of the matrix element $\mid \mu_A \mu_D \frac{\kappa}{r^3} \mid$ in Eq. (3.10). This factorizes into a product of squares of the Frank-Condon overlap factors, $FC^2_{i(D),f(D)}$ for the down-transition in the donor oscillator manifold, and $FC^2_{i(A),f(A)}$ for the up-transition in the acceptor oscillator manifold.

Under the assumption that the electronic part of the transition matrix element, can be taken to be approximately independent of the vibrational states, the transfer rate can be written as the overlap of a product of two functions,

$$\begin{aligned} R \;\; \propto \;\; & \int d\varepsilon \left(\sum_{i(D),f(D)} \frac{e^{-\beta \varepsilon_i^{*D}}}{Z_D^*} FC^2_{i(D),f(D)} \delta\left(\varepsilon - \varepsilon_f^D + \varepsilon_i^{*D}\right) \right) \\ & \cdot \left(\sum_{i(A),f(A)} \frac{e^{-\beta \varepsilon_i^A}}{Z_A} FC^2_{i(A),f(A)} \delta\left(\varepsilon - \varepsilon_f^A + \varepsilon_i^A\right) \right). \end{aligned}$$

The first factor is the line-shape function that characterizes the emission spectrum of the donor,

$$\sigma^D_{fluor}\left(\varepsilon\right) \propto \sum_{i(D),f(D)} \frac{e^{-\beta \varepsilon_i^{*D}}}{Z_D^*} FC^2_{i(D),f(D)} \delta\left(\varepsilon - \varepsilon_{f(D)} + \varepsilon_i^{*D}\right),$$

and the second factor is the line-shape function that characterizes the absorption spectrum of the acceptor,

$$\sigma^A_{abs}\left(\varepsilon\right) = \sum_{i(A),f(A)} \frac{e^{-\beta \varepsilon_{i(A)}}}{Z_A} FC^2_{i(A),f(A)} \delta\left(\varepsilon - \varepsilon_f^{*A} + \varepsilon_{i(A)}\right).$$

Taking into account that the delta-function sums in these expressions describe donor and acceptor density of states, the FRET rate Eq. (3.11) can be represented as,

$$R_{f\leftarrow i} = \frac{2\pi}{\hbar^2} \frac{\mid \mu_D \mid^2 \mid \mu_A \mid^2 \kappa^2}{r^6} J. \tag{3.16}$$

Here,

$$J = \int_{-\infty}^{\infty} \sigma^D_{fluor}(\varepsilon)\sigma^A_{abs}(\varepsilon)\ d\varepsilon. \tag{3.17}$$

is the overlap integral between the donor emission and acceptor absorption spectra.

The rate given by Eq.(3.16) has the characteristic $1/r^6$ spatial scaling resulting from the donor and acceptor dipole-dipole interactions. Also, it is a function of the overlap of donor emission and acceptor absorption line-shapes. The orientational term κ is of great importance since it can completely eliminate Förster transfer when the transition dipoles are oriented perpendicular with respect to each other. Due to the uncertainty of the exact orientation of the donor and acceptor, and because many experiments are done on an ensemble of molecules, κ is usually rotationally averaged. The spectral overlap integral, J, is usually determined by experiment and will henceforth be taken as a parameter.

3.2 FRET in the Presence of MNPs

In this section we will model FRET in the presence of MNPs. We will consider three different MNPs, a metal sphere, a metal sphere with a dielectric shell (core/shell), and a metal shell with a dielectric core (shell/core). All systems will be assumed to be embedded in a medium with dielectric constant ε_d. The metal's permittivity will be calculated using data from the experiments of Johnston and Christy [JC72].

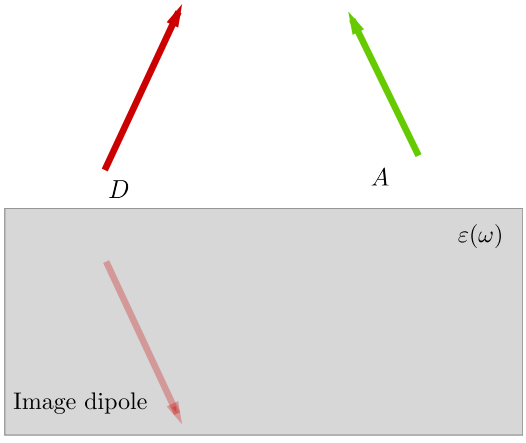

Figure 3.2: Schematic of Förster transfer in the presence of a semi-infinite metal slab. The donor transition dipole induces an image response at the metal surface. We do not consider the secondary effect of the image of the acceptor transition dipole.

The problem of Förster transfer above a planar metal surface has been well studied, beginning with the seminal work of Chance, Prock and Silbey [CPS78]. The last few years have seen greater interest in the use of nanoparticles to observe this effect. Since MNPs can provide localized SPs with intense field enhancements, they are an ideal candidate for enhancing the Förster rate. Spherical nanoparticles have received a significant amount of attention due to reliable synthetic techniques and their strong plasmonic characteristics [DRKS08].

Solutions to spherical geometries can be written down exactly through Mie theory, or more simply in the near field quasi-static approximation [EN74]. For SP frequencies of MNPs smaller than the wavelength of optical light the method is in excellent agreement with experiment. The quasi-static approximation does fail to predict retardation effects, such as the size dependence of ω_{sp} [Kre92, KG85, KF69]. Also not included are effects due to electron wave function spill out from nanoparticles of very small radii [HL94, CA74].

When including the effects of a metal surface, the simplest approach is to modify

Eq. (3.16) by including the image electric field induced by the donor transition dipole on the surface of the nanoparticle (see Fig. 3.2 for planar geometry). Clearly the type of metal and its geometry are important due to the effect that these parameters have on the value of the SP resonance frequency. Specifically, we modify the transition matrix element used in the Fermi's golden rule calculation by expanding the electric field term to include the image field of the donor due to the presence of the MNP. We therefore want to calculate,

$$R_{f\leftarrow i} = \frac{2\pi}{\hbar} \left|\langle f|\hat{\boldsymbol{\mu}}_A \cdot \mathbf{E}_D^{total}|i\rangle\right|^2 J. \tag{3.18}$$

Here, $\mathbf{E}_D^{total}$ is the total electric field of the donor transition dipole and the image response of the metal. We have not included secondary effects, such as the image response of the MNP to the acceptor transition dipole field, or feedback re-polarization. It is assumed that these effects are small when compared to the electric field of the donor transition dipole and its image.

The total electric field will depend on the polarizabilty, $\alpha(\omega)$, of the MNP, which is singular when a SP is excited. But enhancement of the electric field does not guarantee enhancement of the Förster rate because the presence of a metal surface also opens up decay channels that didn't exist in the system prior to it being plasmonically coupled.

We can mitigate this somewhat by tuning the parameters of the system in such a way as to change its energy profile. For example, it is well known that gold is very lossy in the frequency range surrounding ω_{sp}. This is due to contributions to the damping coefficient by interband scattering, which is unfortunately high around optical frequencies. Nanorods partially solve this problem by reducing non-radiative damping in gold nanoparticles [Sön01]. This can be understood by modeling the nanorod as a prolate spheroid. Doing so gives an expression for the SP modes that depends on the aspect ratio of the spheroid. Higher aspect ratios lower ω_{sp}, which

places the system in a frequency range further away from where interband scattering dominates.

Ignoring this problem for now, let's return to modifying Fermi's golden rule to include image effects. We need to calculate the total electric field of the donor and its image. The potential of a point charge is proportional the Green function,

$$G_0(\boldsymbol{r}, \boldsymbol{r}') = \frac{1}{\mid \boldsymbol{r} - \boldsymbol{r}' \mid} \tag{3.19}$$

We expand the Green function in a Taylor series expansion as follows [SDMT98]:

$$\begin{aligned} \frac{1}{\mid \boldsymbol{r} - \boldsymbol{r}' \mid} &= \frac{1}{r} - \boldsymbol{r}' \cdot \boldsymbol{\nabla} \frac{1}{r} + \frac{1}{2} \left(\boldsymbol{r}' \cdot \boldsymbol{\nabla} \right)^2 \frac{1}{r} + \cdots \\ &= \frac{1}{r} + \frac{\boldsymbol{r} \cdot \boldsymbol{r}'}{r^3} + \frac{1}{2} \frac{1}{r^5} \boldsymbol{r} \cdot \left(3 \boldsymbol{r} \boldsymbol{r}' - \mathbf{1} r'^2 \right) \cdot \boldsymbol{r} + \cdots . \end{aligned} \tag{3.20}$$

On the first line of Eq. (3.20), the first term is the potential of a point charge, the second term is the interaction energy of a point dipole with the field produced by a point charge, and the third term is the interaction energy of a point quadrupole and the field of a point dipole. Equating the second terms of lines 1 and 2 of Eq. (3.20) gives,

$$\frac{\boldsymbol{r} \cdot \boldsymbol{r}'}{r^3} = -\boldsymbol{r}' \cdot \boldsymbol{\nabla} \frac{1}{r} \tag{3.21}$$

Since the Green function is invariant under the substitution $\boldsymbol{r} \rightarrow \boldsymbol{r}'$, we write,

$$\frac{\boldsymbol{r} \cdot \boldsymbol{r}'}{r^3} = -\boldsymbol{r} \cdot \boldsymbol{\nabla}' \frac{1}{r'}. \tag{3.22}$$

With this identity, we can relate the potential of an arbitrary point dipole $\boldsymbol{\mu}$, to the gradient of the Green function,

$$\phi(\boldsymbol{r})_{dipole} = -\frac{1}{4\pi\varepsilon_0} \boldsymbol{\mu} \cdot \boldsymbol{\nabla}' \frac{1}{r'} \tag{3.23}$$

Recall that the Green function for an inhomogeneous environment has the form,

$$G(\boldsymbol{r},\boldsymbol{r}') = G_0(\boldsymbol{r},\boldsymbol{r}') + g(\omega)G_0(\boldsymbol{r},\boldsymbol{r}''), \tag{3.24}$$

so the argument above works for both the source and image fields. We can use the results of Chapter 2 to derive the potential of a point dipole in the same environments. Therefore, the field of a the donor transition dipole in the presence of a layered dielectric sphere with inner radius R_I and outer radius R_{II}, including its image, is,

$$\mathbf{E}_D^{total} = \boldsymbol{\nabla}((\boldsymbol{\mu}_D \cdot \boldsymbol{\nabla}'\varphi(\mathbf{r},\mathbf{r}')). \tag{3.25}$$

Here $\varphi(\mathbf{r},\mathbf{r}')$ is the potential of a point charge located at $\boldsymbol{r}'$. Using Eq. (2.58) we obtain an expression for the total electric field;

$$\begin{aligned} \mathbf{E}_D^{total} &= \frac{[3(\boldsymbol{\mu}_D \cdot \hat{\mathbf{r}})\hat{\mathbf{r}} - \boldsymbol{\mu}_D]}{r^3} \\ &- \sum_{l=1}^{\infty}\left[\frac{1}{r^{l+2}}g(\omega,l)\left(\frac{a^{2l+1}}{r'^{l+2}}\right)\left(\mathcal{R}(l,\vartheta,\varphi)\hat{\boldsymbol{r}} + \Phi(l,\vartheta,\varphi)\hat{\boldsymbol{\vartheta}} + \Theta(l,\vartheta,\varphi)\hat{\boldsymbol{\varphi}}\right)\right]. \end{aligned} \tag{3.26}$$

Here, $\mathcal{R}(l,\vartheta,\varphi)$, $\Theta(l,\vartheta,\varphi)$, and $\Phi(l,\vartheta,\varphi)$ are defined as follows:

$$\begin{aligned} \mathcal{R}(l,\vartheta,\varphi) &= -\tilde{\mu}_{dx}(l+1)(\sin\vartheta\cos\varphi)P_l'(\cos\vartheta) \\ &- \tilde{\mu}_{dy}(l+1)\sin\vartheta\sin\varphi P_l'(\cos\vartheta) + \tilde{\mu}_{dz}(l+1)^2 P_l(\cos\vartheta), \\ \Theta(l,\vartheta,\varphi) &= (\tilde{\mu}_{dx}\cos\varphi + \tilde{\mu}_{dy}\sin\varphi)(\cos\vartheta P_l'(\cos\vartheta) \\ &- \sin^2\vartheta P_l''(\cos\vartheta)) + \tilde{\mu}_{dz}(l+1)\cos\vartheta P_l'(\cos\vartheta), \\ \Phi(l,\vartheta,\varphi) &= (\tilde{\mu}_{dy}\cos\varphi - \tilde{\mu}_{dx}\sin\varphi)\,P_l'(\cos\vartheta). \end{aligned} \tag{3.27}$$

Also defined is the orientation of the donor transition dipole, $\tilde{\mu}_{dx} = \mu_{dx}\sin\vartheta_D\cos\varphi_D$, $\tilde{\mu}_{dy} = \mu_{dy}\sin\vartheta_D\sin\varphi_D$, and $\tilde{\mu}_{dz} = \mu_{dz}\cos\vartheta_D$, where ϑ_D and φ_D are the angles that define the orientation of the donor.

The first term in Eq. (3.26) is the donor dipole electric field and the second term is the contribution of the images dipoles due to the response of the metal. All primed

coordinates represent the location of the donor and all un-primed coordinates locate the position of the acceptor. We set $\vartheta' = 0$, and $\varphi' = 0$, making $\cos\gamma = \cos\vartheta$. This implies that the donor is oriented along the z-axis. Inserting this expression into Eq. (3.18) allows us to calculate the Föster rate for the multi-polar response of both isolated and shell spherical geometries. The functional form of Eq. (3.26) is the same for both cases, and one only needs to re-define the response function.

Since tuning the energy spacing between donor and acceptor is key for determining the magnitude of the enhancement, it is important to find materials that allow for the control of this parameter. Here we consider QDs, which are small crystals that behave like artificial "atoms" and may be approximated as two-level systems [LBB96, BGL$^+$99]. Because their radii are proportional to their bandgap energies [LBB96], they make ideal candidates for testing the bounds of a plasmonically enhanced FRET. We model the QDs as two transition dipole moments using the following parameters; $J = 0.004\ cm^{-1}$, $\mu_D = 0.2\ D$ and $\mu_A = 22.5\ D$, $a = 20\ nm$, $r' = 22\ nm$ and $r = 22\ nm$ [DRKS08]. When calculating the FRET rate, we place the donor and acceptor QDs equidistant from the surface of the sphere, fixing the position of the donor, and varying the angle between them.

Metal Sphere

The first system we consider is that of two CdSe QDs placed near an isolated metal sphere. We take the parameters from Ref.[DRKS08] and also reproduce some of the results from that work.

For an isolated metal sphere, the response function in Eq. (3.26) is given by,

$$g(\omega; l) = \frac{l(\varepsilon(\omega) - \varepsilon_d)}{l(\varepsilon(\omega) + \varepsilon_d) + \varepsilon_d}. \tag{3.28}$$

The expression for the case of an isolated sphere was derived in Chapter 2, and here we include the effect of the dielectric environment though ε_d. We will use $\varepsilon(\omega)$ of

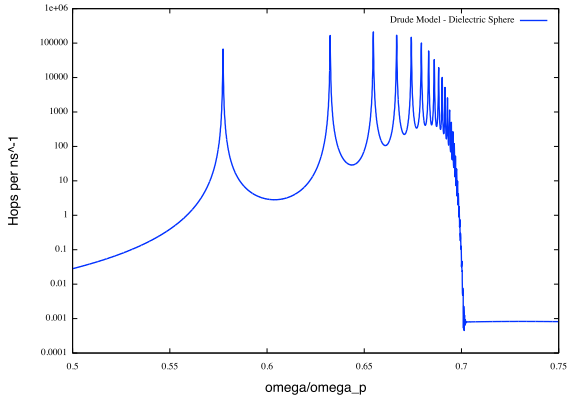

Figure 3.3: SP enhanced FRET rate for an isolated sphere calculated using the Drude model. The peaks represent the spectrum of the system. Each peak corresponds to a term of the multipole expansion of the image field. Dipole response is the first peak and corresponds to $l = 1$. The quadrupole is the second peak and represents $l = 2$, and so on.

the metal to be of the Drude form,

$$\varepsilon(\omega) = \varepsilon_\infty - \frac{\omega_p^2}{\omega(\omega + i\gamma)}, \tag{3.29}$$

where γ is the damping coefficient of the metal and ω_p is the bulk plasma frequency.

Figure 3.3 shows FRET rates as a function of frequency using the Drude model. Here the frequency represents the possible values of the energy gap between ground and excited states of our two-level QD system. We do this to explicitly show how FRET is enhanced in the presence of the metal. We have made the frequency dimensionless with respect to the plasmon frequency, so Fig. (3.3) serves as a qualitative example. Each resonant peak corresponds to a pole of the response function. Whenever the separation between the ground and excited states of the donor-acceptor system are in coincidence with the plasmon frequency, the Föster rate also inherits the associated singularity. This leads to a significant enhancement of the rate.

Figure 3.4 shows the enhancement of the Förster rate when experimental data are used for the dielectric [JC72] response. The effect is still substantial, but obviously

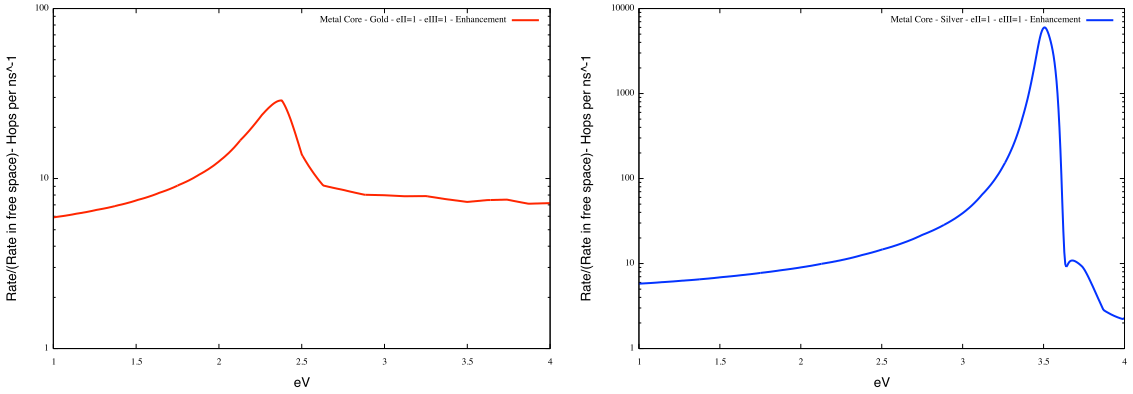

Figure 3.4: Enhancement of Forster rate between two QDs in the presence of both gold (left) and silver (silver) for an isolated metal sphere. Here, $\varepsilon = 1$.

dulled due to the damping. Notice the large difference between Au and Ag MNP cases. Au predicts an enhancement factor of about 30 for a simple isolated sphere and Ag predicts a value on the order of 10^3. The lower enhancements in Au are due to the lossy character in the region around ω_{sp}. Ag is far less lossy in this range. While gold has the benefit of being easy to handle during synthesis, the enhancement gains of silver suggest that it is worth the added difficulty. Furthermore, Ag shows a peak dominated by dipole response but also features a second smaller peak due to quadruple response [HS03]. In contrast, Au is so dissipative in this range that the contributions of higher poles are indistinguishable from the dipole peak. It should be noted that, when calculating these rates, we took many terms in the expansion of the response function. For Au we noticed that, while the overall shape did not seem to be effected, the height of the peak was. It seemed to be the case that higher multipole contribution lowered the height of the peak. This is in contrast to Ag, which shows a nice succession of peaks corresponding to each term of the multipole expansion.

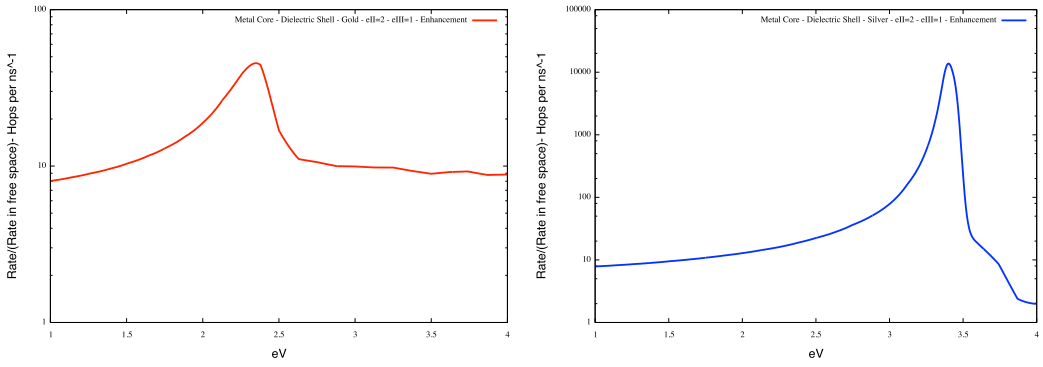

Figure 3.5: Enhancement of FRET rate for both gold and silver core/shell systems in free space as a function of donor-acceptor band gap energy.

Core/Shell and Shell/Core Nanospheres

Next, we consider the case of core/shell and shell/core structures. The form of the response function for these systems before the substitution of a frequency dependent dielectric constant is:

$$g(\omega;l) = -\frac{(\beta_l+1)/\varepsilon_{II}+\beta_l/\varepsilon_{III}}{1+\alpha_l\beta_l\bar{r}^{2l+1}}\alpha_l R_I^{2l+1} + \frac{(\beta_l+1)/\varepsilon_{II}-1/\varepsilon_{III}}{1+\alpha_l\beta_l\bar{r}^{2l+1}}R_{II}^{2l+1}, \quad (3.30)$$

where the dimensionless constants are defined in Eqs.(2.60-2.62). Whether or not we are calculating rates for a core/shell or shell/core depends upon which dielectric constant in Eq. (3.30) is is set to $\varepsilon(\omega)$.

The results of the simulation for the core/shell structure are found in Fig.3.5. This is of interest because often MNPs have a dielectric shell left over form synthesis. This can have a strong effect on the location of the SP frequency. The main features of this system are not much different than those of the isolated sphere. The effect of the dielectric shell is to redshift the value of ω_{sp}. This can lead to slightly higher enhancements because it places the SP mode in a frequency range where the imaginary part of the dielectric function is lower in magnitude.

Shell/core structures are unique because they support SPs on each surface of the shell. Recall that, in Chapter 2, we derived the modes for this system and found the

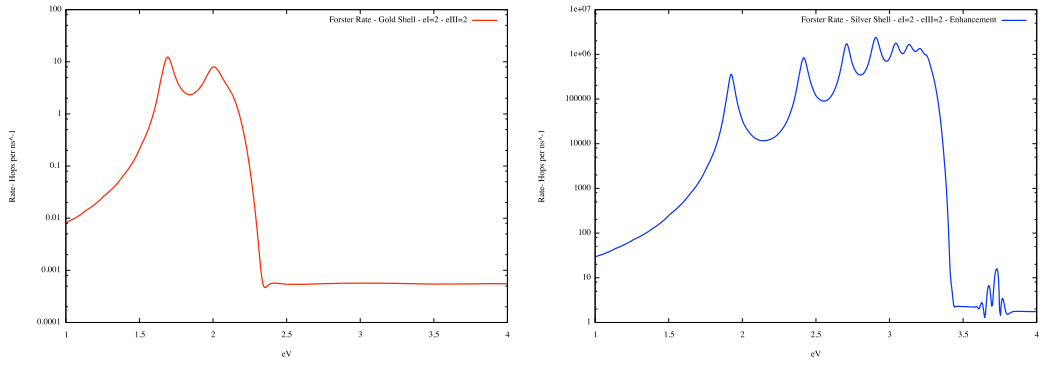

Figure 3.6: FRET rate for both gold and silver shells as a function of frequency in units of eV. The free space FRET rate can be seen in the high frequency limit where the plots saturate.

$l \to \infty$ limit of the SP modes to be,

$$\omega_{sp}^{\pm} = \frac{\omega_p}{\sqrt{1+\varepsilon_I}}, \frac{\omega_p}{\sqrt{1+\varepsilon_{III}}}. \tag{3.31}$$

This effect can be seen in the formation of a second band in the enhancement factor of FRET, corresponding to the in-phase, and out-of-phase modes of SPs at each surface of the shell. Figure 3.7 shows the idealized FRET rate enhancement factor for QDs in the presence of a shell/core MNP. We can clearly see the effect of having two surfaces by the appearance of two SP bands. The dielectric environment inside and outside the shell can be used to tune the spacing between the bands. However, when experimental data for the dielectric function are used (see Fig. (3.6)), the effect is completely washed out in Au MNPs, and greatly reduced in Ag MNPs. But even with losses, Fig. 3.6 shows that Ag MNPs can lead to an enhancement factor on the order of 10 at the peak of the second SP band. While not as impressive as the drastic gains predicted by the lower bands of shell/core MNPs, it's still competitive with the enhancement properties of Au core/shell MNPs. This could be exploited to enhance resonance phenomena at frequencies outside the optical range.

For Au MNPs, the enhancement factor predicted by the model is the same or-

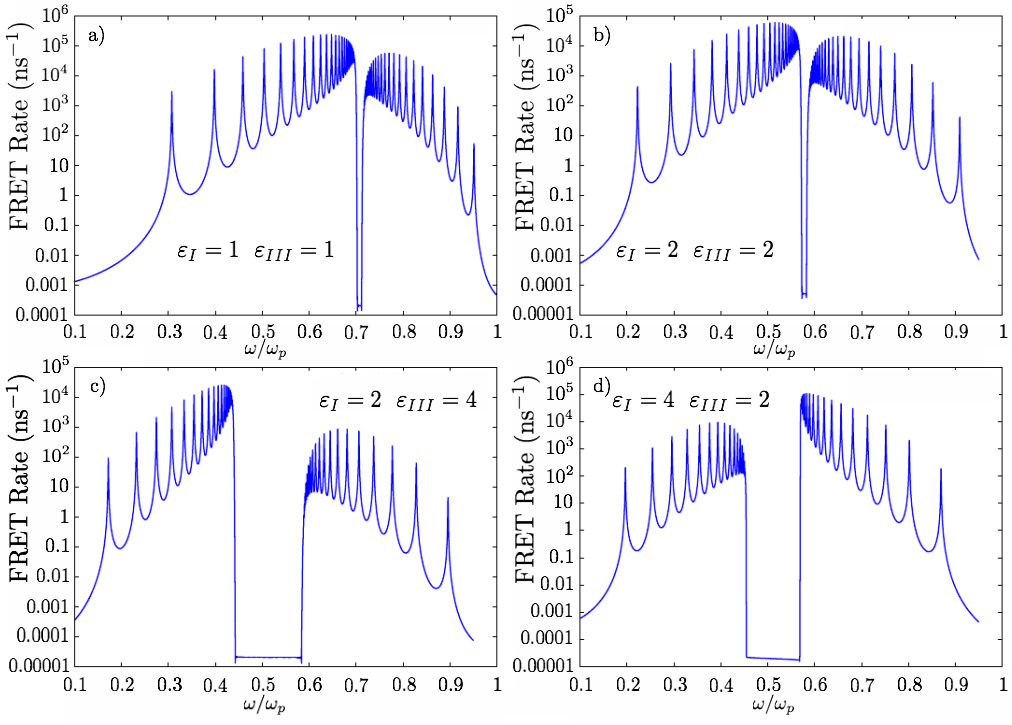

Figure 3.7: Förster rate for shell/core MNPs using the Drude model. Panels a) and b) have the same dielectric constant for inside and outside the metal nanoshell. a) $\varepsilon = 1$ and b) $\varepsilon = 2$. This illustrates the role of the dielectric surroundings in tuning the SP frequency band. Panels c) and d) have inside and outside dielectric constants that differ by a factor of 4. This illustrates the ability of dielectrics to tune each band individually, allowing control of the gap between SP bands for different values of the inner and outer dielectric constants. The aspect ratio was set to 0.85.

der of magnitude for both core/shell and shell/core structures. However, shell/core structures exhibit a clearly distinguishable quadrupole response. This effect is due to the redshift of the SP band caused by environment and geometry. For Au MNPs, these effects move the dipole response of the MNP by about 0.5 eV, allowing for a greater separation between the dipole and quadrupole response.

Figure 3.8 shows how sensitive the multi-polar response of Ag nansoshells is to aspect ratio. As the aspect ratio increases, the nanoshell becomes more like a core/shell structure and we see the multi-polar response of the MNP become evident

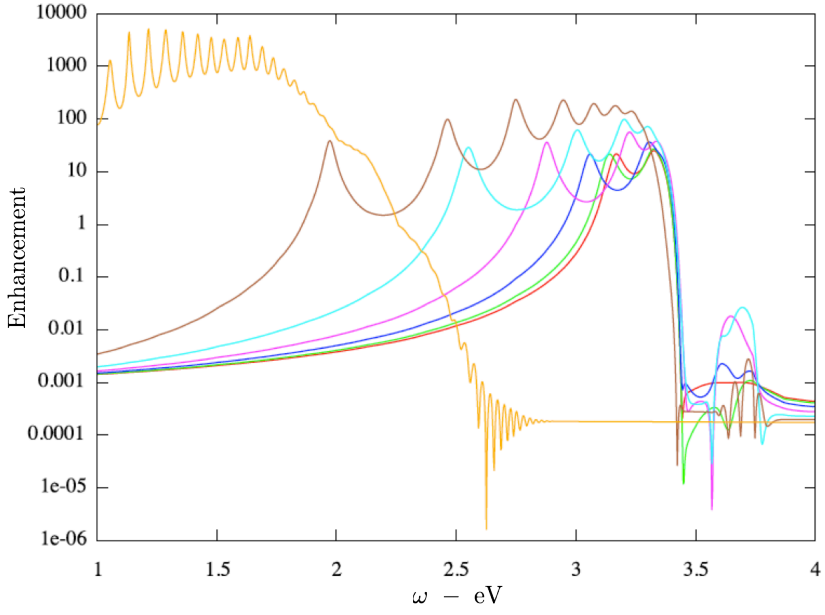

Figure 3.8: FRET enhancement for a Ag nanoshell. Parametric in aspect ratio.

in the enhancement factor of FRET.

3.2.1 Quantum Yield

The Förster transfer mechanism is only one of the several possible energy pathways present in the system. Losses to radiation and heat must also be calculated and compared with the Förster rate. The quantity of interest is often the quantum yield. It is defined as,

$$QY = \frac{\gamma_f}{(\gamma_f + \gamma_m + \gamma_r)}, \tag{3.32}$$

where γ_f is the FRET rate, γ_m is losses to the metal, and γ_r are radiative losses. Radiative losses, can be ignored for nanoparticles with dimensions smaller than the skin depth of the SP layer [Sto11]. An expression for γ_m is related to the imaginary

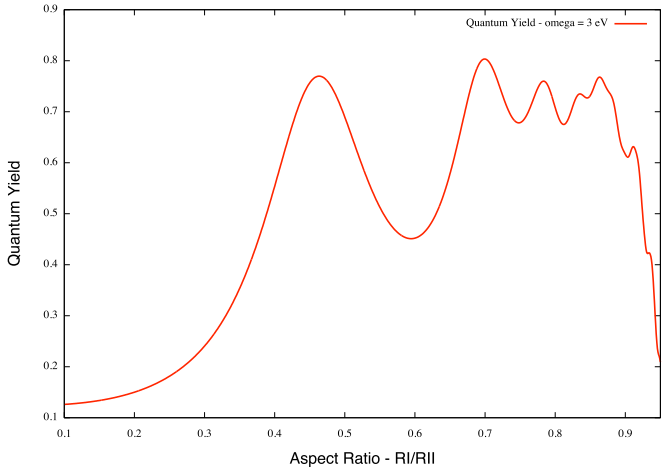

Figure 3.9: Quantum yield as a function of aspect ratio for $\omega - 3$ eV.

part of the total electric field function by, [DRKS08, NH12],

$$\gamma_m = -\frac{|\mu_D|^2}{6\varepsilon_h \hbar a^3} \sum_{l=1}^{\infty} \mathrm{Im}\, F_l(\bar{r}, \omega)(2l+1)(l+1) \left(\frac{a}{r}\right)^{2l+4} . \tag{3.33}$$

Here, $F_l(\omega)$ is the response function of a spherical shell derived in Eq. (2.59). The aspect ratio of nanoshells is known to be a key parameter in determining the response of the system, for example the relationship between SP lifetimes and the aspect ratio of nanoshells was established by Kirakosyan et al. [KSS09]. Figure 3.9 shows the quantum yield as a function of aspect ratio of a Ag nanoshell. Because the aspect ratio tunes the SP frequency, we see an oscillation in the quantum yield corresponding to when system comes into resonance with the FRET rate. Showing how one can mitigate losses due to damping by tuning the characteristics of the MNP and how sensitive the quantum yield is to the geometry of the MNP even, in the presence of damping.

3.3 Conclusion

We have examined the enhancement of FRET due to the image response of MNPs. We have considered several different MNP structures and metals, and have reported on the role of geometry and material in tuning the enhancement factor. Figure 3.10 compares the FRET rate for all MNPs considered in this chapter. The parameters used for Fig. 3.10 are as follows; the FRET rate was calculated at a frequency of, $\omega = 2$ eV and, the dielectric constant was set to $\varepsilon_i = 2$ for all MNPs. The donor QD was placed 2 nm from the surface of the MNP and oriented along the z-axis. The acceptor QD orientation was averaged over all angles. The acceptor QD was kept a fixed distance of 2 nm from the surface, and its position varied in the range of $\theta = 20 - 180$ deg, where θ is the angle made by the center of the MNP to the centers of the QDs. This increased the distance between the QDs while effectively turning FRET into a probe of the electric field near the surface of the MNP. Ag nanoshells produced the highest enhancement and was the most sensitive to variations in the electric field than any of the configurations studied.

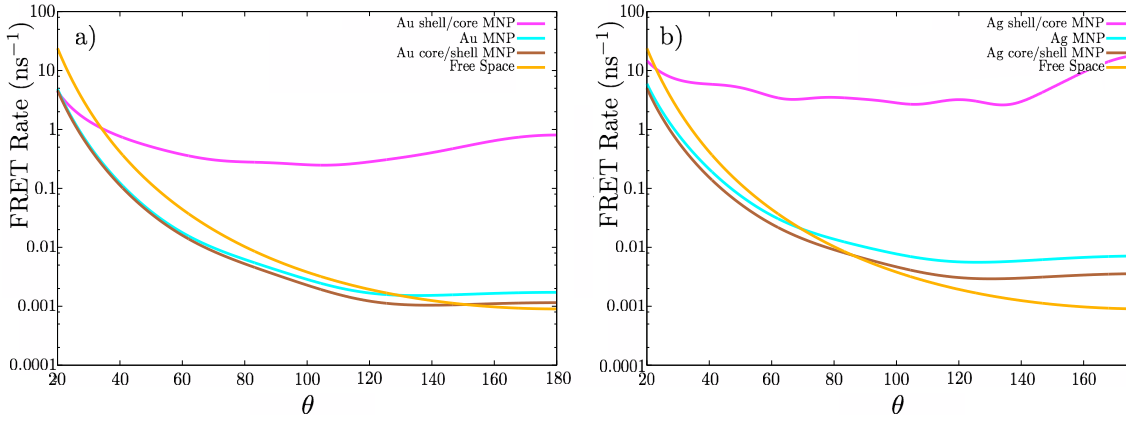

Figure 3.10: Comparison of FRET rates for all three types of MNPs. The results for both a) Au and b) Ag are shown.

Chapter 4

Dynamic Image Force on a Charge Moving above a Metal Plane

4.1 Introduction

We now continue to explore the image response of metal surfaces in the context of non-resonantly driven systems. Recently, a resurgence of interest has emerged in the study the non-driven interactions with metal surfaces. Recent developments in force measurement [SAI13, THW$^+$13, RCJ11, Cle03] and nano-optomechanics [MKZ$^+$08, LRC$^+$10] require a detailed understanding of low energy charge-surface interactions, including quantum effects. Commonly used semi-classical descriptions of SPs are unable to properly account for quantum effects [LTLL12, TMÖ$^+$13], leading to a resurgence in interest quantum mechanical models [ERW$^+$05, TMÖ$^+$13, LTLL12, SHE$^+$12, JS11]. In this Chapter, we begin to address these issues in the context of planar surfaces.

The image force is central to the understanding of classical and quantum surface plasmons (QSP). We begin by considering the back-attraction felt by a charge as it

moves through a dielectric medium, and then we extend the formalism to include the case of a charge moving above a metal slab. We consider the parallel and perpendicular motion separately, and develop a Hamiltonian formalism to describe the dynamics of the charge. We then quantize the system at the level of the Hamiltonian. We then treat the system adibadically in the limit of high QSP frequency as compared to the motion of the charge. We discuss the existence of a zero point repulsion due to the ground state energy of the QSPs. These results are analyzed and checked for self-consistency. We find that the effective potential for motion perpendicular to the plane is inconsistent with adiabatic arguments, showing that existing work on the subject is flawed [ŠTL72, Bar77, SMPP91, NH78].

4.2 Motion of a Charge Through an Electron Gas

Before we address the problem of a charge above a plane, it is illustrative to consider the problem of a charge moving in a dielectric medium. The analysis followed in this chapter is similar to that found in the calculation of dielectric friction [HO77, Zwa70].

Consider a positive spherical charge density $\rho = \frac{q}{4\pi a^2}\delta(r-a)$, of total charge q, distributed uniformly on the surface of a sphere of radius a sitting inside a homogeneous dielectric medium. Suppose that we want to know the induced polarization. The polarization of a material is proportional to the inducing electric field $\mathbf{E}$, by a coefficient independent of direction. In linear response the relation is,

$$\mathbf{P} = \chi \mathbf{E}. \tag{4.1}$$

Taking the divergence of Eq. (4.1) returns an expression for the bound charge density [JF99],

$$\rho_b(\mathbf{r}) = -\nabla \cdot \mathbf{P} = -\frac{\chi q}{4\pi\varepsilon a^2}\delta(r-a)\ ,\ r \geq a. \tag{4.2}$$

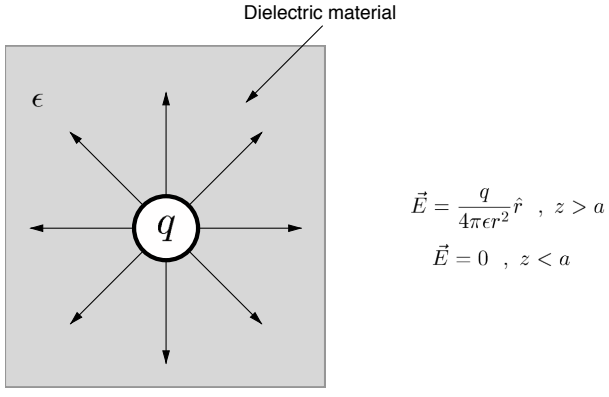

Figure 4.1: A sphere of charge density ρ inside a dielectric medium of relative permittivity ε.

The total charge on the surface of the sphere is then,

$$q_{total} = q(1 - \frac{\chi}{\varepsilon}) = \frac{\varepsilon_0}{\varepsilon} q \tag{4.3}$$

with a total electric field outside of the sphere of,

$$\mathbf{E}_{total} = \frac{q_{total}}{4\pi\varepsilon_0 r^2}\hat{r} = \frac{q}{4\pi\varepsilon r^2}\hat{r}. \tag{4.4}$$

Now let us suppose that we move the sphere to a new location quickly enough that the surrounding material doesn't have a chance to relax. There will be an attraction between the sphere and the disturbance left behind. Initially, there is an attractive force,

$$F_{attraction} = \frac{\chi q^2}{4\pi\varepsilon\varepsilon_0 r^2}, \tag{4.5}$$

pointing in the direction of the residual polarization cloud. After dielectric relaxation, the initial polarization dies away and the back-force goes to zero. At the same time, however, the medium surrounding the new position of the sphere begins to become polarized, becoming fully polarized after some time. If the sphere subsequently moves again, it will again experience a back-attraction, but this time to its new location. Presumably there will be a small lingering back-attraction to its original location.

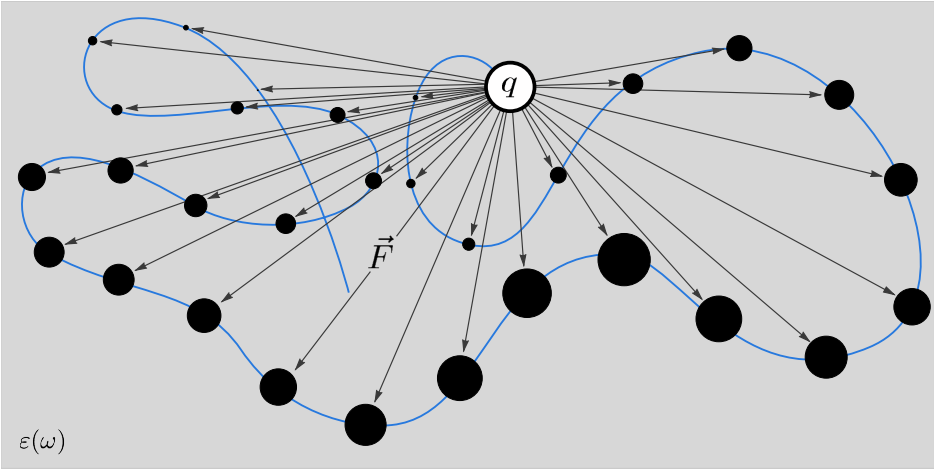

Figure 4.2: Trail of images left along the trajectory of the charge density. The image charges grow and decay away based on the intrinsic properties of the material. The charge density ρ is back attracted to all images that have not decayed.

If you think of the continuous motion of the sphere as being a sequence of abrupt movements, then it is apparent that as the sphere moves through the dielectric, it is back attracted to a dynamical trail of image charges created along its trajectory. The strength of the back-attraction depends on the strength of the image and the distance between the it and the sphere. The strength of images have an initial rise time associated with the dielectric constant of the material, as well as a decay time associated with the material's intrinsic loss mechanisms.

Now suppose that, instead of a sphere, we have a single point charge, moving in space under the influence of the cumulative back-force. The equation of motion for the charge can be found through Newton's second law;

$$m\ddot{\mathbf{r}} + \gamma\dot{\mathbf{r}} = \mathbf{F}_I(t), \tag{4.6}$$

where $\mathbf{r}(t)$ is the position of the charge, $\mathbf{F}_I(t)$ is the image back attraction, m is the mass of the charge, and γ is the damping constant.

To calculate the image force we start by writing down an expression for the total

electric field of the charge and the images.

$$\mathbf{E}_{total} = \frac{q}{4\pi\varepsilon_0}\frac{\mathbf{r}\,' - \mathbf{r}(t')}{\mid \mathbf{r}' - \mathbf{r}(t') \mid^3} + \frac{1}{4\pi\varepsilon_0}\int\limits_{all\ \ space} d^3r''\rho_I(\mathbf{r}\,'')\frac{\mathbf{r} - \mathbf{r}\,''}{\mid \mathbf{r} - \mathbf{r}\,'' \mid^3} \tag{4.7}$$

Here $\rho_I(\mathbf{r})$ is equal to the image charge density. To find the value of $\rho_I(\mathbf{r})$ we must first calculate the polarization vector. In the time domain this is given by a convolution integral,

$$\mathbf{P}(t) = \int\limits_{-\infty}^{t} dt'\chi(t-t')\mathbf{E}(t'), \tag{4.8}$$

where $\chi(t-t')$ is the susceptibility of the medium. Taking the divergence of both sides, we have the following expression for the image charge density;

$$\rho_I(\mathbf{r}', t) = -\int\limits_{-\infty}^{t} dt'\chi(t-t')\nabla'\cdot\mathbf{E}(\mathbf{r}', t') \tag{4.9}$$

Taking Eq. (4.7) and substituting into Eq. (4.9) gives an expression for $\rho_I(\mathbf{r}', t)$,

$$\rho_I(\mathbf{r}', t) = -\frac{1}{4\pi\varepsilon_0}\int\limits_{-\infty}^{t} dt'\chi(t-t')\nabla'\cdot\left[\frac{q(\mathbf{r} - \mathbf{r}(t'))}{\mid \mathbf{r} - \mathbf{r}(t') \mid^3} + \int\limits_{all\ \ space} d^3r''\frac{\rho_I(\mathbf{r}'')(\mathbf{r}' - \mathbf{r}'')}{\mid \mathbf{r}' - \mathbf{r}'' \mid^3}\right]. \tag{4.10}$$

The integrand can be simplified by noting that $\nabla\cdot\dfrac{\mathbf{r}' - \mathbf{r}}{\mid \mathbf{r}' - \mathbf{r} \mid^3} = \delta^3(\mathbf{r}' - \mathbf{r})$, giving an equation for ρ_I,

$$\rho_I(\mathbf{r}\,', t) - \int\limits_{-\infty}^{t} dt'\chi(t-t')\rho_I(\mathbf{r}\,', t) = -q\int\limits_{-\infty}^{t} dt'\chi(t-t')\delta^3(\mathbf{r}' - \mathbf{r}(t)). \tag{4.11}$$

Taking the Fourier transform over time gives,

$$\tilde{\rho}_I(\mathbf{r}') + \tilde{\chi}(\omega)\tilde{\rho}_I(\mathbf{r}') = -q\tilde{\chi}(\omega)\cdot\mathcal{F}[\delta^3(\mathbf{r}' - \mathbf{r}(t))], \tag{4.12}$$

where $\mathcal{F}$ is the Fourier transform operator. Solving this equation and transforming out of Fourier space gives a final expression $\rho_I(\mathbf{r}\,', t)$.

$$\rho_I(\mathbf{r}\,', t) = -q\int\limits_{-\infty}^{t} dt' g(t-t')\delta^3(\mathbf{r}' - \mathbf{r}(t)) \tag{4.13}$$

Here, we have defined the response function as,

$$g(t) = \frac{1}{2\pi} \int_{-\infty}^{t} d\omega \; e^{-i\omega t} \frac{\tilde{\chi}(\omega)}{1 + \tilde{\chi}(\omega)}. \tag{4.14}$$

Recalling that $\tilde{\chi}(\omega) = \epsilon(\omega) - 1$, we find that the response function in Fourier space is,

$$\tilde{g}(\omega) = \frac{\varepsilon(\omega) - 1}{\varepsilon(\omega)}. \tag{4.15}$$

Using the Drude dielectric function and inverting Eq. (4.15) back into the time domain gives an explicit expression for the equation of motion including image effects,

$$m\ddot{\mathbf{r}} = \frac{e^2}{4\pi\epsilon_0} \int_{-\infty}^{t} dt' \omega_p \sin\left(\omega_p(t - t')\right) \frac{\mathbf{r}(t) - \mathbf{r}(t')}{\mid \mathbf{r}(t) - \mathbf{r}(t') \mid^3}. \tag{4.16}$$

Here, $\omega_p = \sqrt{\frac{ne^2}{e\varepsilon_0}}$ is the bulk plasmon frequency.

The problem with Eq.(4.16) is that the singularities when $\boldsymbol{r} = \boldsymbol{r}(t)$ cause divergence in the force, and how these are avoided for real systems becomes the most relevant issue. This issue does not arise for a charge moving external to the polarizable medium, a problem to which we now turn our attention.

4.3 Charge Moving Above a Metal Slab

Consider now the problem of a charge moving above a metal slab. We again solve the time-dependent Poisson equation. Here, the free charge density will consist of a delta-function at the location of the moving point charge,

$$\nabla \cdot \int_{-\infty}^{t} dt' \tilde{\varepsilon}\left(t - t'\right) \mathbf{E}\left(t'\right) = \rho(\boldsymbol{r}) \tag{4.17}$$

For simplicity, we consider motion in the x-direction at some height $z = d$ from the slab. In this case,

$$\rho(\boldsymbol{r}) = e\delta(x - x(t))\delta(y = 0)\delta(z = d). \tag{4.18}$$

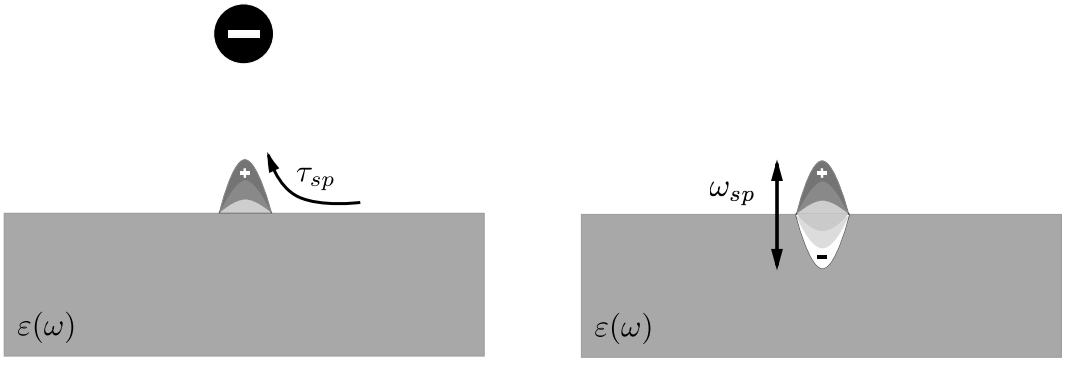

Figure 4.3: Charge density rises on the surface of a metal slab due to the presence of an external charge with a timescale τ_{sp}. If the charge is suddenly removed and damping is ignored the electron density will oscillate at a frequency of ω_{sp}.

Plugging Eq. (4.18) into the r.h.s. of Eq. (4.17) and taking a Fourier transform gives,

$$\nabla \cdot \varepsilon(\omega)\tilde{\mathbf{E}}(\omega) = \mathcal{F}[\delta(x - x(t))]. \tag{4.19}$$

Where $\varepsilon(\omega) = 1 + \tilde{\chi}(\omega)$, is the dielectric function. The Fourier transform of the delta function source term can be written as,

$$\int_{-\infty}^{\infty} dt e^{i\omega t}\delta(x - x(t)) = \int_{-\infty}^{\infty} dt e^{i\omega t} \sum_n \frac{\delta(t - t_n)}{|\frac{dx(t)}{dt}|_{t=t_n}} = \sum \frac{e^{i\omega t_n}}{|\frac{dx(t)}{dt}|_{t=t_n}} \equiv \tilde{f}(x, \omega) \tag{4.20}$$

Where t_n are the roots of $x - x(t) = 0$, and we have made use of the identity $\delta(g(x)) = \frac{\delta(x-x_0)}{|g'(x_0)|}$. After substituting $\tilde{f}(x, \omega)$, the Poisson equation becomes

$$\begin{aligned} \nabla \cdot \varepsilon_0\tilde{\mathbf{E}}(\omega) &= q\delta(y)\delta(z - d)\tilde{f}(x, \omega),\ z > 0 \\ \nabla \cdot \varepsilon(\omega)\tilde{\mathbf{E}}(\omega) &= 0,\ z < 0 \end{aligned} \tag{4.21}$$

To find the electric field we must solve this set of equations subject to the usual boundary conditions,

$$\begin{aligned} \tilde{\mathbf{E}}_{\|} \mid_{z=0^{\dagger}} &= \tilde{\mathbf{E}}_{\|} \mid_{z=0^{-}} \\ \varepsilon_0\tilde{\mathbf{E}}_{\perp} \mid_{z=0^{\dagger}} &= \varepsilon(\omega)\tilde{\mathbf{E}}_{\perp} \mid_{z=0^{-}} . \end{aligned} \tag{4.22}$$

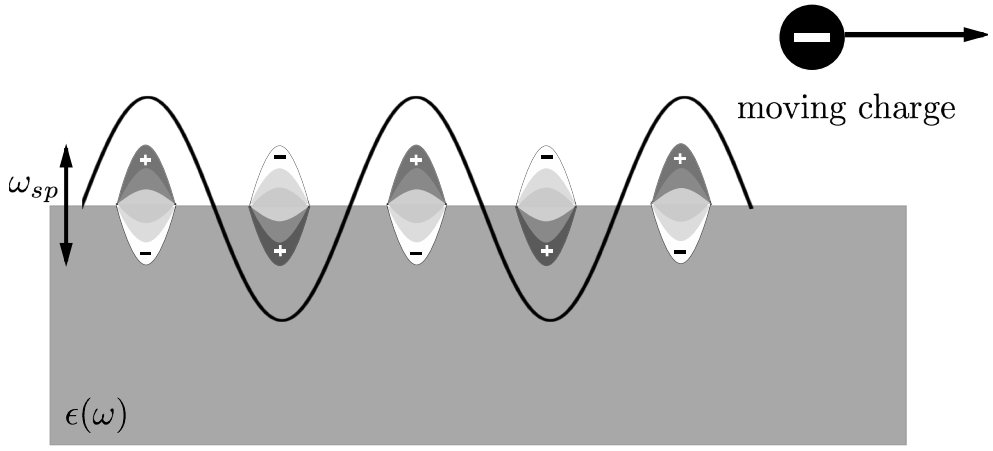

Figure 4.4: Charge density wake set up by a charge moving parallel to the surface of a metal slab. The standing wave structure is a SP that oscillates at a frequency of ω_{sp}.

Rewriting the source term as a superposition of delta functions,

$$\tilde{f}(x,\omega) = \int dx' \delta(x-x')\tilde{f}(x',\omega) \tag{4.23}$$

we see that, in the frequency domain, this dynamical system can be interpreted as the solution to a sum of static electric fields due to the superposition of point charges of strength

$$Q(x',\omega) \equiv Q\tilde{f}(x',\omega). \tag{4.24}$$

These charges are located at x' along a straight line segment parallel to the dielectric. One way to solve for the total electric field is to consider the contribution from each point charge separately and then superimpose these contributions to find the total field. Thus for each point charge at x' we must solve the Poisson equation,

$$\begin{aligned} \nabla \cdot \varepsilon_0 \tilde{\mathbf{E}}(\omega) &= Q(x',\omega)\delta(y)\delta(z-d)\tilde{f}(x,\omega),\ z>0 \\ \nabla \cdot \varepsilon(\omega)\tilde{\mathbf{E}}(\omega) &= 0,\ z<0 \end{aligned} \tag{4.25}$$

subject to the usual boundary conditions. The total electric field in the x direction is therefore,

$$\begin{aligned} \tilde{E_x}(x:x',\omega) &= -\frac{\partial\varphi}{\partial x} \\ &= \frac{Q(x',\omega)}{4\pi\varepsilon_0}\left[\frac{x-x'}{[(x-x')^2(z-d)^2]^{3/2}} - \tilde{g}(\omega)\frac{x-x'}{[(x-x')^2(z+d)^2]^{3/2}}\right]. \end{aligned} \tag{4.26}$$

In writing the total electric field, it is convenient to define a dimensionless response function,

$$\tilde{g}(\omega) = \frac{\varepsilon(\omega)-1}{\varepsilon(\omega)+1} = \frac{\chi(\omega)}{2+\chi(\omega)}. \tag{4.27}$$

Inverting Eq. (4.27) to the time domain gives the total electric field;

$$\begin{aligned} E_x(x,t) &= \frac{e}{4\pi\varepsilon_0}\frac{x-x(t)}{[(x-x(t))^2+y^2+(z-d)^2]^{3/2}} \\ &- \frac{e}{4\pi\varepsilon_0}\int_{-\infty}^{t} dt' g(t-t')\frac{x(t)-x(t')}{[(x(t)-x(t'))^2+(z+d)^2]^{3/2}}. \end{aligned} \tag{4.28}$$

The first term is obviously the field due to the point charge itself, which is located at $x(t)$. The second term with the memory function is the field due to a superposition of image (point) charges at locations $x(t')$ below the dielectric, where $x(t')$ are the positions that the charge has visited in the past. To find the force on the moving charge, we simply pick up the second term of Eq. (4.28). Thus the image force is given by,

$$\begin{aligned} F(x,t) &= qE_{x,image}(x(t),t) \\ &= -\frac{q^2}{4\pi\varepsilon_0}\int_{-\infty}^{t} dt' g(t-t')\frac{x(t)-x(t')}{[x(t)-x(t'))^2+4d^2]^{3/2}}. \end{aligned} \tag{4.29}$$

Now that we have the force we can Newton's equation of motion,

$$m\ddot{x}(t)+\gamma\dot{x}(t) = -\frac{e^2}{4\pi\varepsilon_0}\int_{-\infty}^{t} dt' g(t-t')\frac{x(t)-x(t')}{[(x(t)-x(t'))^2+4d^2]^{3/2}} \tag{4.30}$$

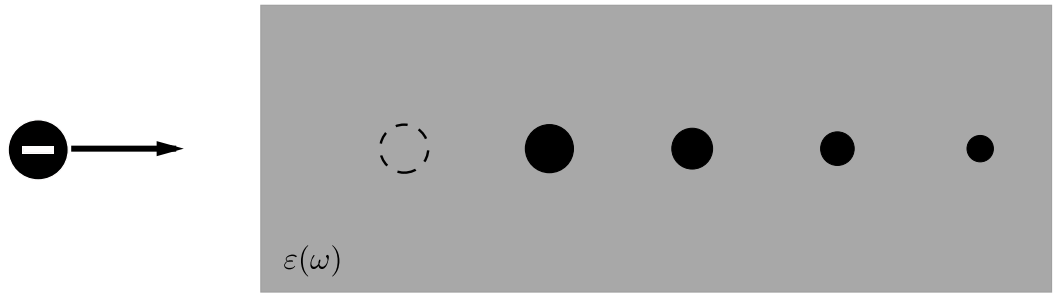

Figure 4.5: image trail of a charge moving perpendicular to a metal slab

Equation of Motion Perpendicular to the Plane

For motion perpendicular to the plane we follow the same procedure but change the rhs of the Poisson to read,

$$\nabla \cdot \int_{-\infty}^{t} dt' \tilde{\varepsilon}\left(t-t'\right) \mathbf{E}\left(t'\right) = e\delta(x=0)\delta(y=0)\delta(z-z(t)) \tag{4.31}$$

Thus, the equation of motion for $z(t)$ is,

$$m\ddot{z} + \gamma\dot{z}(t) = -\frac{e^2}{4\pi\varepsilon_0} \int_0^{\infty} dt' \frac{g(t-t')}{(z(t)+z(t'))^2}. \tag{4.32}$$

The response function is is the same for both the parallel and perpendicular directions,

$$g(t-t') = \mathcal{F}^{-1}\left[\frac{\varepsilon(\omega)-1}{\varepsilon(\omega)+1}\right] = \omega_{sp} e^{-\gamma(t-t')} \sin\left[\omega_{sp}(t-t')\right]. \tag{4.33}$$

The roots of the denominator of Eq. (4.33) define the SP frequency. When the Drude model is used for $\epsilon(\omega)$, we find that

$$\omega_{sp} = \frac{\omega_p}{\sqrt{2}}. \tag{4.34}$$

Integro-differential equations of the form of Eq, (4.32) are difficult to solve due to the non-local nature of the integrand. This motivates us to search for an alternative but equivalent formulation of the problem. We notice the form of kernel Eq. (4.32) is the homogeneous solution to a harmonic oscillator equation and use this as motivation to formulate a Hamiltonian description of the problem.

4.3.1 Hamiltonian Formalism

Here we develop a Hamiltonian representation of a charge moving above a metal plane for motion parallel and perpendicular to the surface of the metal slab.

4.3.2 Motion Perpendicular to the Plane

Let us first consider the motion of the charge perpendicular to the plane. We propose the following Hamiltonian (in the $\gamma = 0$ limit) to describe the motion:

$$H = \frac{\wp^2}{2m} + \sqrt{\frac{e^2 M \alpha_0}{4\pi\varepsilon_0}}\omega_{sp} \int_{n=0}^{\infty} d\alpha_n \; Q_n e^{-\alpha_n z} + \int_{n=0}^{\infty} d\alpha_n \left(\frac{P_n^2}{2M} + \frac{1}{2}M\omega_{sp}^2 Q_n^2\right). \quad (4.35)$$

Here, $\alpha_n = n\alpha_0$, and we will be taking the limit as $\alpha_0 \to 0$. A fictitious oscillator with mass M represents the response of the metal, and ω_{sp} is the SP a frequency. We can check that we retrieve Eq. (4.32) by writing down Hamilton's equations of motion for $z(t)$:

$$\dot{\wp} = -\frac{\partial H}{\partial z} = \sqrt{\frac{e^2 M \alpha_0}{4\pi\varepsilon_0}}\omega_{sp} \sum_n \alpha_n Q_n e^{-\alpha_n z} = m\ddot{z} \tag{4.36}$$

$$\dot{P}_n = -\frac{\partial H}{\partial Q_n} = -M\omega_{sp}^2 \tag{4.37}$$

$$Q_n - \sqrt{\frac{e^2 M \alpha_0}{4\pi\varepsilon_0}}\omega_{sp} e^{-\alpha_n z} = M\ddot{Q}_n \tag{4.38}$$

Formally solving this set of equations for $Q_n(t)$, for the initial conditions, $Q_n(0) = \dot{Q}_n(0) = 0$, we get,

$$Q_n(t) = -\sqrt{\frac{e^2 M \alpha_0}{4\pi\varepsilon_0}}\frac{1}{M}\int_0^t dt' \sin\omega_{sp}(t-t') \sum_n \alpha_n e^{-\alpha_n (z(t)+z(t'))}, \tag{4.39}$$

Substituting Eq. (4.39) into Eq. (4.36) we get,

$$m\ddot{z} = -\frac{e^2 \alpha_0}{4\pi\varepsilon_0}\omega_{sp}\int_0^t dt' \sin\omega_{sp}(t-t') \sum_n \alpha_n e^{-\alpha_n (z(t)+z(t'))}, \tag{4.40}$$

Let us now bring the α_0 inside the summand, let $\alpha_0 \Delta n \to d\alpha$ and convert the sum to an integral. The result is an inverse-square -law,

$$\int_0^\infty d\alpha \alpha e^{-\alpha(z+z(t'))} = \frac{1}{(z+z(t'))^2}, \tag{4.41}$$

with the result that

$$m\ddot{z} = -\frac{q^2}{4\pi\varepsilon_0}\int_0^\infty dt' \omega_{sp} \frac{\sin\omega_{sp}(t-t')}{(z(t)+z(t'))^2} \tag{4.42}$$

Thus we see that the Hamiltonian Eq. (4.36) gives us back the correct equation of motion in the limit $\alpha \to 0$. Realizing this, we could just use the first order Hamilton's equations of motion to solve for the dynamics numerically. However, seeing the problem cast in a Hamiltonian form makes us wonder what, if any, quantum mechanical effects exist.

Quantum mechanical Hamiltonian

We quantize this system by promoting the generalized coordinates to operators and imposing upon them the canonical commutation relations [Dir47].

$$H = \frac{\wp^2}{2m} + \sqrt{\frac{e^2 M \alpha_0}{4\pi\varepsilon_0}}\omega_{sp} \int_{n=0}^{\infty} d\alpha_n \; Q_n e^{-\alpha_n z} + \int_{n=0}^{\infty} d\alpha_n \left(\frac{P_n^2}{2M} + \frac{1}{2}M\omega_{sp}^2 Q_n^2\right) \quad (4.43)$$

With the displacement,

$$Q_n = Q_0 \frac{(b_n + b_n^\dagger)}{\sqrt{2}} \quad (4.44)$$

$$(4.45)$$

and the momentum,

$$P_n = \frac{\hbar}{Q_0}\frac{(b_n - b_n^\dagger)}{\sqrt{2i}}, \quad (4.46)$$

expressed in terms of raising and lowering operators, the Hamiltonian becomes,

$$\begin{aligned} H &= \frac{\wp^2}{2m} + \sqrt{\frac{e^2\alpha_0 M}{4\pi\varepsilon_0}}\frac{Q_0}{\sqrt{2}}\omega_{sp}\sum_n (b_n + b_n^\dagger)e^{-n\alpha_0 z} + \hbar\omega_{sp}\sum_n \hbar\left(b_n^\dagger b_n + \frac{1}{2}\right) \\ &= \frac{\wp^2}{2m} + \hbar\omega_{sp}\sum_n g_n(z)\left(b_n + b_n^\dagger\right) + \hbar\omega_{sp}\sum_n \left(b_n^\dagger b_n + \frac{1}{2}\right) \end{aligned} \quad (4.47)$$

where,

$$g_n(z) \equiv \frac{\omega_{sp}}{\hbar\omega_{sp}}\sqrt{\frac{e^2\alpha_0 M}{4\pi\varepsilon_0}}\frac{Q_0}{\sqrt{2}}e^{-n\alpha_0 z} \tag{4.48}$$

is a dimensionless coupling constant and where $Q_0 = \sqrt{\frac{\hbar}{M\omega_{sp}}}$. is the zero point displacement. We note the Hamiltonian contains a linear coupling to the oscillator coordinates and elect to make the Lang-Firsov (LF) transformation [Kup63, LF63].

A unitary transformation on any operator $\hat{O}$ is defined as [Wag86],

$$e^S O e^{-S} = O + \frac{1}{1!}[S, O] + \frac{1}{2!}[S, [S, O]] + \cdots \tag{4.49}$$

where S is the generating function for the transformation. In the case of LF transformation, $S = i\sum_{n'} g_n(z)(\hat{b}_n - \hat{b}_n^\dagger)$ causes a displacement of the oscillator by the coupling function $g_n(z)$. This displacement of the SP oscillator changes dynamically with respect to the position of the charge, and thus is explicitly dependent on the electron coordinate. This leads to the following set of transformations;

$$\begin{aligned} e^S b_n e^{-S} &= e^{g_n(z)(b_n - b_n^\dagger)} b_n e^{-g_n(z)(b_n - b_n^\dagger)} && (4.50)\\ &= b_n + g_n(z)[b_n^\dagger, b_n] = b_n + g_n(z) \\ e^S z e^{-S} &= z && (4.51)\\ e^{-S}\wp e^{-\hat{S}} &= \wp - \sum_n i\hbar g_n'(z). && (4.52) \end{aligned}$$

Applying this unitary transformation to the Hamiltonian gives,

$$
\begin{aligned}
e^S H e^{-S} &= H = \frac{\left[\wp - i\hbar \sum_n g'_n(z)(b_n - b_n{}^\dagger)\right]^2}{2m} - \hbar\omega_{sp} \sum_n g_n(z)^2 + \hbar\omega \sum_n (b_n^\dagger b_n + \frac{1}{2}) \\
&= \frac{\wp^2}{2m} + \frac{\hbar}{i} \sum_n (b_n - b_n^\dagger)(g_n(z)\wp + \wp g'_n(z) \qquad (4.53) \\
&+ \left(\frac{\hbar}{i}\right)^2 \sum_{n_1 m} g'_n(z) g'_m(z)(b_n - b_n^\dagger)(b_m - b_m{}^\dagger) - \hbar\omega_{sp} \sum_n g_n(z)^2 \\
&+ \hbar\omega_{sp} \sum_n \left(b_n{}^\dagger b_n + \frac{1}{2}\right).
\end{aligned}
$$

The cross term, $(g'_n(z)\wp + \wp g'_n(z))(b_n - b_n{}^\dagger)$, of the extended momentum in Eq. (4.53) will be thrown out in the rotating wave approximation due to the fast motion of the oscillators that vibrate at the SP frequency. The double sum,

$$
\sum_n \sum_m g'_n(z) g'_m(z)(b_n b_m + b_m^\dagger b_n^\dagger - b_m^\dagger - b_n^\dagger b_m - b_n^\dagger b_m), \qquad (4.54)
$$

connects oscillator states of different SP occupation number. It can easily be shown that this term will not contribute if the system is initially in the ground state and the incoming particle energy is much less than a quanta of SP energy. This is effectively an adiabatic argument. We assume that the charge never picks enough energy to cause real transitions between SP eigenstates. If this condition is satisfied, the electron moves in an effective potential,

$$
U(z) = \sum_{n=0}^{\infty} \left(\frac{\hbar^2}{2m} g'_n(z)^2 - \hbar\omega_{sp} g_n{}^2(z)\right), \qquad (4.55)
$$

determined by the spatial extent of the SP-electron coupling function. Let us recall that,

$$
g_n{}^2(z) = \frac{e^2 \alpha_0 M}{4\pi\varepsilon_0} \frac{Q_0^2}{2} \frac{e^{-2n\alpha_0 z}}{(\hbar\omega_{sp})^2} \omega_{sp}^2, \qquad (4.56)
$$

Multiplying by $\hbar\omega_{sp}$ and summing over n gives,

$$\begin{aligned} \hbar\omega_{sp}\sum_{n}^{\infty} g_n^2(z) &= \frac{e^2}{4\pi\varepsilon_0}\sum_{n=0}^{\infty}\alpha_0\Delta n e^{-2n\alpha_0 z}\omega_{sp}^2 \\ &\rightarrow \frac{e^2}{8\pi\varepsilon_0}\int_0^{\infty} d\alpha e^{-2\alpha z} = \frac{e^2}{16\pi\varepsilon_0 z} \end{aligned} \tag{4.57}$$

Upon differentiating $g_n(z)$, we find

$$g'_n(z) = \frac{1}{\hbar\omega_{sp}}\sqrt{\frac{e^2\alpha_0 M}{4\pi\varepsilon_0}}\frac{Q_0}{\sqrt{2}}(-n\alpha_0)e^{-n\alpha_0 z}\omega_{sp}^2 \tag{4.58}$$

$$\rightarrow \sum_n \frac{\hbar^2}{2m}(g'_n(z))^2 = \frac{\hbar e^2}{8\pi m\varepsilon_0\omega_{sp}}\sum_n (n\alpha_0)^2 e^{-2\alpha_0 z} \tag{4.59}$$

$$= \frac{\hbar e^2}{8\pi m\varepsilon_0\omega_{sp}}\int_0^{\infty} d\alpha\alpha^2 e^{-2\alpha z} = \frac{e^2}{16\pi\varepsilon_0}\frac{z_0^2}{4z^3}, \tag{4.60}$$

where $z_0 = \sqrt{\frac{\hbar}{m\omega_{sp}}} \cong 2\mathring{A}$. The effective potential is the sum of two parts,

$$U_{eff}(z) = U_{CL} + U_{QSP} \tag{4.61}$$

The potential,

$$U_{CL}(z) = -\left(\frac{e^2}{16\pi\varepsilon_0}\right)\frac{1}{z} \tag{4.62}$$

is the classical electrostatic image potential, and the potential

$$U_{QSP}(z) = \left(\frac{e^2}{128\pi\varepsilon_0 m\omega_{sp}}\right)\frac{1}{z^3} \tag{4.63}$$

is a repulsive quantum correction. The connection of SPs to the classical image potential is well known [Rit72] result. It is the lowering of the SP ground state energy due to the presence of an external charge. Figure 4.6 plots both components of $U_{eff}(z)$ and their sum.

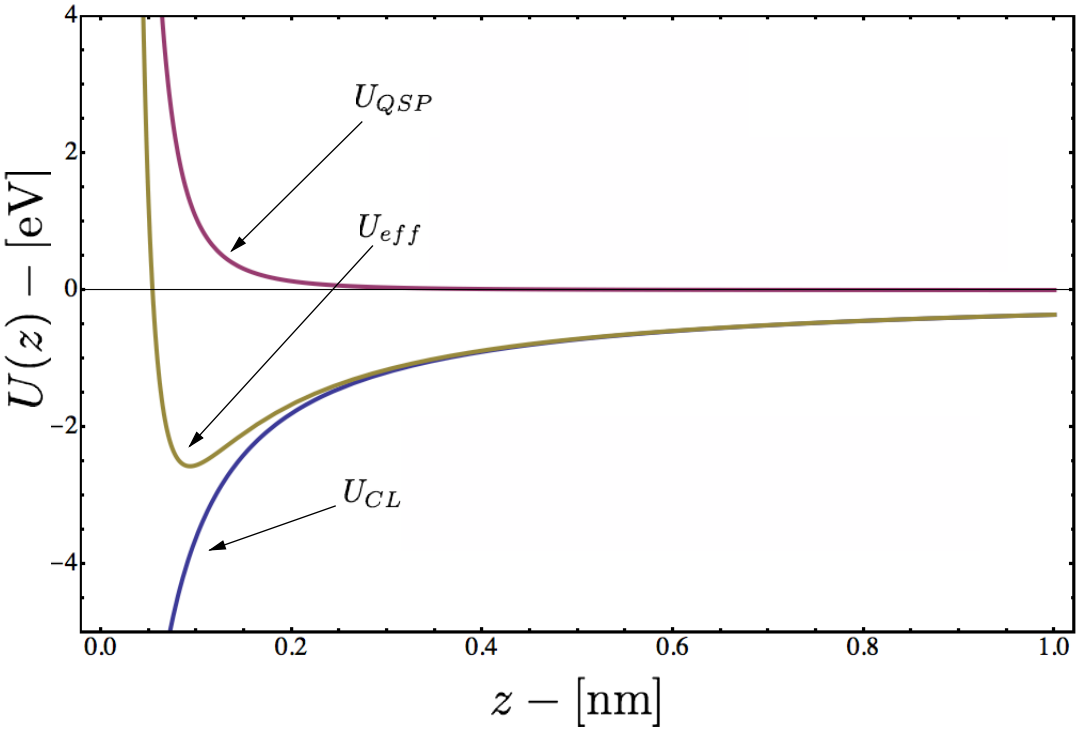

Figure 4.6: Effective potential for motion perpendicular to the plane.

The quantum correction to the image force, U_{QSP}, is repulsive for all values of z. Since this potential is only defined outside of the metal slab, z can only take on positive values. Because it is proportional to $1/z^3$, the repulsion dominates the attraction near the surface.

As the charge approaches the surface it first experiences a long-range attraction due to U_{CL}, but when it reaches within of few $\mathring{A}$s of the surface it feels a zero-point repulsion due to the ground state energy of the QSP. Looking at Fig.4.6, one can't help to notice that the minimum of the U_{eff} is on the order of a few eV's.

We can calculate the amount of energy the particle picks up at the deepest part of the well,

$$U_{min} = -\frac{2}{3}\sqrt{\frac{4}{3}}\left(\frac{e^2}{16\pi\varepsilon_0 z_0}\right) \cong -2\ eV. \tag{4.64}$$

As an electron travels from $x = -\infty$, it will pick up enough energy to excite a SP. This violates the adiabatic assumption under which U_{eff} was derived.

For self consistency, we should also find the frequency of small oscillations in for potential well, and demand that this frequency be small as compared to the plasma frequency ω_{sp}. Setting $\frac{dU}{dz} = 0$ we find the minimum of the potential to be

$$z_{min} = \sqrt{\frac{3}{4}} z_0, \tag{4.65}$$

where $z_0 = \sqrt{\frac{\hbar}{m\omega_{sp}}}$. We then calculate the effective spring constant "K" to find the natural frequency of the bound state.

$$\frac{d^2u}{dz^2}|_{z_{min}} = K = \frac{e^2}{16\pi\epsilon_0}\left(\frac{3z_0^2}{z^5} - \frac{2}{z^2}\right)|_{z_{min}} \tag{4.66}$$

The frequency of small oscillation, ω_0, in this potential well is,

$$\omega_0 = \sqrt{\frac{K}{m}} \approx 3 \text{ eV}. \tag{4.67}$$

Assuming a value of, $\hbar\omega_{sp} \approx 2$eV for the energy of a SP, we can compare the the two energies. We find the ratio,

$$\frac{\hbar\omega_0}{\hbar\omega_{sp}} > 1, \tag{4.68}$$

to be on the order of 1 or larger, whereas for the adiabatic approximation to be valid we require $\frac{\hbar\omega_0}{\hbar\omega_{sp}} << 1$. This finding is in conflict with much of the work done on this topic [Bar77, Bar79, Luc79, MR81, RM72]. Part of the problem is that some authors did not formulate the problem in terms of Hamiltonian dynamics and this left them with a cumbersome integro-differential equation to solve. Some authors tried setting

the electron velocity to be constant [Mil77], but that removes a necessary component of the dynamics. The charge must be able to able to pick up speed. Otherwise the interplay between the long range nature of U_{CL} and the short range nature of U_{QSP} will not occur. Sunjic and Toulouse formulated a quantum mechanical treatment of SPs [ŠTL72], and used perturbative methods to derive the quantum correction. While they arrived at the same result, they did not see the inconsistency of the argument. While they appreciated the perturbative nature of the interaction, their formalism did not explicitly consider any adiabatic arguments.

4.3.3 Motion Parallel to the Plane

Having considered motion perpendicular to the plane, let us now turn our attention to the parallel motion of the charge. The equation of motion for a charge moving parallel to the plane is,

$$m\ddot{x} = \frac{-e^2\omega_{sp}}{4\pi\varepsilon_0}\int_0^t dt' \sin(\omega_{sp}(t-t'))\frac{(x(t)-x(t'))}{[(x(t)-x(t'))^2+(2d)^2]^{\frac{3}{2}}} \tag{4.69}$$

We map this to a Hamiltonian system by using Graf's addition theorem for Bessel functions. It is useful to note the following identities,

$$\begin{aligned}\int_0^\infty dk e^{-2kd}J_0(k(x-x')) &= \frac{1}{\sqrt{(x-x')^2+(2d)^2}} \\ \frac{\partial}{\partial x}\int_0^\infty dk e^{-2kd}J_0(k(x-x')) &= \frac{(x-x')}{[(x-x')^2+(2d)^2]^{\frac{3}{2}}}.\end{aligned} \tag{4.70}$$

Graf's addition theorem states [GRJ+65],

$$J_0(kR) = \sum_{n=-\infty}^{+\infty} J_n(k\rho)J_n(kr)e^{in\varphi} \tag{4.71}$$

where $R = \sqrt{r^2 + \rho^2 - 2r\rho\cos\varphi}$. If $\varphi = 0$, $R = \sqrt{(r^2 + \rho^2 - 2r\rho)} = \sqrt{(r-\rho)^2} = \mid r - \rho \mid$. Let $r = x$ and $\rho = x'$. Therefore,

$$J_0(k(x-x')) = \sum_{n=-\infty}^{+\infty} J_n(kx)J_n(kx') \tag{4.72}$$

$$\int_0^\infty dk e^{-2kd} J_0(k(x-x')) = \sum_{n=-\infty}^{=\infty} \frac{\partial}{\partial x} J_n(kx)J_n(kx') \tag{4.73}$$

$$= \frac{x-x'}{[(x-x')^2 + (2d)^2]^{\frac{3}{2}}} \tag{4.74}$$

Furthermore, we can write the integral over k as a sum. Introducing the factor k_0 so that $k = k_0 m$.

$$\lim_{k_0 \to 0} k_0 \sum_{m=0}^{\infty} \sum_{n=-\infty}^{\infty} e^{-k_0 m 2d} \frac{\partial}{\partial x} J_n(mk_0 x)J_n(mk_0 x') \tag{4.75}$$

$$= \frac{x-x'}{[(x-x')^2 + (2d)^2]^{\frac{3}{2}}} \tag{4.76}$$

Our Hamiltonian is as follows

$$H = \frac{\wp^2}{2m} + \sqrt{\frac{e^2 M k_0}{4\pi\varepsilon_0}}\omega_{sp} \sum_{m,n} e^{-k_0 md} J_n(mk_0 x) Q_{m,n} + \sum_{m,n} \left(\frac{{P_{n,m}}^2}{2M} + \frac{1}{2} M \omega_{sp}^2 {Q_{n,m}}^2 \right) \tag{4.77}$$

This will give the correct equations of motion and represents a free charge interacting with a field of oscillators and is analogous to the Holstein polaron Hamiltonian. To simplify the form of the Hamiltonian we define,

$$g_{n,m}(x) \equiv \frac{\omega_{sp}}{\hbar\omega_{sp}} \sqrt{\frac{e^2 k_0 M}{4\pi\varepsilon_0}} \frac{Q_0}{\sqrt{2}} e^{-k_0 md} J_n(mk_0 x) \tag{4.78}$$

$$P_{n,m} \rightarrow \sqrt{\frac{1}{M\hbar\omega_{sp}}} P_{n,m} \tag{4.79}$$

$$Q_{n,m} \rightarrow \sqrt{\frac{M\omega_{sp}}{\hbar}} Q_{n,m} \tag{4.80}$$

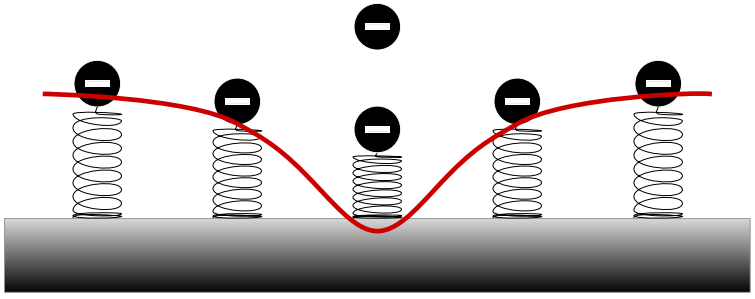

Figure 4.7: Oscillator model a charge moving over a metal slab. The SP response is modeled as a set of oscillators with which the charge interacts.

leading to a more manageable form of the Hamiltonian.

$$H = \frac{\wp^2}{2m} + \hbar\omega_{sp}\sum_{n,m} g_{n,m}(x)(Q_{n,m}) + \frac{\hbar\omega_{sp}}{2}\sum_{m,n}\left(P_{n,m}^2 + Q_{n,m}^2\right) \tag{4.81}$$

Quantum mechanical Hamiltonian

To examine quantum mechanical aspects, let us first write the oscillator coordinates in terms of raising and lowering operators;

$$H = \frac{\wp^2}{2m} + \hbar\omega_{sp}\sum_{n,m} g_{n,m}(x)(b_{n,m} + b_{n,m}^\dagger) + \sum_{n,m}\hbar\omega_{sp}\left(b_{n,m}^\dagger b_{n,m} + \frac{1}{2}\right) \tag{4.82}$$

The same arguments followed for the case of perpendicular motion can be repeated here, leading to the effective Hamiltonian,

$$H_{eff} = \frac{\wp^2}{2m} + U(x) + \hbar\omega_{sp}\sum_{n,m}\left(b_{n,m}^\dagger b_{n,m} + \frac{1}{2}\right), \tag{4.83}$$

where $U(x) = \sum_{n,m}(\frac{\hbar^2}{2m}g'_{n,m}(x)^2 - \hbar\omega_{sp}g_{n,m}^2(x))$. The different structure of the coupling function leads to some different results. The $U(x)$ seen by our moving electron can

be understood by first evaluating the terms in the effective Hamiltonian.

$$\sum_{n,m} g_{n,m}^2(x) = \frac{1}{\hbar^2}\frac{e^2 k_0}{4\pi\varepsilon_0}\frac{\hbar}{\omega_{sp}}\frac{1}{2}\sum_{m=0}^{\infty} e^{-2k_0 md}\sum_{n=-\infty}^{+\infty} J_n^2(mk_0x) \tag{4.84}$$

$$= \frac{e^2}{8\pi\varepsilon_0}\frac{1}{\hbar\omega_{sp}}\frac{1}{2d} \tag{4.85}$$

and,

$$\hbar\omega_{sp}\sum_{n,m} g_{n,m}^2(x) = \frac{e^2}{16\pi\varepsilon_0 d}\sum_{n,m} g'_{n,m}(x)^2 \tag{4.86}$$

$$= \frac{1}{\hbar^2}\frac{e^2 k_0}{4\pi\varepsilon_0}\frac{\hbar}{\omega_{sp}}\frac{1}{2}\sum_{m=0}^{\infty} e^{-2k_0 md}\sum_{n=-\infty}^{=\infty}\left(\frac{d}{dx}J_n(mk_0x)\right)^2$$

Taking $z \to mk_0x$ we recall that,

$$\frac{d}{dx}J_n(mk_0x) = mk_0\frac{d}{dz}J_n(z) \tag{4.87}$$

$$= \frac{mk_0}{2}\left(J_{n-1}(z) - J_{n+1}(z)\right)$$

and that,

$$\sum_{n=-\infty}^{+\infty}\left(\frac{mk_0}{2}\right)^2\left(J_{n-1}^2(z) + J_{n+1}^2(z) - 2J_{n-1}(z)J_{N+1}(z)\right) \tag{4.88}$$

$$= 2\left(\frac{mk_0}{2}\right)^2\left(1 - \sum_{n=-\infty}^{+\infty} J_{n+1}(z)J_{n-1}(z)\right)$$

Shifting the summation index to $n' = n - 1$ results in,

$$\sum_{n'=-\infty}^{+\infty} J_{n'}(z)J_{n'+2}(z) = J_n(0) = 0 \tag{4.89}$$

We see that there is no contribution from this term. Finally,

$$\frac{1}{2}\int_0^\infty dk k^2 e^{-2kd} = \frac{1}{2}\frac{\Gamma(3)}{(2d)^3} = \frac{1}{8d^3} \tag{4.90}$$

$$\frac{\hbar^2}{2m}\sum_{n,m} g'_{n,m}(x)^2 = \frac{e^2}{16\pi\varepsilon_0 d}\frac{1}{8}\left(\frac{d_0}{d}\right)^2 \tag{4.91}$$

where $d_0 = \frac{\hbar}{m\omega_{sp}}$. Thus we find that $U(x)$ is just a constant, independent of x, and so does not affect motion. We should not be surprised because we have nothing that breaks the translational invariance of the system.

Parallel Motion and Effective Mass

We used Graf's addition theorem to obtain the effective adiabatic potential $U_{eff}(x)$ for a charge moving parallel to a metal surface. We found $U_{eff}(x)$ to independent of x, as one would expect from the translational invariance of the problem. Unfortunately, there was apparently no effect whatsoever of the on the motion of the charge. Let us take a closer look at the cross-term produced by the new momentum and see if there are residual effects when we keep it to higher order.

$$H_1 = \frac{\hbar}{2mi}\sum_n (b_n - b_n^\dagger)(g'_n(x)\wp + \wp g'_n(x)) \tag{4.92}$$

$$= \frac{\hbar}{2mi}\sum_n (b_n - b_n^\dagger)(2g'_n\wp - i\hbar g''_n) \tag{4.93}$$

Let us assume that all dynamics are such that SPs remain in their ground states. In such a case, we can define an effective Hamiltonian for the charged particle by carrying out perturbation theory to second order,

$$E = E^{(0)} + E^{(1)} + E^{(2)} + \cdots, \tag{4.94}$$

where,

$$E^{(0)} = \langle 0| H_0 |0\rangle \tag{4.95}$$

$$E^{(1)} = \langle 0| H_1 |0\rangle \tag{4.96}$$

$$E^{(2)} = \sum_{n'} \frac{\langle 0| H_1 |n'\rangle \langle n'| H_1 |0\rangle}{\epsilon_0 - \epsilon_n}. \tag{4.97}$$

Here, $|0\rangle$ is the SP ground state and $|n'\rangle$ represents the product over all SP excited states,

$$|n'\rangle = |n_1\rangle |n_2\rangle |n_2\rangle |n_3\rangle \cdots \tag{4.98}$$

Since $H_1 \propto \sum_n \left(b - b^\dagger\right)$, when we take its ground state expectation value, only singly-excited states of the type; $|0\rangle |0\rangle |0\rangle |n_i\rangle |0\rangle |0\rangle$, with $n_i = 1$, need to be considered. Therefore,

$$E^{(2)} = \left(\frac{\hbar}{mi}\right)^2 \sum_n \frac{\langle 0| (b_n - b_n^\dagger) |1\rangle \langle 1| (b_n - b_n^\dagger) |0\rangle}{\hbar\omega_{sp}} \tag{4.99}$$

$$\times (2g'_n \wp - i\hbar g''_n) (2g'_n \wp - i\hbar g''_n) \tag{4.100}$$

Expanding Eq.(4.99) produces terms proportional to $g'_n g''_n = \frac{1}{2}\frac{d}{dx}(g'_n)^2$, and since $\sum_n (g'_n)^2 = constant$, independent of x, it follows that these terms vanish. We also get terms proportional to $\sum_n (g'_n g'''_n)$ and $\sum_n (g''_n)^2$, that will be independent of x, and are therefore uninteresting for motion in the x direction. These will be ignored. To carry out the sum in Eq.(4.99), recall that,

$$\frac{\hbar^2}{2m} \sum_{n,m} (g'_{n,m}(x))^2 = \frac{e^2}{16\pi\epsilon_0 d} \frac{1}{8} \left(\frac{d_0}{d}\right)^2 \tag{4.101}$$

where $d_0^2 \equiv \frac{\hbar}{m\omega_0}$. An expression for the second order correction in E is,

$$E^{(2)} = \frac{2m}{\hbar^2\omega_{sp}} \frac{e^2}{16\pi\epsilon_0 d} \left(\frac{d_0}{d}\right)^2 \frac{\wp^2}{(2m)^2}, \tag{4.102}$$

plus uninteresting constants. Adding this to $\langle 0| H_0 |0\rangle$, we have

$$H = \frac{\wp^2}{2m^*} + constants, \tag{4.103}$$

where

$$[m^*]^{-1} = \left[1 - \frac{1}{m\omega_{sp}^2}\frac{e^2}{32\pi\epsilon_0 d^3}\right]. \tag{4.104}$$

Thus, the effective mass Hamiltonian is,

$$H = \frac{\wp^2}{2\frac{m}{[1 - \frac{1}{m\omega_{sp}^2}\frac{e^2}{32\pi\epsilon_0 d^3}]}} \tag{4.105}$$

Notice that, even though we are keeping the zero-pt. motion of the SPs, the effective mass does not depend on $\hbar$. Also, the lighter the mass of the electron, the more important the mass correction. That is, $m^* \to \infty$ as $m \to 0$. (Specifically, when $m = \frac{32\pi\epsilon_0 d^3\omega_0^2}{e^2}$, $m^* = \infty$.) For $\omega_{sp} = 10^{15} sec^{-}1$, and $m = 9.1 * 10^{-31}$ kg, $\frac{1}{m\omega_{sp}^2}\frac{e^2}{32\pi\epsilon_0 d^3} \cong 0.04$ at $d = 1$ nm, a small correction to the electron mass.

4.4 Conclusion

We have analyzed the problem of a charge moving above a metal slab. We established a quantization procedure for near field QSPs. We also showed that for motion parallel to the plane that quantum correction to the classical image force is inconsequential. For motion perpendicular to the plane, we found that the results of an adiabatic expansion of the Hamiltonian fail to be self-consistent with the adiabatic limit under which it was derived. Our results are in conflict with those established by others [Sun72, RM72, Rit72]. Future research in this field should include the bosonic nature of QSPs as it relates to multiple excitations of SPs, electron-QSP scattering rates and electron-QSP interaction in resonantly driven systems. Furthermore, though the

relationship between ground state QSPs and the image force is known [Rit72, EN74], a careful review of current literature shows that this is an unappreciated subtlety.

Chapter 5

Dynamical Image of a Charge Moving Towards a Metal Sphere

5.1 Introduction

The optical absorption and scattering of light off ensembles of small metal particles was first considered by Gustav Mie in 1908 [Mie08] to explain the experiments of Steubing [GH09]. The problem was also addressed by Debye [Deb10], who calculated the mechanical pressure exerted upon the a spherical particle by the incoming light. Mie's solution to the problem has dominated the modeling of light scattering off small particles due to its ability to correctly predict resonances in the absorption coefficient of the scattered light. We refer the reader to the works by Stratton [Str07] for a comprehensive overview of the theory and to the book by Kreibig [VK95] for an overview of the optical properties of metal clusters in a modern context. From a modern perspective it was through the experiments of Doremus [Dor64] and the pioneering theoretical work of Kawabata and Kubo [KK66, Kub62] that the connection between plasmons and the absorption spectra was understood. Kawabata and Kubo used linear response theory to explain the widths of the absorption reso-

nances in terms of plasmon decay into single electron-hole excitations and radiative decay. The excitation of plasmons on spheres through interaction with nonrelativistic electrons wasn't considered until 1967 by Fujimoto [FKI67] and also separately by Ritchie [CR68] a year later. These sphere plasmons were immediately attractive since radiative decay of SPs is allowed without the need of surface roughness as in the case of planar geometries. Experimental verification of the radiative decay of spherical SP's followed the next year [KZ70].

In the early days of the field much of the theoretical and experimental focus centered on the observation and characterization of ensembles of metal clusters. However, the coming of age of nanoscale fabrication has made the manufacturing, control, and observation of single metal nanoparticles [Sön01, KPG$^+$98] a reality. While there has always been some interest in the field of plasmons localized to small particles, it wasn't until the observation of single molecules using surface enhanced Raman spectroscopy (SERS) [KWK$^+$97, NE97] that interest in the field exploded. SERS uses the intense electric (near) fields of MNPs to enhance the Raman scattering rate. This observation motivated further exploration of how to exploit the intense electric near fields of localized SPs (LSP), and set the stage for subwavelengths optics [GTG$^+$98, ELG$^+$98, BVD$^+$06, BDE03], .

The coupling of semiconductors to plasmonic systems has also become an active field of research [BS03, BS04, LLSB05, SFB02, YLZ$^+$13, ANP$^+$13], particularly with respect to the coherent amplification of near fields [SFB02]. Most applications of LSPs use either a laser or fast electrons as the exciting field source. Due to the high energies and relatively large sizes involved, a classical description of LSPs was seen as adequate for many years. Recently, there has been a growing interest in the quantum nature of LSPs [ES, CPD13, SGEKD13, TMÖ$^+$13, LTLL12, MKN$^+$12, SHE$^+$12, SKD12]. In this Chapter we want to focus on the implications of a quantum LSP, with an eye towards potential applications in the growing fields of nanomechanics [Cle03] and nanoelectronics.

We consider a model system of a SWNT coupled to a single MNP and examine the effect QSPs have on the transport properties of charge carriers in SWNTs. We model the SWNT by considering the charge carrier to be an electron confined to move in one dimension. We consider the MNP as a perfect sphere; using the Drude dielectric function to model its material properties. By using the tools built in previous chapters, we find that the first correction to the classical image force is a quantum repulsion. Furthermore, we find that due to the properties of SWNTs and QSPs, when the QSP remains in its ground state, a charge can feel a repulsion comparable to the classical image force. We frame the repulsive term in the context of ponderomotive forces and provide a new interpretation of zero point SP effects.

5.2 Charge Motion in the Presence of a Metal Sphere

Let us assume that a MNP is situated downstream and below a moving charge. As the charge approaches the sphere, the metal responds by forming image charges on its surface. Let us assume that the spatial extent of the system is less than a wavelength of optical light, and carry out our calculations neglecting retardation effects due to the speed of light. We build the response function in the same way that we have in previous chapters, by solving the electrostatic Poisson equation and replacing the static response with its frequency dependent analogue. We are concerned, as we were in the case of a plane geometry, with how the dynamics of the moving charge are modified by the interaction with the metal. We assume that the spatial extent of the system is less than the wavelength of optical light and carry out our calculations neglecting retardation effects due to the speed of light. We build the response function in the same way we have in previous chapters by solving the electrostatic Poisson equation and replacing the static response with its frequency dependent analogue. We are concerned, as we were in the case of a plane geometry,

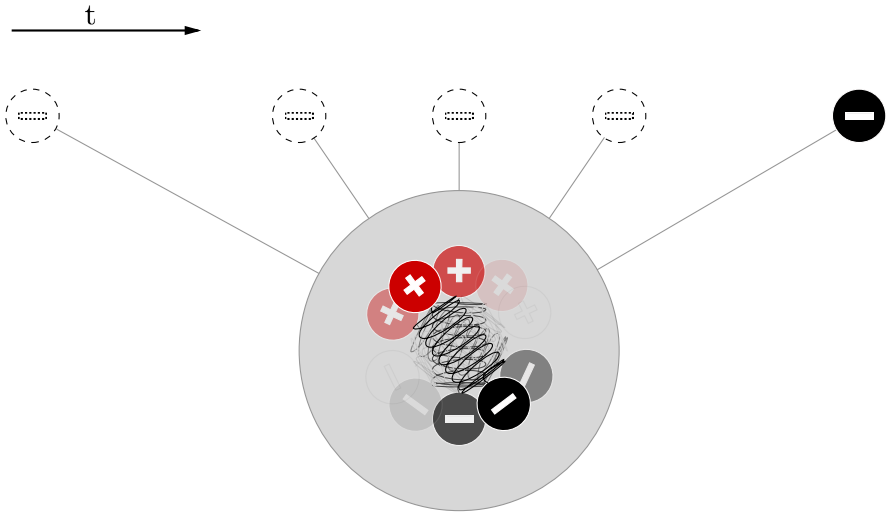

Figure 5.1: Schematic of time dependent response of a metal sphere due to a moving charge. As the charge approaches the MNP, it seeds images. These images grow to some maximum value and decay away. If they are given some initial energy, they oscillate with a frequency of ω_{sp}.

with how the dynamics of the moving charge are modified by the interaction with the metal.

5.2.1 Linear Response of the Sphere

To solve this problem we need the equation of motion of a moving charge in the presence of the metal sphere. Figure 5.1 is a schematic of the system. As a reaction to the electric field of the charge, the metal forms a surface state, which from the perspective of a point outside the sphere is equivalent to a set of oscillators located within the sphere. Each dipole formed in the body of the sphere has both a rise and decay time associated with the solid-state properties of the metal. As the charge passes by the sphere the back-force felt by the charge at a later time is due to the distance between it and all the images located in the sphere, as well as their strength.

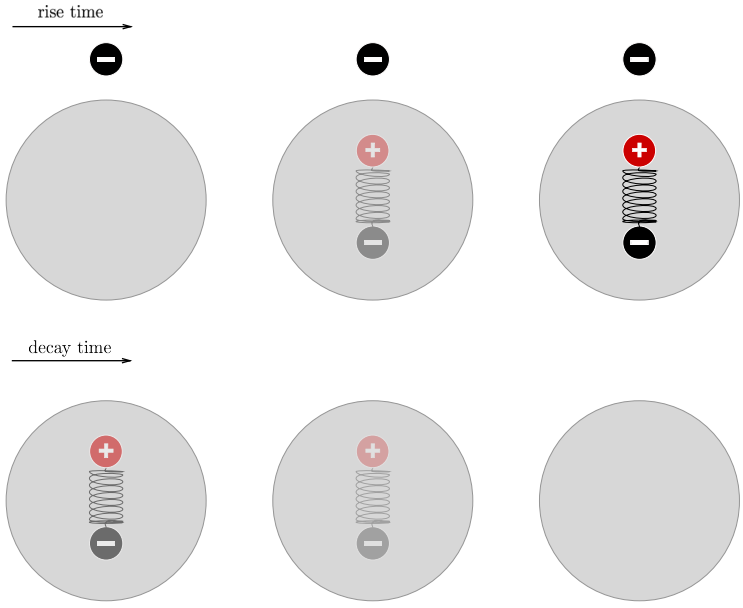

Figure 5.2: Time delayed response of a metal sphere due to a stationary charge. Time moves from left to right. If we place a charge in front of a metal sphere, the image dipole rises on a timescale associated with ω_{sp}. In the second row, we have removed the charge, and the image dipole decays away on a timescale associated with the damping mechanisms of the metal.

This is completely analogous to the case of a charge moving above a plane with the exception that the images are now localized. With this description in mind, our goal is to find a solution to the following equation,

$$m\ddot{x} = F_x(x,t) = -q\nabla_x \varphi^I(x,t). \tag{5.1}$$

Here, $\varphi^I(x,t)$ is the image potential induced by the presence of the charge, m is the mass of the incoming particle, and q is the net charge. The gradient defining the image electric field on the right hand side of the equation is only taken in the direction the particle is constrained to move in, since we only care about the forces in that direction.

In order to get $\varphi^I(x,t)$, we solve the time dependent Poisson equation. The total force is the contribution of all images laid by the particle during its history of

interaction with the metal up to the present moment in time. The Poisson equation is

$$\nabla \cdot \int_{-\infty}^{t} dt' \tilde{\varepsilon}\,(t-t')\,\mathbf{E}\,(x,t') = \rho(t), \tag{5.2}$$

where we have defined the free charge density $\rho(\mathbf{r})$ as,

$$\rho(\mathbf{r},t) = q\delta(x-x(t))\delta(y)\delta(z-d). \tag{5.3}$$

Here, $\mathbf{E}$ is the total electric field $\mathbf{E} = \mathbf{E}^e + \mathbf{E}^I$, with $\mathbf{E}^e$ and $\mathbf{E}^I$ being the source electric field of the incoming particle and the image field, respectively. Using the Green function solution found in Eq. (2.54), and multiplying by $\frac{q}{4\pi\epsilon_0}$, we get an expression for the total electrostatic potential,

$$\varphi(\boldsymbol{r},\boldsymbol{r}') = \frac{q}{4\pi\varepsilon_0}\left[\frac{1}{\mid \mathbf{r}-\mathbf{r}' \mid} - \sum_{l=1}^{\infty}\frac{l(\varepsilon-\varepsilon_0)}{l(\varepsilon+\varepsilon_0)+1}\frac{a^{2l+1}}{r'^{l+1}r^{l+1}}P_l\cos\gamma\right]. \tag{5.4}$$

Here, $\cos\gamma = \cos\vartheta\cos\vartheta' + \cos\vartheta\sin\vartheta'\cos(\varphi-\varphi')$ is defined as the angle between the source charge located at $\boldsymbol{r}'$, and $\boldsymbol{r}$ is the location where we require knowledge of the potential. P_l are the Legendre polynomials, defined for integer values of l. Invoking the quasistatic approximation, we replace ε with $\varepsilon(\omega)$. The potential is thus,

$$\varphi(\mathbf{r};\omega) = \frac{q}{4\pi\varepsilon_0}\left[\frac{1}{\mid \mathbf{r}-\mathbf{r}' \mid} - \sum_{l=1}^{\infty}\tilde{g}(\omega;l)\frac{a^{2l+1}}{r'^{l+1}r^{l+1}}P_l\cos\gamma\right]. \tag{5.5}$$

Here, as usual, we have defined the dimensionless response function,

$$\tilde{g}(\omega;l) = \frac{l(\varepsilon(\omega)-1)}{l(\varepsilon(\omega)+1)+1}. \tag{5.6}$$

Using the Drude dielectric function Eq. (2.10), we write down an explicit expression for the motion of a single charge under the influence of the image electric field in the time domain;

$$\begin{aligned} m\ddot{x}(t) &= \frac{e^2}{4\pi\varepsilon_0}\int_{-\infty}^{t} dt'\nabla\sum_{l,m}^{\infty} e^{-\gamma_l(t-t')} \\ &\quad \times\omega_l\sin\left[\omega_l(t-t')\right]\frac{a^{2l+1}}{r\,(t')^{l+1}\,r\,(t)^{l+1}}Y_{l,m}(\theta(t),\phi(t))Y^*_{l,m}(\theta(t'),\phi(t')). \end{aligned} \tag{5.7}$$

Let us only consider the dipole response of the sphere and take $l = 1$. In such a case we obtain,

$$\ddot{x}(t) = 4\pi\varepsilon_0 a^3 \omega_{sp} \int_{-\infty}^{t} dt' e^{-\gamma(t-t')} \sin\left(\omega_{sp}(t-t')\right)(\nabla_x \mathbf{E}^e(x(t)))\mathbf{E}^e(x(t')). \quad (5.8)$$

Here t is the present time, and t' the past time. We would like to find the Hamiltonian that reproduces the dynamics predicted by Eq. (5.8), but as a set of first ordered coupled equations instead of a second order integro-differential equation of the form of Eq. (5.8). This would not only make the problem easier to solve numerically, but would also give us some insight into the underlying mechanics at play and set the stage for a quantum mechanical description of the system.

5.3 Classical Hamiltonian Description

We know that the kernel of Eq. (5.8) is the solution to a harmonic oscillator equation with natural frequency ω_{sp}. The oscillator is driven by the external force caused by the electric field of the charge. In dimensionless units, a Hamiltonian for the electron-SP is

$$H = \frac{\Delta}{2}\wp^2 + \frac{1}{2}\sum_n \left(P_n^2 + Q_n^2\right) - \sum_n Q_n g_n(x). \quad (5.9)$$

Here, n is the number of oscillators needed to model a three-dimensional dipole and

$$g_n(x) = \sqrt{\frac{e^2}{4\pi\varepsilon_0 a\hbar\omega_{sp}}}\left(\frac{a}{d}\right)^2 f_n(x) \quad (5.10)$$

is the spatially dependent coupling, and $\Delta = \frac{\hbar^2}{md^2}/(\hbar\omega_{sp})$. The function $f_n(x)$ is the dimensionless and unit free function associated with the three Cartesian components of $\mathbf{E}^I$, a is the radius of the sphere, d is the distance of the charge from the center of the sphere, and $\omega_{sp} = \omega_p/\sqrt{3}$ is the SP frequency.

Recall that the expansion in Legendre polynomials is related to spherical harmonics through the addition theorem (Eq.(2.53)). Therefore, the $l = 1$ term in Eq. (5.4) has a degeneracy of $2l + 1 = 3$. These are the three degenerate oscillators needed to model the dipole response of the sphere in three dimensions. Because the charge is constrained to move in one dimension, we only need two oscillators to describe the tracking of a charge by the image dipole. In the Legendre polynomial representation, the two terms appear when $\cos\gamma$ is written in Cartesian representation with $z = d$ and $y = 0$. It can be easily verified that, by integrating out the oscillator coordinates, one regains Eq. (5.8) under the condition that $Q_n(0) = 0$ and $P_n(0) = 0$. Hamilton's equations of motion for this system are as follows:

$$\begin{aligned} \dot{x} &= \frac{\partial H}{\partial \wp} = \wp \\ \dot{\wp}_n &= -\frac{\partial H}{\partial x} = Q_n \nabla_x g_n(x) \\ \dot{Q}_n &= \frac{\partial H}{\partial P_n} = P_n \\ \dot{P}_n &= -\frac{\partial H}{\partial Q_n} = g_n(x) - Q_n \end{aligned} \tag{5.11}$$

5.3.1 Numerical Simulation

To regain Eq. (5.8) from the Hamiltonian in Eq.(5.9), it was necessary to assume that the oscillator had no initial energy. The coupling is rooted in the image response of the sphere so that, as the charge comes in from far away, the SP oscillator slowly deforms as it approaches. Under these conditions the dynamics are uninteresting. However, now that we see this problem from the vantage point of a Hamiltonian system, it is tempting to ask what happens when the oscillator does have some initial energy.

Figure 5.3 shows the simulation results of Eq.(5.12) as a function of dimensionless initial velocity. We have also given the oscillator some initial energy equal to $\frac{1}{2}$ in

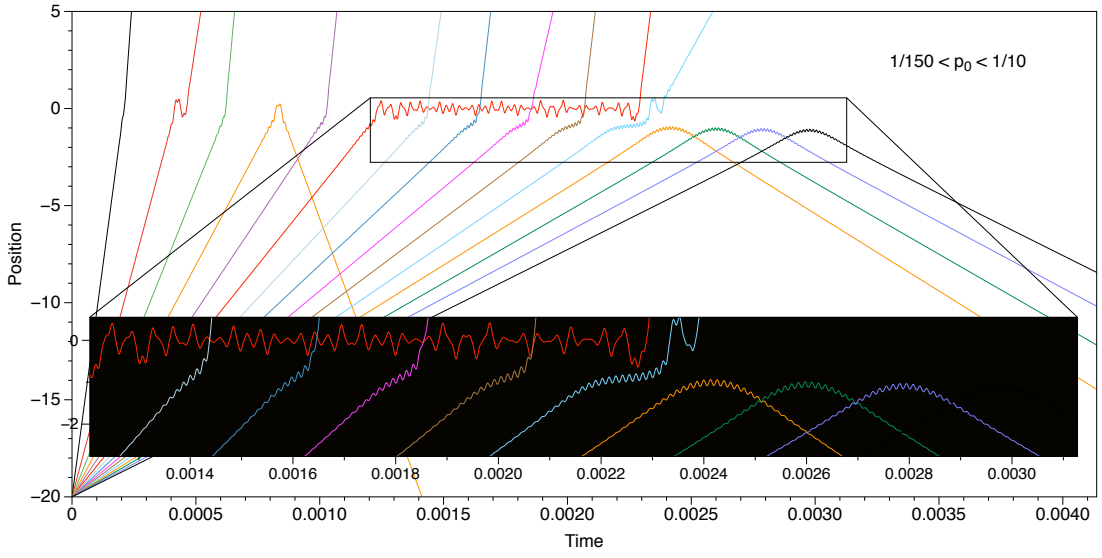

Figure 5.3: Plot of position versus dimensionless time parametric in incoming initial momentum. The plots are the far left are for incoming electron momentum on the order of $\hbar\omega_{sp}/10$. As we move to the right each trajectory plotted represents a lower incoming momentum.

dimensionless units. In comparison, the range of initial momentum given to the moving electron in Fig. 5.3 is $\frac{1}{10} < v < 1/100$. It was also necessary to give a value of the dimensionless constant $\Delta = 2$.

Trajectories for different initial velocities are shown in Fig.5.3. When the momentum is high, the particle simply shoots past with little change. As we lower the initial velocity, the dynamics become complex and we see a variety of behaviors stretching from bound, reflection, transmission, or a mixture of all three. We even see situations where the charge leaves with less energy than it came it with or vice-versa. If we want to understand the dynamics of this system in terms of a simple effective Hamiltonian, we have to stay clear of the more complex behavior for the moment. As we decrease the incoming energy, we see the formation of what appears to be adiabatic behavior. In this regime the particle comes in, begins to wiggle and is reflected back with the same energy as it started with. We anticipate that it will

be possible to adopt an adiabatic description of the motion in this parameter range. Furthermore, the oscillation of the electron "wiggle" can be checked and is found to be in resonance with the ω_{sp}. This is quite interesting since we began this discussion emphasizing the lack of resonant phenomena in the system. It seems that the interaction has induced its own resonance. Our goal is to derive an effective Hamiltonian for the system in this limit and analyze both the classical and quantum dynamics of the charge.

5.3.2 Adiabatic Expansion

Turning our focus back to the Hamiltonian in Eq. (5.9), we notice a resemblance to the Fröhlich [Frö54] electron-lattice coupling Hamiltonian found in polaron theory [Hol59] and other related electron-lattice coupling theories [BP55]. Generally the Hamiltonians studied in those systems are translationally invariant, and as we will see, the loss of this symmetry will complicate matters.

The strategy we follow is to look for the set of canonical transformations that get us to an adiabatic representation. For simplicity, consider only one oscillator oriented in the z direction.

$$H = \frac{\Delta}{2}\wp^2 + \frac{1}{2}\left(P^2 + Q^2\right) - Qg(x) \tag{5.12}$$

where $\Delta = \frac{\hbar^2}{md^2}/(\hbar\omega_{sp})$ and $g(x) = \sqrt{\frac{e^2}{4\pi\varepsilon_0 a\hbar\omega_{sp}}}\left(\frac{a}{d}\right)^2 \frac{1}{(1+x^2)}$ is the coupling for a $\hat{\boldsymbol{z}}$-oriented dipole perpendicular to the motion of the charge.

First let's focus on the linear coupling between the oscillator coordinate and the dimensionless electric field $g(x)$, which we will henceforth refer to as an influence function. Given the similarities between this and the polaron Hamiltonian, we are tempted to look to that theory for clues on how to begin our analysis. A common place to start is to perform a displaced oscillator transformation and try and remove the linear coupling [LF63]. One doesn't need prior knowledge of the polaron to know

that completing the square in Q will get rid of the linear term. Doing so gives,

$$H = \frac{\Delta}{2}\wp^2 + \frac{1}{2}P^2 + \frac{1}{2}\left(Q - g(x)\right)^2 - \frac{1}{2}g(x)^2 \tag{5.13}$$

In Eq. (5.13) what usually plays the role of the polaron lowering energy $g^2/2$ is the square of the influence function, and due to the dependence of g on x, it appears as a potential term in the Hamiltonian. In polaron theory one is more accustomed to seeing this term as a constant. The spatial dependence of the coupling has some important consequences, as we will soon see. The form of the Hamiltonian after completing the square indicates that the displaced coordinate $Q-g(x)$ is the preferred frame of reference. To properly perform a coordinate transformation at the level of a Hamiltonian we write down a generating function that relates the old and new variables. Following Goldstein [Gol62], we propose a generating function of the form,

$$F_1 = -\left(Q + g(x)\right)\tilde{P} - q\tilde{\wp}. \tag{5.14}$$

The set of equations which relate old and new variables through the generating function are,

$$\tilde{x} = -\frac{\partial F_1}{\partial \tilde{\wp}} = x \tag{5.15}$$

$$\tilde{Q} = -\frac{\partial F_1}{\partial \tilde{P}} = Q + g(x) \tag{5.16}$$

$$\wp = -\frac{\partial F_1}{\partial q} = \nabla g(x)\tilde{P} + \tilde{\wp}. \tag{5.17}$$

We now write our new Hamiltonian in terms of our old variables to get,

$$\mathcal{H} = \frac{\Delta}{2}\left(\wp - \nabla g(x)P\right)^2 + \frac{1}{2}\left(P^2 + Q^2\right) - \frac{1}{2}g(x)^2. \tag{5.18}$$

There are a few things to notice about the form of the Hamiltonian in Eq. (5.18). The first thing, as we already noted, is the polaron lowering energy as a potential term

in our Hamiltonian. In actuality, this term is nothing more than the classic image potential of a charge placed in front of a dielectric sphere. Another, and perhaps more interesting feature, is that the spatial dependence of the influence function has resulted in an extended momentum, consistent with transforming into an accelerating reference frame. So while our transformation did remove the linear coupling to Q it replaced it with a coupling between the charge and oscillator momenta. Focusing on the adiabatic limit of Fig. 5.3, we identify two timescales associated with the motion of the charge; a fast oscillatory motion, and a slow translational motion. The fast "wiggles" are due to the fast optical frequencies of ω_{sp}, and the slow translational motion of the particle is due to initial conditions and the long range coulomb potential $-\frac{g(x)^2}{2}$.

Action angle variables

It makes sense to introduce action angle variables when searching for adiabatic arguments having to do with separation of time scales, but since we will intend to treat this system quantum mechanically we should be careful not to over-learn any lessons gained. Any results results coming from an action angle variable representation cannot be quantized [SSS94] because they represent cyclic variables in phase space. Keeping this in mind, we proceed with a classical analysis by introducing action angle variables,

$$P = \sqrt{2\mathcal{J}}\sin\varphi$$
$$Q = \sqrt{2\mathcal{J}}\cos\varphi$$

where $\mathcal{J} = \frac{1}{2}(P^2 + Q^2)$ is the action, the radius of the circle in phase space. The action angle variable Hamiltonian is

$$H = \frac{\Delta}{2}\wp^2 + \frac{1}{2}\left(\Delta(\nabla g(x))^2\mathcal{J}\sin^2\varphi - g(x)^2\right) + \frac{\Delta}{2}\sqrt{\mathcal{J}}\nabla g(x)\wp\sin\varphi + \mathcal{J} \quad (5.19)$$

Interaction Picture Transformation

We perform another transformation to bring in the explicit time dependence of the SP. The generating function for this transformation is,

$$F = \mathcal{J}(\varphi - t), \tag{5.20}$$

giving rise to a new Hamiltonian,

$$\mathcal{H} = \frac{\Delta}{2}\wp^2 + \frac{1}{2}\left(\Delta(\nabla g(x))^2 \mathcal{J}\sin^2(\varphi - t) - g(x)^2\right) + \frac{\Delta}{2}\sqrt{\mathcal{J}}\nabla g(x)\wp \sin(\varphi - t). \tag{5.21}$$

Hamilton's equation of motion gives the following set of equations,

$$\begin{aligned} \dot{\varphi} &= \frac{\partial \mathcal{H}}{\partial \mathcal{J}} = \frac{\Delta}{2\sqrt{J}}[\wp + \sqrt{\mathcal{J}}\nabla g(x)\cos(\varphi - t)]\nabla g(x)\cos(\varphi - t) \\ \dot{\mathcal{J}} &= -\frac{\partial \mathcal{H}}{\partial \varphi} = \sqrt{\mathcal{J}}[\wp + \sqrt{\mathcal{J}}\nabla g(x)\cos(\varphi - t)]\nabla g(x)\sin(\varphi - t) \end{aligned} \tag{5.22}$$

It is at this level that we will make our adiabatic arguments.

Time Averaged Hamiltonian

We solve this system of equations for φ and $\mathcal{J}$ by iteration. First, we formally solve Eq.(5.22) as integral equations,

$$\begin{aligned} \varphi &= \varphi(0) + \Delta\int_0^t dt' \frac{\wp}{2\sqrt{\mathcal{J}}}\nabla g(x)\cos(\varphi - t) + \frac{\Delta}{2}\int_0^t dt'(\nabla g(x))^2\cos^2(\varphi - t) \\ \mathcal{J} &= \mathcal{J}_0 + \Delta\int_0^t dt'\wp\sqrt{\mathcal{J}}\nabla g(x)\sin(\varphi - t) + \Delta\int_0^t dt'\mathcal{J}(\nabla g(x))^2\sin(2\varphi + t). \end{aligned} \tag{5.23}$$

Because of the high frequency of the oscillators we throw away all terms linear in $\sin(\phi - t)$ or $\cos\sin(\phi - t)$ since they integrate to 0 on average. We keep all terms

quadratic in $\sin(\phi - t)$ or $\cos\sin(\phi - t)$ because they average out to 1/2. To lowest order, the action

$$\mathcal{J} = \mathcal{J}_0 \to \dot{\mathcal{J}} \cong 0 \tag{5.24}$$

is an adiabatic invariant, and the phase evolves linearly in time,

$$\varphi \cong t. \tag{5.25}$$

(proportional $\omega_{sp}t$ in dimensional units). This gives us an effective Hamiltonian.

$$\mathcal{H}_{eff} = \frac{\Delta}{2}\wp^2 + \frac{1}{2}\left(\frac{\mathcal{J}(\nabla g(x))^2}{2} - g(x)^2\right). \tag{5.26}$$

We should be careful to note that this argument only works if the oscillator has non-zero initial conditions. Otherwise the solution for φ is divergent. If the oscillator does have some initial amplitude then the effective effective potential is,

$$U_{eff} = \frac{1}{2}\left(\frac{\mathcal{J}(\nabla g(x))^2}{2} - g(x)^2\right) \tag{5.27}$$

The term proportional to $g(x)^2$, is as we stated earlier, analogous to the polaron lowering energy, and is the remnant of our completing the square analysis. It is nothing more than the electrostatic image potential.

What's different here is the term proportional to $\mathcal{J}(\nabla g(x))^2$ in Eq, (5.27). Recall that it appeared as part of the extended momentum obtained when transforming into the displaced oscillator frame of reference (Eq.(5.18)); When we integrated out the oscillator coordinates, we gave the oscillator some initial amplitude, i.e.

$$Q_n = Q_n(0)\cos t + \int_0^t dt' \sin(t - t') g_n(x(t')) \tag{5.28}$$

If we examine the structure of the term $\frac{\mathcal{J}g(x)^2}{2}$ we see that its proportional to the derivative of $g(x)$, meaning that it is peaked in a different location than $\frac{g(x)^2}{2}$. It's

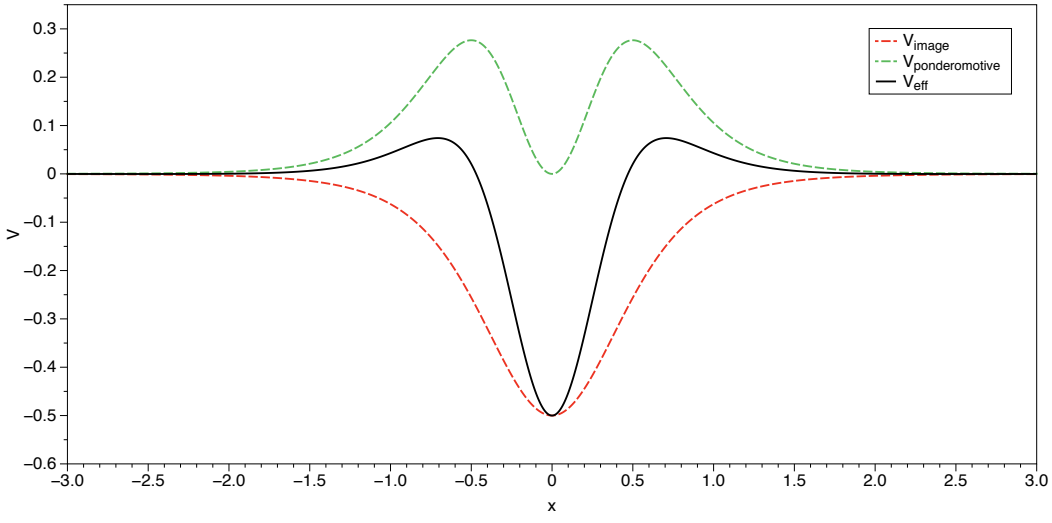

Figure 5.4: Effective potential seen by moving charge in adiabatic basis. The red curve is the electrostatic image potential. The green curve is the repulsive contribution and the black curve is the sum of the two for $\Delta = 2$ and the maximum of the influence function set to $g_{max} = 0.1$ and $\mathcal{J} = \frac{1}{2}$, with all quantities made dimensionless and normalized with respect to the SP energy $\hbar\omega_{sp}$.

also short range, and appears as a positive squared quantity, always making it a repulsive contribution to the effective potential. If the parameters of the system are tuned correctly, the particle can come in and reflect off the barrier as we saw in the far right region of Fig.5.3.

Clearly this analysis is very sensitive to the parameters of the system. The particle needs to be light enough to respond to weak external forces. The coupling must be weak enough to justify the perturbative nature of the calculation, the oscillator must have some initial energy and the electron may never pick up enough energy when compared to the energy of the oscillator. If any of these conditions are violated the adiabatic argument fails.

Our adiabatic Hamiltonian describes a free particle moving in an effective potential that consists of a long-range attractive potential and a short range repulsion. This system has many similarities to the case of a charge moving perpendicular to

a semi-infinite metal slab, and we expect to see similar results in this system. For that system we found that the particle would have a resonant frequency when in a bound state that was very near or larger than the SP frequency. Furthermore we saw that when the electron is traveling directly over the deepest part of the well, that it would pick up enough energy to violate the adiabatic approximation. Perhaps there are reasons due to the geometry of the system that this will not be the case here. One thing that's different about this system is the location of the repulsion. The charge-plane interaction had a repulsive term, but it was always located over the attractive part of the potential well. In contrast, in the case of the sphere, the structure of U_{eff} is such that the charge will hit a repulsive barrier before it reaches the bottom of the well. Let's calculate some physical values of the system. Recall that $\Delta = \frac{\hbar^2}{md^2}/(\hbar\omega_{sp})$ and $g(x) = \sqrt{\frac{e^2}{4\pi\varepsilon_0 a\hbar\omega_{sp}}}\left(\frac{a}{d}\right)^2 \frac{1}{(1+x^2)}$. If we take the distance between the SWNT and the surface of the sphere to be on the order of 1 nm, and the radius of the sphere to be about 5 nm, we can approximate the value of the coupling to be $g \sim \frac{1}{32}$ which is well withing the limits of perturbation theory. If we set $\mathcal{J} = \frac{1}{2}$ then the effective potential is,

$$U_{eff} = -\frac{1}{2}g^2(x) + \frac{\Delta}{8}[\nabla g(x)]^2 \tag{5.29}$$

We are also interested in maintaining as strong of a repulsion as possible while not violating our adiabatic arguments. Therefore, to have the repulsion compete with the attraction, we need the ratio of the attractive and repulsive terms of the effective potential to be on the order of 1. Making $\Delta \cong 1$ requires a very light mass. If we take the 1-D system to be a SWNT, we can take advantage of the light effective mass of SWNT charge carriers. Taking a value for $m^* \approx \frac{m_e}{100}$ [KM97], makes it possible to observe this effect without violating the adiabatic approximation. This seems like a narrow window to work in, but it might be possible if the materials are carefully chosen.

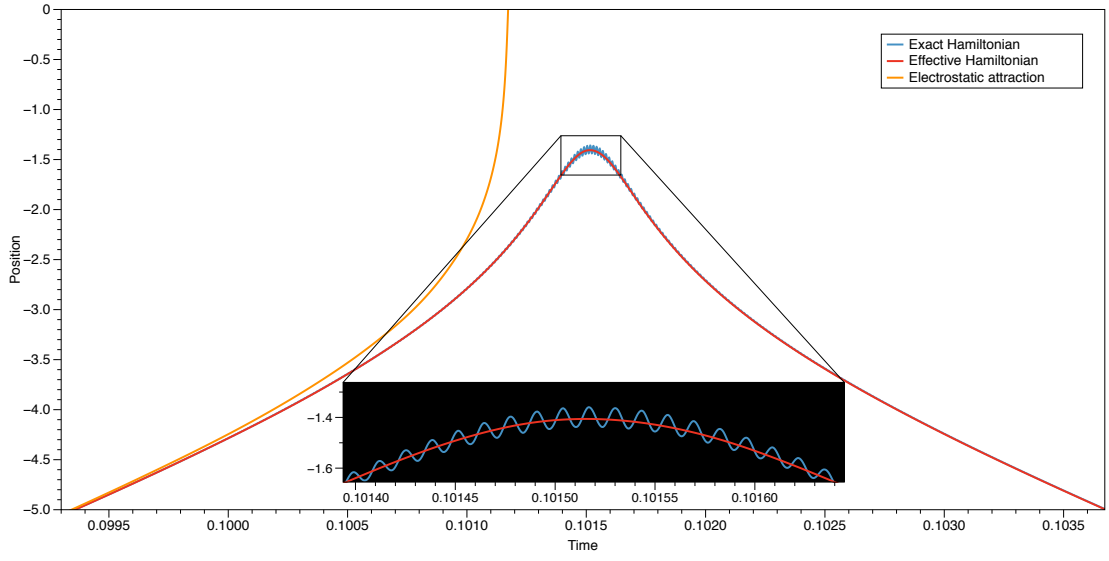

Figure 5.5: Position for exact, adiabatic and attractive potentials. The red curve is for simulations using the effective Hamiltonian, the blue curve is for simulations using the untransformed Hamiltonian, and the orange curve is for the effective Hamiltonian ignoring the repulsive contribution to U_{eff}.

Figure 5.5 shows a comparison of the results for the position of the moving charge for the parameters discussed above. The effective Hamiltonian does a remarkable job if we place ourselves in the correct parameter range. Even though we used the image force initially to derive the Hamiltonian, if we ignore the effect of the additional repulsive terms we lose any agreement at all. The key to all of this is the separation of time scales in which we separate the moving charge's quivering in response to the SP oscillation and its translational motion due to the long range image attraction. The dynamics of the particle can be further understood if we realize that the system under consideration is mathematically equivalent to the well-known ponderomotive interaction in gaseous state plasma physics.

Ponderomotive Force

The ponderomotive force is a well known effect in Plasma physics [BH57]. It is based on the same fundamental physics we've already described. The key to the effect is the balance between weak coupling, light mass and oscillator strength and the two time scales in the motion of the incoming charge. Consider the equation of motion for the charge when we give the SP oscillator some initial amplitude,

$$\ddot{x}(t) = \Delta\sqrt{\mathcal{J}}\nabla g(x)\cos t + \int_0^t dt' \sin(t-t')(\nabla g(x(t)))g(x(t')). \tag{5.30}$$

If we ignore the second term, we recover the traditional starting point for a particle interacting with a fast oscillating field [LL60]. The particle interacts with a fast oscillating SP field in the same way that it would with a laser field. A key feature to this is the spatial modulation of the time dependent term in Eq. (5.30). This is significant, because as an electron oscillates back and forth it samples the derivative of the modulating function $g(x)$. In a single oscillation cycle the electron is pushed back and forth over a space where the forces are not equal. This leads to the two types of motion we've been discussing, a fast quivering motion which is resonant with the frequency of the oscillating field and a one slow translational that is associated with the sum of the electrostatic potential and the electron's initial energy. What the adiabatic argument does is separate these two time scales and averages over the fast in resonance with the SP. A perturbation expansion is possible if it turns out that the fast motion has small amplitude. The averaged quivering motion shows up in the effective potential as a repulsive contribution.

It might be tempting to conclude that the particle steals some energy away from the oscillator, but in the adiabatic limit under consideration this is not the case. This is a self interaction mediated by the SP modes of the sphere. Figure 5.3 clearly shows that, in the limit of low incoming momentum, as the electron begins to quiver, the translational component of its overall motion also goes down. The quivering energy is taken from the net translational energy. This is possible even in the low energy

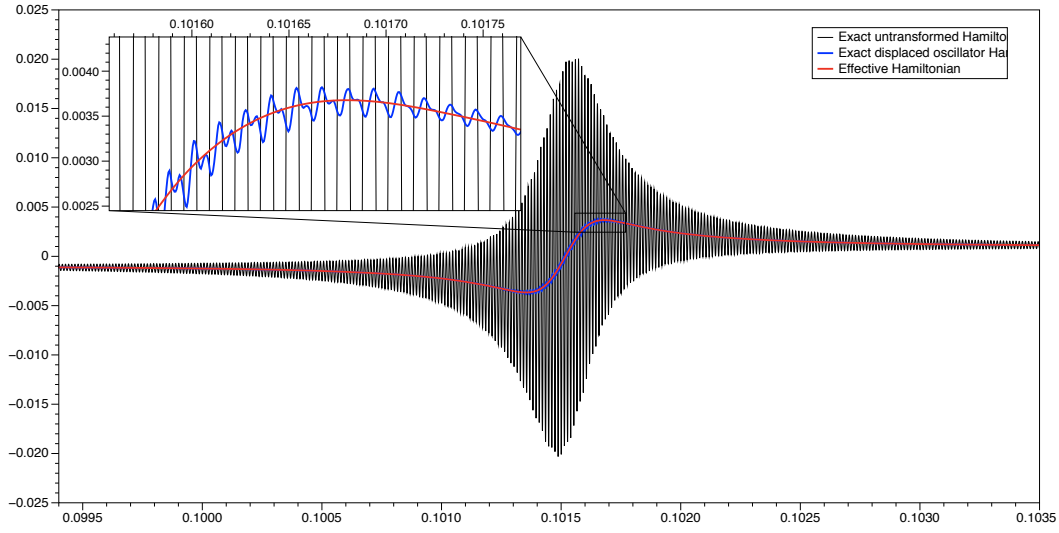

Figure 5.6: Momentum of the electron, the time axis is in dimensionless units of time normalized to ω_{sp}. The black curve is for the untransformed Hamiltonian. The blue curve is from the displaced oscillator Hamiltonian and the red curve is form the simulation results from the adiabatic Hamiltonian.

limit because of the small amplitude nature of the quivering. Once the electron has exhausted the reservoir of translational energy, it stops and then returns the energy to itself through the electron-SP interaction, and turns around. Figure 5.5 compares the approximate and exact solutions and shows the particle quivering back and forth as it approaches the position of the oscillator, slowing down, and going back the other way with the same energy it had on the way in. The adiabatic solution in the same figure shows the effective position of the electron cuts perfectly though the oscillations (see inset).

It should be noted that, in the case of the laser induced ponderomotive interaction, the electron couples weakly to the photon field, and only intense laser fields can induce the effect. In contrast, localized SPs are mostly concentrated in the near field, and therefore can couple more effectively. It is also interesting that the displaced oscillator transformation has played such an important role. If one looks at Fig. 5.6, one sees a comparison of the exact Hamiltonian, the exact displaced oscillator

Hamiltonian, and the effective Hamiltonian. The amplitude is vastly reduced in in the displaced oscillator picture even though the phase and frequency stay the same. The corresponding plots for position are not reproduced here because they are identical. It's only when you look at the rate of change of position with respect to time that this feature appears. This justifies our intuition in using the displaced oscillator transformation in the weak coupling limit.

Source of Oscillator Energy

We started this discussion with a charge coming in from infinity, but found that in order to carry out an adiabatic approximation it was necessary to have some initial energy in the SPs. We wonder if there might be a physical source for this energy that would not require that the plasmon be pumped. We're motivated by the idea that if the SP is treated quantum mechanically, it will have some zero point energy because it's an oscillator. Could the ground state energy be enough to make the repulsive term contribute? The old Borm-Sommerfeld-Wilson rule of qunatization [Wil15, Som16], when patched up to describe an oscillator, gives

$$\mathcal{J} = n + \frac{1}{2}. \tag{5.31}$$

and thus $\mathcal{J} = \frac{1}{2}$ is the action. For the moment let's accept the heuristic argument outlined above and discuss some of the other parameters in the model. It turns out that, for low effective mass particles, such as those found in SWNT, the parameter range seem to be on the edge of making it possible that a self induced ponderomotive repulsion could be observed in an experiment. This motivates us to rigorously prove the existence of a quantum mechanical counterpart to Eq, (5.26). The problem with the argument above is that action angle variables may not be quantized.

To resolve this we can follow one of two paths. We can reformulate our classical arguments when arriving to Eq. (5.26) in such a way avoid action angle variables

and remain in a Cartesian representation. This way would allow the canonical quantization [Dir47] of the generalized coordinates. Alternatively, we can quantize the exact unmolested Hamiltonian and find a set of unitary transformations that lead us to the same effective Hamiltonian or use perturbation theory to arrive to the same result. In the following section we do the latter.

5.4 Quantum Mechanical Hamiltonian

We begin again by writing our system in terms of raising and lowering operators. Accordingly, the Hamiltonian for this system is,

$$\hat{H}_0 = \frac{\Delta}{2}\hat{\wp}^2 + \left(\hat{b}^\dagger\hat{b} + \frac{1}{2}\right) - \lambda g(x)(\hat{b}^\dagger + \hat{b}) \tag{5.32}$$

where, $\hat{p} = -id/dx$. $\hat{b}^\dagger$ and $\hat{b}$ are the surface-plasmon creation and annihilation operators, respectively. They satisfy Bose commutation relations. The surface-plasmon frequency, ω_{sp}, is obtained using the metal Drude dielectric function, $\varepsilon(\omega) = \varepsilon_\infty - \omega_p^2/\omega(\omega + i\gamma)$, and λ is for book keeping since we will be using $g(x)$ as an expansion parameter.

5.5 Heisenberg's Equation of Motion Approach

One way of finding the effective Hamiltonian is through the use of Heisenberg's equation of motion. Writing the Hamiltonian in terms of raising and lowering operators gives,

$$\hat{H} = \frac{\hbar\Omega}{2}(\hat{\wp} - \nabla g(\hat{b}^\dagger - \hat{b}))^2 + \hbar\omega_{sp}(\hat{b}^\dagger\hat{b} + \frac{1}{2}) - \frac{\hbar\omega_{sp}}{2}g(x)^2, \tag{5.33}$$

which is the same starting Hamiltonian we have been using, but I have elected to leave in the factor of $\hbar\omega_{sp}$ and $\Omega = \Delta\hbar\omega_{sp}$, to better expose ω_{sp} in the calculation.

We start from equations of motion for $\hat{b}$,

$$\dot{\hat{b}} = -i(\omega_{sp} + \Omega(\nabla g)^2)\hat{b} + \frac{i\Omega(\nabla g)^2}{2}\hat{b}^\dagger + (-\frac{\Omega}{2}\nabla g(x)\hat{\wp} + i\Omega\nabla^2 g) \tag{5.34}$$

Let us define $\tilde{\Omega}(t) \equiv \omega_{sp} + \frac{\Omega}{2}(\nabla g)^2$ as the time dependent frequency and solve for b to zeroth order;

$$\hat{b}(t) = \hat{b}(0)e^{-i\int_0^t dt'\tilde{\Omega}(t')} = \hat{b}(0)e^{-i\varphi(t)}. \tag{5.35}$$

Here, the phase $\varphi(t) \equiv \int_0^t dt'\tilde{\Omega}(t')$ will deviate from linearity during the interaction, but return to linearity afterwards. But will only deviate a small amount as long as the incoming charge carrier never acquires much energy.

After inserting the zeroth order solution into the rhs of Eq. (5.34), we find the first order correction to be,

$$\begin{aligned}
\hat{b}(t) &= \hat{b}(0)e^{-i(\varphi(t)} + i\hbar\Omega\int_0^t dt'\hat{b}^\dagger(0)e^{i(\varphi(t')}e^{-i((\varphi(t)-\varphi(t'))} \\
&+ \int_0^t e^{i(\varphi(t')}e^{-i((\varphi(t)-\varphi(t'))}(-\hbar\Omega\nabla g(x)\hat{\wp} + i\Omega\nabla^2 g(x)) \\
&= \hat{b}(0)e^{-i(\varphi(t)} + i\hbar\Omega e^{-i\varphi(t)}\hat{b}^\dagger(0)\int_0^t dt' e^{2i\varphi(t')} \\
&+ e^{-i\varphi(t)}\int_0^t e^{i\varphi(t')}(-\frac{\hbar\Omega}{2}\nabla g(x)\hat{\wp} + i\hbar\Omega\nabla^2 g(x))
\end{aligned} \tag{5.36}$$

We throw out the last term because $e^{i\varphi(t')}$ will pass through many cycles during the time that $(-\frac{\Omega}{2}\nabla g(x)P + i\Omega\nabla^2 g(x))$ changes any appreciable manner. Writing $\varphi(t')$ explicitly, we have,

$$e^{i\varphi(t')} = e^{i\omega_{sp}t'}e^{i\int_0^{t'} dt''\frac{\Omega}{2}(\nabla g)^2} \tag{5.37}$$

which, when combined with the slow variables gives,

$$\int_0^t e^{i\omega_{sp}t'}[e^{i\int_0^{t'} dt''\frac{\Omega}{2}(\nabla g(x))^2}(-\Omega\nabla g(x)\hat{\wp}+2i\Omega\nabla^2 g(x))]dt' \cong 0. \tag{5.38}$$

We can also throw out the second term since $\int_0^t dt' e^{2i\varphi(t')} \cong 0$. Thus, to first order,

$$\begin{aligned}\hat{b}(t) &= \hat{b}(0)e^{-i\varphi(t)},\\ \hat{b}^\dagger(t) &= \hat{b}^\dagger(0)e^{+i\varphi(t)}.\end{aligned} \tag{5.39}$$

Let us now insert these solutions into the equations for $\dot{x}$ and $\dot{\hat{\wp}}$,

$$\hat{x}(t) = \hat{x}(0)+\hbar\Omega\int_0^t dt'\hat{\wp}(t') \tag{5.40}$$

$$- \quad i\hbar\Omega\int_0^t dt'(\hat{b}^\dagger(0)e^{i\varphi(t')}-\hat{b}(0)e^{-i\varphi(t')})\nabla g(x(t'))$$

$$\begin{aligned}\hat{\wp}(t) &= \hat{\wp}(0)+i\hbar\Omega\int_0^t dt'\hat{\wp}(t')\nabla^2 g(x(t'))(\hat{b}^\dagger(0)e^{i\varphi(t')}-\hat{b}(0)e^{-i\varphi(t')}) \\ &- i\hbar\Omega\int_0^t dt'(\hat{b}^\dagger(0)e^{i\varphi(t')}-\hat{b}(0)e^{-i\varphi(t')})(\nabla g(x(t')))^2\nabla g(x(t')) \\ &- 2\hbar\Omega\int_0^t dt'\nabla(\nabla^2 g(x(t')))(\hat{b}^\dagger(0)e^{i\varphi(t')}-\hat{b}(0)e^{-i\varphi(t')}) \\ &+\hbar\omega_{sp}\int_0^t \nabla(g(x(t'))^2\end{aligned} \tag{5.41}$$

We again throw away all fast oscillating terms, leaving us with,

$$\begin{aligned}\dot{\hat{\wp}} &\cong \frac{1}{2}\hbar\Omega\nabla(\nabla g(x))^2\left(\hat{b}^\dagger(0)\hat{b}(0)+\frac{1}{2}\right)+\hbar\omega_{sp}\nabla g(x)^2 \\ &= \frac{1}{2}\hbar\Omega\nabla(\nabla g(x))^2(\hat{n}+\frac{1}{2})+\hbar\omega_{sp}\nabla g(x)^2\end{aligned} \tag{5.42}$$

where $\hat{n}$ is the occupation number of the quantum SP oscillator. Choosing the ground state, we have,

$$\begin{aligned} \dot{\hat{\wp}} &= -\nabla\left[\frac{\Delta}{2}(\nabla g(x)))^2 - g(x)^2\right], \\ \dot{\hat{x}} &= \Delta\hat{\wp}, \end{aligned} \tag{5.43}$$

in dimensionless form. The effective Hamiltonian that gives this set of equations is,

$$\hat{H}_{eff} = \frac{\Delta}{2}\hat{\wp}^2 + \frac{1}{2}\left[\frac{(\nabla g(x))^2}{4} - g(x)^2\right]. \tag{5.44}$$

This method works as long as we don't go past first order, where higher order corrections begin to produce secular terms and make the expansion invalid. We simply have to let our classical intuition guide us and assume that all the secular terms produced will sum to some oscillatory function that does not blow up at long times.

Polaron Transformation and Perturbation Expansion

A different way to obtain the Hamiltonian above is to use the polaron transformation directly and see what the ground state Hamiltonian looks like. The Hamiltonian in the polaron picture is,

$$\hat{H} = \frac{\Delta}{2}\left(\hat{\wp} + \nabla g(x)\hat{P}\right)^2 + \frac{1}{2}\left(\hat{P}^2 + \hat{Q}^2\right) - \frac{1}{2}g(x)^2 \tag{5.45}$$

which, when expanded gives,

$$\hat{H} = \frac{\Delta}{2}\hat{\wp}^2 + \frac{\Delta}{2}(g(x)\hat{P})^2) + \frac{(\hat{\wp}\nabla g(x) + \nabla g(x)\hat{\wp})\hat{P}}{2} + \frac{1}{2}\left(\hat{P}^2 + \hat{Q}^2\right) - \frac{1}{2}g(x)^2. \tag{5.46}$$

Let us separate this into two parts,

$$\hat{H}_0 = \frac{\Delta}{2}\wp^2 + \frac{1}{2}\left(\hat{P}^2 + \hat{Q}^2\right); \tag{5.47}$$

$$\hat{H}_1 = \frac{\Delta}{2}\nabla g(x)^2\hat{P}^2 + \Delta\hat{\wp}\nabla g(x)\hat{P} - \frac{1}{2}g(x)^2. \tag{5.48}$$

Let us now perform Schrödinger perturbation theory using $\hat{H}_1$ as the perturbing Hamiltonian on the states of H_0, which are products $|n\rangle\,|k\rangle$. The term in Eq. (5.47) linear in $\hat{P}$ does not contribute to the ground state energy. Thus, the ground state energy is perturbed by,

$$E^{(1)}_{0,k} = \int_{-\infty}^{\infty} dx\ [-\frac{1}{2}g(x)^2 + \frac{\Delta}{8}\ g'(x)^2]\psi^*\psi. \tag{5.49}$$

This is compatible with a Hamiltonian of the form,

$$\hat{H}_{gs} = \frac{\Delta}{2}\hat{\wp}^2 + \frac{1}{2}\left(\frac{\Delta}{4}\nabla g(x)^2 - g(x)^2\right) \tag{5.50}$$

Classical Frohlich "Trick"

We have given a number of arguments as to why one should expect a quantum mechanical Hamiltonian to exist of the form analogous to Eq. (5.26). Another method is to attempt to derive H_{eff} while remaining in Cartesian coordinate space. To begin we again consider the analogy drawn between the electron-SP and polaron Hamiltonians. We are inspired Frölich's work on the electron-lattice Hamiltonian [Frö54]. What Frölich realized was that perturbation theory gave no contribution to the ground state wave function when considering the electron-lattice interaction. This was due to the linear form of the coupling in the interaction Hamiltonian between the electron and the lattice displacement coordinate $\hat{Q}_{lattice}$, leaving all corrections to be of second order or higher. Due to the difficulty of the problem he proposed to find a transformation that would transform to a coordinate frame which removed all terms linear in the $\hat{Q}_{lattice}$ or $\hat{P}_{lattice}$. The contributions to the ground state could then be calculated using first order perturbation theory. The way Frölich approached the problem was by searching for the unitary transformation that satisfied the following condition.

$$[\lambda\hat{S}, \hat{H}_0] = -\hat{H}_1(\lambda) \tag{5.51}$$

Here, $\hat{S}$ is the transformation generating function and λ is the expansion parameter. A review of this technique, and generalizations of it can be found in Wagner's [Wag86] book on unitary transformations. Unfortunately, accomplishing this solely through unitary transformations has proven to be difficult. Instead we develop a classical analogue to this approach while remaining in Cartesian coordinate space. Instead of searching for a unitary operator S that satisfies the Frölich condition Eq. (5.51), we search for a generating function F,

$$\lambda\{F, H_0\} = -H_1(\lambda). \tag{5.52}$$

We don't know the exact form of the generating function F, but we do know that any generating function that does satisfy Eq. (5.52) must be composed of old and new variables. Condition Eq. (5.52) is the same as Eq. (5.51) except that the commutation brackets have been replaced with Poisson brackets. We can show this to be true by first writing the generating function as a function of new and old variables,

$$F = f_0 + \lambda f(\tilde{\wp}, x, \tilde{P}, Q) \tag{5.53}$$

Let us write down the formal relations between old and new variables,

$$P = \tilde{P} - \lambda\frac{\partial f}{\partial Q} \tag{5.54}$$

$$\tilde{Q} = Q - \lambda\frac{\partial f}{\partial \tilde{Q}} \tag{5.55}$$

$$\wp = \tilde{\wp} - \lambda\frac{\partial f}{\partial x} \tag{5.56}$$

$$\tilde{x} = x - \lambda\frac{\partial f}{\partial \tilde{\wp}}. \tag{5.57}$$

Plugging these back into the Hamiltonian and collecting all terms of order λ and setting this to zero, we arrive at the equation,

$$\lambda\left(\Delta\tilde{\wp}\frac{\partial f}{\partial \tilde{x}} - \tilde{P}\frac{\partial f}{\partial \tilde{Q}} + \tilde{Q}\frac{\partial f}{\partial \tilde{P}} + \Delta\tilde{\wp}\nabla g(\tilde{x})\tilde{P}\right) = 0. \tag{5.58}$$

This is exactly the classical Fröhlich condition Eq. (5.52).

Equation (5.58) can be solved by the method of characteristics. The solution is,

$$f(s) = f(s=0) + \tilde{P}\int_0^{\tilde{x}} dx' cos\left(\frac{(\tilde{x}-\tilde{x}')}{\Delta_{\wp}}\right)\nabla g(\tilde{x}') + \tilde{Q}\int_0^{\tilde{x}} dx' sin\left(\frac{(\tilde{x}-\tilde{x}')}{\Delta_{\wp}}\right)\nabla g(\tilde{x}'). \tag{5.59}$$

For the limit of small $\wp$, the integral in Eq. (5.59), can be approximated by a stationary phase argument. Here we see that the particle must must have low momentum in order to justify the stationary phase argument, as this is what makes the sine and cosine oscillate wildly. In this form we explicitly see the necessity for low momentum in order to insure the validity of any adiabatic argument.

After approximating the integrals, the generating function has the form,

$$f(s) = f(s=0) + \tilde{\wp}\tilde{P}\nabla g(\tilde{x}=0)\ sin\left(\frac{\tilde{x}}{\Delta_{\wp}}\right) + \tilde{\wp}\tilde{Q}\nabla g(\tilde{x}=0)\ cos\left(\frac{\tilde{x}}{\Delta_{\wp}}\right) + \Delta\tilde{Q}\nabla g(\tilde{x}). \tag{5.60}$$

Using this to find the new variables, and substituting into the old Hamiltonian gives us a new Hamiltonian of the form,

$$H_{eff} = \frac{\Delta}{2}\wp^2\left(1+\lambda^2 h(x,Q)\right) + \frac{1}{2}(P^2+Q^2) + \lambda^2\frac{\Delta}{4}P^2(\nabla g(x))^2 - \frac{1}{2}\lambda^2 g(x)^2. \tag{5.61}$$

We observe that the effective Hamiltonian has been reduced to a system of order $g(x)^2$. A new term arises, taking the form of spatially dependent effective mass,

$$h(x) = \frac{\Delta^2}{2}g''(x) - \frac{\Delta^2}{2}g'''(x)\nabla g(x) - \frac{\Delta}{2}(\nabla g(x))^2. \tag{5.62}$$

We did not see this term in any other of our arguments, and if we include them when doing classical simulations, we find that they have no effect. Recall that we derived H_{eff} under the restriction of small $\wp$. Under these conditions it seems reasonable to assume that terms that scale like $\lambda^2\wp^2$ are effectively fourth order terms and can thus be ignored. To show this, we can perform one more transformation that scales

the coordinates x and $\wp$. Introducing another generating function,

$$F = -\wp \int_0^x \frac{dx'}{1+\lambda^2 h(x')}, \tag{5.63}$$

gives new variables as follows:

$$\begin{aligned} \wp &= -\frac{\partial F}{\partial x} = \frac{\tilde{\wp}}{\sqrt{1+\lambda^2 h(x)}} && (5.64)\\ \tilde{x} &= -\frac{\partial F}{\partial \wp} = \frac{1}{\sqrt{1+\lambda^2 h(q)}} \cong \int_0^x dx'(1-\lambda^2 h(x)) && (5.65)\\ &= x - \frac{1}{2}\lambda^2 \int_0^q dx' h(x') \end{aligned}$$

Any function $f(x)$ can be expressed as an expansion,

$$f(x) \cong f(\tilde{x}) + f'(\tilde{x}) \cdot \frac{1}{2}\lambda^2 \int_0^{\tilde{x}} dx' h(x') + \cdots \tag{5.66}$$

So any function in the Hamiltonian already of order λ^2 can be ignored in subsequent transformations because the corrections will go as λ^4.

We now have an effective Hamiltonian that can be quantized,

$$\hat{H}_{eff} = \frac{\Delta}{2}\hat{\wp}^2 + \frac{1}{2}\left(\hat{P}^2 + \hat{Q}^2\right) + \frac{\Delta}{4}(\nabla g(x))^2)\hat{P}^2 - g(x)^2. \tag{5.67}$$

This Hamiltonian represents a free quasi particle dressed with SP states traveling under the influence of an effective potential. Written in terms of raising and lowering operators gives,

$$\hat{H}_{eff} = \frac{\Delta}{2}\hat{\wp}^2 + \frac{1}{2}\left(\frac{\left(\hat{b}^\dagger\hat{b} + \frac{1}{2}\right)(\nabla g(x))^2}{2} - g(x)^2\right), \tag{5.68}$$

which, in the ground state, gives,

$$\hat{H}_{gs} = \frac{\Delta}{2}\hat{\wp}^2 + \frac{1}{2}\left(\frac{(\nabla g(x))^2}{4} - g(x)^2\right). \tag{5.69}$$

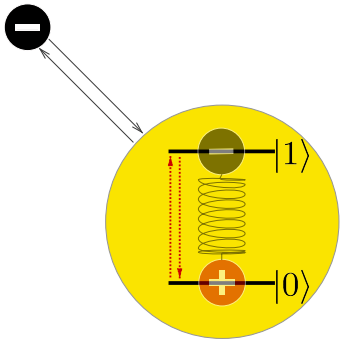

Figure 5.7: Schematic of quantum ponderomotive interaction. As the charge comes towards the sphere it excites virtual transitions between the ground and excited state of the SP. This mediates a self interaction.

This is the same as we found before, in Eq. (5.50), and also in Eq. (5.44).

Since we assuming a ground state solution, it turns out that the addition of more oscillators does not change the basic result. The effective Hamiltonian where both oscillators are included is,

$$\hat{H}_{eff} = \frac{\Delta}{2}\hat{\wp}^2 + \sum_i \frac{1}{2}\left(\hat{P}_n^2 + \hat{Q}_n^2\right) + \sum_i \frac{1}{2}\left(\frac{(\nabla g_n(x))^2}{4} - g_n(x)^2\right). \tag{5.70}$$

Classically we understood the effective potential as a sum of two terms, the electrostatic potential and the averaged fast quivering of the charge. Now the quantum mechanical description needs a new interpretation. $\hat{H}_{eff}$ is only valid in the adiabatic limit where the electron never gains enough energy to excite a real SP. However, energy need not be conserved on short time scales and the electron can induce virtual transitions of SPs. As the particle approaches the sphere it continuously excites virtual transitions which then mediates the self interaction of the electron, lowering the ground state of the SP modes. This is how the effect was understood by Sunjic and Lucas [ŠTL72], and also by Ritchie [Rit72], in their papers on the dynamical image force of a charge above a plane.

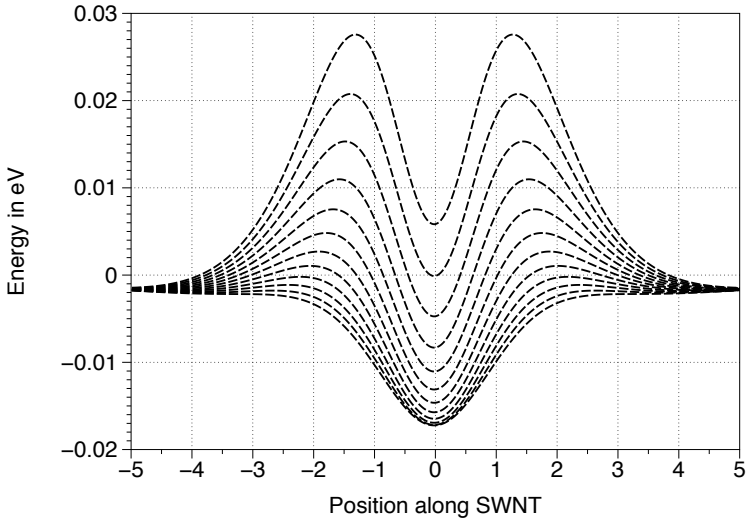

Figure 5.8: Effective potential seen by electron parametric in distance from the surface of MNP

5.6 Tunneling through the Effective Barrier

We are now free to explore the implications of $\hat{H}_{eff}$. Specifically we want to know how important the zero point repulsion is in a realistic system. One quantity that can be calculated is the tunneling amplitude of the electron. Tunneling experiments were used in the 1980's to test quantum dynamical image theory in planar geometries. The original experiment was proposed by Jonson [Jon80], and then quickly verified by Harstein [HWD82] at IBM labs. This motivates us to examine tunneling to see if our system exhibits any novel behavior due to the quantum corrections.

Imagine an experimental setup consisting of a SWNT and a MNP, in which the distance d between the SWNT and the MNP can be controlled. If the parameters are such that Eq. (5.69) correctly describes the system, then the potential seen by the electron as the distance is varied will dramatically change due to ponderomotive effects. Figure 5.8 shows the family of potentials for a range of values for $d-a$. Here, a is the radius of the MNP, which we have chosen to set to 5 nm, the effective mass

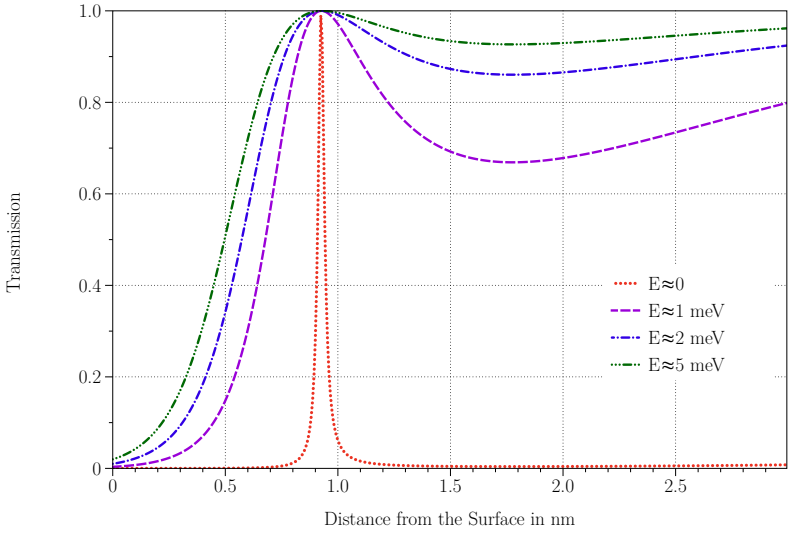

Figure 5.9: Transmission as a function of distance from surface of MNP.

of the electron in the SWNT is, $m^* = 1/100$, and we have assumed a silver MNP with a SP frequency of $\omega_{sp} \approx 3$ eV. Figure 5.9 shows the results of a transfer matrix calculation using the ground state Hamiltonian Eq. (5.69). It plots the transmission coefficient of the electron as a function of the distance between the SWNT and the MNP, and is parametric in initial energy. There appears, at first glance, to be a tunneling resonance at 1 nm from the surface of the MNP for very low energy electrons. However, the deBroglie wave length of the electron at these energies is too large to coincide with the width of the potential and the peak can not be explained as a tunneling resonance. Instead, due to the long deBroglie wave length of the electron, the effective potential behaves as if it were a δ-function potential.

By treating U_{eff} as a delta function we can formulate an effective transmission coefficient in the form,

$$T = |t|^2 = \frac{k^2}{k^2 + (\frac{m}{\hbar^2}\int_{-\infty}^{\infty} U_{eff}(x)dx)^2}. \tag{5.71}$$

The expression in Eq. (5.71) indicates that when the total area under the potential vanishes, the electron effectively sees no potential at all, leading to the illusion of

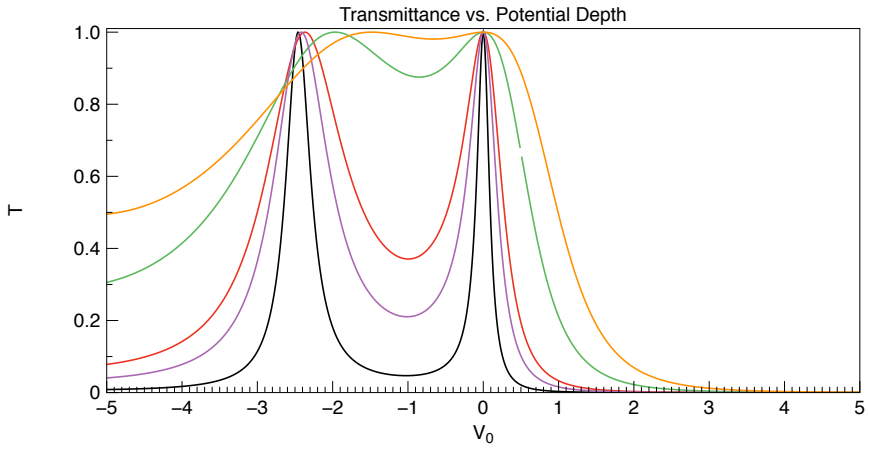

Figure 5.10: Transmission of an electron though a step potential with varying potential depth.

a resonant peak. As the initial energy of the particle increases, the potential looks less like a δ function and the effect is less pronounced. This is just the simple observation that, when the potential is zero, there is no potential to scatter from. This can be visualized through a potential well model. Figure 5.10 shows the result for a step potential problem where the depth of the well is allowed to vary from negative to positive values, as though mimicking the ponderomotive repulsion. When the potential is identically zero, we see the transmission go to unity, as we would expect. The similarities between Fig. 5.9 and Fig. 5.10 suggest that the same essential mechanism is at play. Figure 5.10 shows more peaks at lower negative energies because it has some features that our potential does not. Namely, as the well gets deeper, the electron catches tunneling resonances.

5.7 Conclusion

We have shown how to derive an adiabatic Hamiltonian for the case of a moving charge interacting with a MNP. These results have been justified through classical

and quantum mechanical arguments, and have been applied to a tunneling problem where we have shown the existence of a novel resonance. Though similar reflection effects were derived for planar interfaces [ŠTL72, ZRM89, RM72] we have contributed to the field by examining the effect in materials and geometry relevant to the current research goals of the nanoscience community. Most importantly, we have provided a new and unknown interpretation of the result by framing the electron-SP interaction in the language of ponderomotive forces.

Chapter 6

Exciton Transport in Carbon Nanotubes

6.1 Introduction

The excitation of SP resonances at a metal-dielectric interface results in a strong local electric field in close (i.e., nanoscale) proximity to the interface. This in turn can affect the optical properties of nearby quantum emitters such as fluorescent molecules or semiconductors nanostructure [NH12, Sto11]. Basic quantities, such as emission rates, Raman scattering and absorption cross-sections can be enhanced [NH12, CPS78, GN80]. On the other hand, energy transfer from a quantum emitter to a metal nanoparticle and the subsequent Ohmic losses also occur as a result of the same near field coupling. The balance between the enhancement of the optical properties and the dissipation of energy has a complex dependence on the distance between the quantum emitter and metal interface as well as nanoparticle geometry [NH12, Sto11].

Recent advances in nanoscale fabrication allow for precise control over the ge-

ometry of MNPs, allowing one to tune their SP response across the visible and near-IR spectrum, and to control the associated SP line shapes [PRHN03, LPK06, LBU$^+$08, Ach10] . This allows for the modification of desired properties, e.g., enhancing Förster energy transfer between molecules and/or semiconductor QDs as discussed in Chapter 3 [GLK07, DRKS08, ZLS$^+$13, PS11]. Single and multi-exciton emission rates and emitted photon statistics can be manipulated in composite semiconductor QD and metal nano-structures for applications such as single-photon or entangled photon-pair sources [MNMI09, PGC$^+$13]. Single-photon emission can also be controlled via the coupling of localized quantum emitters to SPP modes in metal nanowire [KGB$^+$09]. Interactions within *assemblies* of quantum emitters, as mediated by SPP modes, can lead to cooperative optical behavior such as the plasmonic Dicke effect [PS09, PS10].

The strong exciton-SP interaction regime, as characterized by the interaction frequency exceeding the dissipation rate, can be achieved in specially chosen geometries of metal nano-structures and quantum emitters. In these systems, strong coupling leads to the formation of mixed exciton-SP states referred to as plexitons, and the appearance of a significant exciton energy Rabi shift [SKB$^+$06, GVMD09, GVMD10, MAN11]. Furthermore, the interference between exciton and SP energy exchange pathways results in Fano resonances [ZGB06, AB08, RDSF$^+$10]. Strong coupling between a single quantum emitter and a SPP confine to a narrow metal nanowire results in the excitation of quantized SP modes [AMY$^+$07, dLSC$^+$12, FTS$^+$07] and allows for control of SP transmission, suggesting a potential application in single-photon transistors [CSHL05]. A nanoscale plasmon resonator has been realized by combining a metal nanowire with a distributed Bragg grating [dLSC$^+$12]. These studies, primarily focused on the interactions of localized quantum emitters with SP modes, constitute a new field of quantum plasmonics [TMÖ$^+$13].

On the other hand, localized SP modes can interact with delocalized excitons in one-dimensional semiconductor nanostractures, particularly affecting their long-

range transport and emission properties. In one example, the effect of exciton-SP energy transfer on the exciton emission wave lengths has been investigated in a semiconductor nanowire decorated with metal nanoparticles [GLK07]. It has been shown that energy transfer to the metal prevents excitons from finding local minima and enhances the resulting blue shifted emission. Another class of one-dimensional nanostructures exhibiting long-range exciton transport are SWNTs. Their optical and transport properties look very promising for potential applications in optoelectronic and photovoltaic devices [ABC$^+$13].

Exciton motion in SWNTs has diffusion-limited transport features that are likely caused by coupling to extensive environmental fluctuations [CDW$^+$12]. Measurements of exciton transport in SWNTs have been carried out using optical microscopy techniques[NH12, CDW$^+$12] including near-field enhancement caused by the interactions of excitons with SP modes in a metal tip (MT) [GBQ$^+$09]. These techniques are sensitive to the emitting dipole orientation via the angular distribution of emitted radiation in the far-field [NH12]. Further application of optical microscopy techniques to study MT effects on SWNT excitons has revealed a nanoantenna effect in which there is fast near-field energy transfer to the tip that is followed by efficient SP radiative emission with a specific directional redistribution [BHG$^+$10]. To this point, these observations have been described in the context of a simple exciton random walk model with enhanced excitation and radiation rates. However, a complete understanding of the effect of the localized SP resonances on transport properties of excitons in SWNTs requires a theoretical approach capable of treating exciton transport, near-field exciton-SP interactions, dissipation processes, and radiation properties, on the same footing.

In this Chapter, we report on the systematic investigation of a localized SP mode on exciton transport and emission properties in a SWNT. The exciton, SP, and photon degrees of freedom are accounted for using a unified quantum mechanical approach. Parameters associated with the exciton-SP interactions are determined

from independent numerical calculations of the quasi-static SP response. These parameters are subsequently used in simulations of coupled exciton transport that are used to calculate a combined exciton/SP radiation distribution pattern. This Chapter is organized as follows. Our theoretical model is introduced in Sec. 6.2. In Sec. 6.3 we apply the model to a (6,5) SWNT in proximity to a MT, and present the results of numerical simulations. Concluding remarks are given in Sec. 6.4. This work presented in this Chapter has been submitted for publication at Journal of Chemical Physics B [RCDP14].

6.2 Theoretical Model

In this section we derive a set of coupled equations describing the evolution of the exciton and MT-SP populations and their coherences following a reduced density matrix approach [KKK84, Muk99, VW06] to account for the coherent exciton-SP coupling and the effect of the environment. Integration of coherences results in a set of the rate equations for exciton and SP populations. We express the exciton-SP population transfer rates in terms of the SP dyadic Green function, introduced in Chapter 2, associated with the near-field interactions of the SP mode and excitons. This quantity can be determined from numerical simulations of the MT-SP response. Ultimately the overall emission cross-section can be calculated in terms of the exciton and SP populations and coherences.

6.2.1 Transport Model

Consider an exciton migrating in a SWNT that is aligned with the x-axis. The exciton excites SP modes in a MT a distance, d, below the center of the SWNT, as shown in Fig. 6.1. For computational purposes, the SWNT has been partitioned into $N+1$ sites, each labeled by a site-index n, with site $n=0$ locating the center.

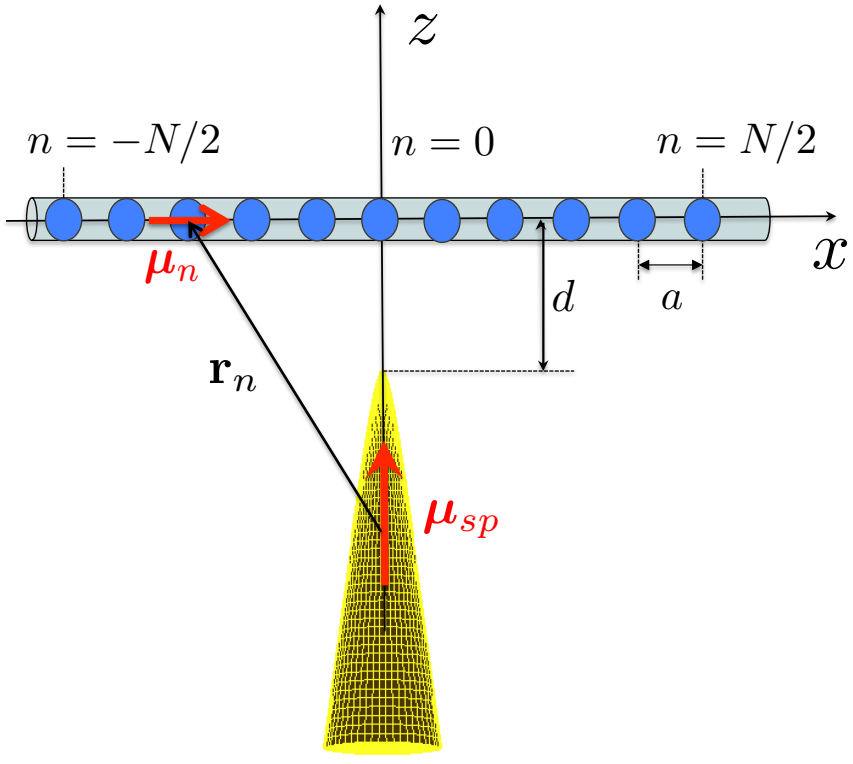

Figure 6.1: Partitioning of the exciton delocalization length along SWNT into N sites separated by distance a. Transition dipole, μ_n, is assigned to each site and oriented along the SWNT axis, i.e., the x-axis. The MT is placed on the distance d below the SWNT with the symmetry axis coinciding with the z-axis. We consider the SP mode associated with the transition dipole, μ_{sp}, oriented along the MT symmetry axis.

To model the exciton-SP interaction, we assign a transition dipole, $\boldsymbol{\mu}_n = \boldsymbol{e}_x \mu_n$, to each site, with direction defined by the unit vector $\boldsymbol{e}_x$. The SP dipole, $\boldsymbol{\mu}_{sp} = \boldsymbol{e}_z \mu_{sp}$, has a perpendicular orientation in a direction defined by the unit vector $\boldsymbol{e}_z$. Vector connecting the centers of the $\boldsymbol{\mu}_{sp}$ and $\boldsymbol{\mu}_n$ is denoted by $\boldsymbol{r}_n$.

We will assume that the SP energy $\hbar\omega_{sp}$ associated with the chosen polarization is tuned to be close to the on-site exciton energies $\hbar\omega_n$, and yet well-separated from the energies of other SP modes. The quasi-electrostatic exciton-SP interaction will be characterized by the energy $\hbar g_n$. As discussed in section 6.2.2, the coupling constant g_n provides frequency of a *single-quantum* exchange between site-n and the SP mode

due to transitions characterized by the associated dipole matrix elements $\boldsymbol{\mu}_n$ and $\boldsymbol{\mu}_{sp}$. By adopting a rotating-wave approximation for the coupling term, the system Hamiltonian maps on a spinless Anderson-Fano Hamiltonian [Mah00].

$$\hat{H}_{AF} = \sum_n \hbar\omega_n \hat{b}_n^\dagger \hat{b}_n + \hbar\omega_{sp}\hat{a}_{sp}^\dagger \hat{a}_{sp} + \sum_n \hbar\left(g_n \hat{b}_n^\dagger \hat{a}_{sp} + g_n^* \hat{a}_{sp}^\dagger \hat{b}_n\right), \tag{6.1}$$

where $\hat{b}_n^\dagger$ and $\hat{b}_n$ ($\hat{a}_{sp}^\dagger$ and $\hat{a}_{sp}$) are creation and annihilation operators of the exciton on site n (localized SP state), respectively. Considering low exciton population, both exciton and SP operators obey Bose commutation relations.

To account for the effect of the environment, we introduce the reduced density operator, $\hat{\rho}_{AF}$, which satisfies the Liouville equation in the following form

$$\dot{\hat{\rho}}_{AF} = \frac{1}{i\hbar}[\hat{H}_{AF}, \hat{\rho}_{AF}] + \hat{\mathcal{R}}_1\hat{\rho}_{AF} + \hat{\mathcal{R}}_2\hat{\rho}_{AF} + \dot{\hat{\rho}}_{ex}. \tag{6.2}$$

The first term on the right hand side describes coherent dynamics corresponding to the Anderson-Fano Hamiltonian (Eq. (6.1)), and the last term described the exciton population increase due to optical pumping. The second and the third terms are relaxation terms are accounted for in a general Lindblad form

$$\begin{aligned}\hat{\mathcal{R}}_1\hat{\rho}_{AF} &= \sum_n \frac{\gamma_n}{2}\left(2\hat{b}_n\hat{\rho}_{AF}\hat{b}_n^\dagger - \hat{b}_n^\dagger\hat{b}_n\hat{\rho}_{AF} - \hat{\rho}_{AF}\hat{b}_n^\dagger\hat{b}_n\right) \qquad (6.3)\\ &+ \frac{\gamma_{sp}}{2}\left(2\hat{a}_{sp}\hat{\rho}_{AF}\hat{a}_{sp}^\dagger - \hat{a}_{sp}^\dagger\hat{a}_{sp}\hat{\rho}_{AF} - \hat{\rho}_{AF}\hat{a}_{sp}^\dagger\hat{a}_{sp}\right)\\ \hat{\mathcal{R}}_2\hat{\rho}_{AF} &= \sum_{nm}\frac{w_{nm}}{2}\left(2\hat{b}_n^\dagger\hat{b}_m\hat{\rho}_{AF}\hat{b}_m^\dagger\hat{b}_n - \hat{b}_m^\dagger\hat{b}_n\hat{b}_n^\dagger\hat{b}_m\hat{\rho}_{AF} - \hat{\rho}_{AF}\hat{b}_m^\dagger\hat{b}_n\hat{b}_n^\dagger\hat{b}_m\right). \qquad (6.4)\end{aligned}$$

Eq. (6.3) accounts for the exciton and SP population decay processes with rates γ_n and γ_{sp} respectively. These include both non-radiative and radiative channels. Eq. (6.4) describes exciton scattering processes with the rates w_{nm} giving rise to dephasing and diffusion.

The complete set of reduced density operator matrix elements can be introduced as the following set of operator averages: the on-site exciton population is $N_n =$

$\mathrm{tr}\{\hat{b}_n^\dagger \hat{b}_n \hat{\rho}_{AF}\}$, the SP population is $N_{sp} = \mathrm{tr}\{\hat{a}_{sp}^\dagger \hat{a}_{sp} \hat{\rho}_{AF}\}$, the exciton spatial coherence between sites $n \neq m$ is $X_{nm} = \mathrm{tr}\{\hat{b}_n^\dagger \hat{b}_m \hat{\rho}_{AF}\}$, and the exciton-SP coherence is $Y_{n,sp} = \mathrm{tr}\{\hat{b}_n^\dagger \hat{a}_{sp} \hat{\rho}_{AF}\}$. We consider an experimentally realized situation in which only the excitons are optically excited but not the SP mode (e.g., the laser is tuned to an energy lying well above the SP resonance, and exciton population growth follows inter and/or intra-band relaxation). These process are accounted for by introducing an on-site exciton population gain with the rate $\mathrm{tr}\{\hat{b}_n^\dagger \hat{b}_n \dot{\hat{\rho}}_{ex}\} = I_n$.

For the density matrix elements introduced above, we obtain the following coupled equations of motion from Eq. (6.2):

$$\dot{N}_n(t) = -i\left(g_n Y_{n,sp} - g_n^* Y_{n,sp}^*\right) + D\frac{\partial^2 N_n}{\partial n^2} - \gamma_n N_n + I_n, \tag{6.5}$$

$$\dot{N}_{sp}(t) = i\sum_n \left(g_n Y_{n,sp} - g_n^* Y_{n,sp}^*\right) - \gamma_{sp} N_{sp}, \tag{6.6}$$

$$\dot{X}_{nm}(t) = i\tilde{\omega}_{nm} X_{nm} - i\left(g_m Y_{n,sp} - g_n^* Y_{m,sp}^*\right), \tag{6.7}$$

$$\dot{Y}_{n,sp}(t) = i\tilde{\omega}_{n,sp} Y_{n,sp} - i\sum_{m\neq n} g_m^* X_{nm} - i g_n^*(N_n - N_{sp}). \tag{6.8}$$

Eq. (6.5) contains a diffusion term in which the second derivative $\partial^2 N_n/\partial n^2 = (N_{n+1} - 2N_n + N_{n-1})$ is defined as the finite difference of the nearest neighbor populations. The diffusion term is the long-wavelength approximation to the master equation associated with the relaxation term (Eq. (6.4)) matrix element $\mathrm{tr}\{\hat{b}_n^\dagger \hat{b}_n \hat{\mathcal{R}}_2 \hat{\rho}_{AF}\}$ $= \sum_m (w_{nm} N_m - w_{mn} N_n)$. Assuming inversion and translational symmetry, $w_{nm} = w_{mn} \to w_{|m-n|}$, the diffusion rate $D = \sum_n w_n n^2$ is given by the weighted sum of exciton site-scattering rates from Eq. (6.4). The coherences (Eqs. (6.7) and (6.8)), X_{nm} and $Y_{n,sp}$ depend on the complex frequencies $\tilde{\omega}_{nm} = \omega_n - \omega_m + i(\gamma_n/2 + \gamma_m/2 + \tilde{\gamma}_{mn})$ and $\tilde{\omega}_{n,sp} = \omega_n - \omega_{sp} + i(\gamma_n/2 + \gamma_{sp}/2 + \tilde{\gamma}_n)$, respectively. Here, γ_n and γ_{sp} are the exciton and SP population decay rates defined in Eq. (6.3), and the dephasing rates are expressed in terms of the exciton scattering rates as follows $\tilde{\gamma}_n = \sum_m w_{mn}/2$ and $\tilde{\gamma}_{mn} = w_{mn} + w_{mm}/2 + w_{nn}/2$.

Typically, coherences approach their steady state values on the timescale faster

than the populations, and can be eliminated from the equations for the populations. The steady state solution for coupled Eqs. (6.7) and (6.8) can be found from a perturbation expansion in the small parameter $g_n/(\gamma_n/2 + \gamma_{sp}/2 + \tilde{\gamma}_n)$, resulting in the following second and third order expressions

$$\begin{aligned} X_{nm} &= \frac{1}{\tilde{\omega}_{nm}} \{(\boldsymbol{\mu}_m \cdot \mathbf{G}_{mn}(\tilde{\omega}_n) \cdot \boldsymbol{\mu}_n)(N_n - N_{sp}) \\ &- (\boldsymbol{\mu}_m \cdot \mathbf{G}_{mn}(\tilde{\omega}_n) \cdot \boldsymbol{\mu}_n)^*(N_m - N_{sp})\} \end{aligned} \tag{6.9}$$

$$\begin{aligned} Y_{n,sp} &= \sum_m \frac{|\boldsymbol{\mu}_m \cdot \mathbf{G}_{mn}(\tilde{\omega}_n) \cdot \boldsymbol{\mu}_n|^2}{g_n \tilde{\omega}_{nm}} (N_n - N_m) \\ &+ \frac{1}{g_n} (\boldsymbol{\mu}_n \cdot \mathbf{G}_{nn}(\tilde{\omega}_n) \cdot \boldsymbol{\mu}_n)(N_n - N_{sp}), \end{aligned} \tag{6.10}$$

respectively. Substitution of the coherences into Eqs. (6.5) and (6.6) leads to coupled rate equations for the exciton and SP populations:

$$\begin{aligned} \dot{N}_n(t) &= -W_{n,sp}\,(N_n - N_{sp}) \\ &- \sum_{m \neq n} W_{nm}\,(N_n - N_m) + D\frac{\partial^2 N_n}{\partial n^2} - \left(\gamma_n^{nr} + \gamma_n^{rd}\right) N_n + I_n, \end{aligned} \tag{6.11}$$

$$\begin{aligned} \dot{N}_{sp}(t) &= \sum_n W_{n,sp}\,(N_n - N_{sp}) + \sum_n \sum_{m \neq n} W_{nm}\,(N_n - N_m) \\ &- (\gamma_{sp}^{nr} + \gamma_{sp}^{rd}) N_{sp}, \end{aligned} \tag{6.12}$$

valid in the *weak* coupling regime and accounting for both energy transfer to SP and SP-assisted exciton site energy transfer on the same footing. Specifically, the exciton-SP population transfer rate is

$$W_{n,sp} = \frac{2}{\hbar} \mathrm{Im}\left(\boldsymbol{\mu}_n \cdot \mathbf{G}_{nn}(\tilde{\omega}_n) \cdot \boldsymbol{\mu}_n\right), \tag{6.13}$$

with $\tilde{\omega}_n = \omega_n + i(\gamma_n/2 + \tilde{\gamma}_n)$, and the SP-assisted exciton site transfer rate is

$$W_{nm} = \frac{2\gamma_{nm}}{\hbar^2(\omega_{nm}^2 + \gamma_{nm}^2)} \left|\boldsymbol{\mu}_n \cdot \mathbf{G}_{nm}(\tilde{\omega}_n) \cdot \boldsymbol{\mu}_m\right|^2, \tag{6.14}$$

with $\omega_{nm} = \omega_n - \omega_m$ and $\gamma_{nm} = \gamma_n/2 + \gamma_m/2 + \tilde{\gamma}_{mn}$. These expressions, along with Eqs. (6.9) and (6.10) are written in terms of the dyadic Green function $\mathbf{G}_{nm}(\omega)$ for the SP mode, as described in section 6.2.2.

6.2.2 Exciton-SP interaction and dyadic Green function.

The system we want to consider and model is of a SWNT and a metal tip (MT). In order to model this system we do not specify the geometry of the nanoparticle but instead declare the SP to be a quantum oscillator with an effective transition dipole moment. Alternative cavity QED quantization approach requires knowledge of MNT geometry [WS10]. To identify the parameters of the SP quantum oscillator, we exploit the connection between parameters of the Hamiltonian (Eq. (6.1)) and the classical dyadic Green function.

Consider quantum mechanical oscillator associated with a SP mode characterized by a transition dipole operator $\hat{\boldsymbol{\mu}}_{sp} = \boldsymbol{\mu}_{sp}(\hat{a}_{sp} + \hat{a}^{\dagger}_{sp})$ coupled to a local electric field $\hat{\mathbf{E}}_{loc}$. The associated Hamiltonian is,

$$\hat{H}_{sp} = \hbar\omega_{sp}\hat{a}^{\dagger}_{sp}\hat{a}_{sp} - \hat{\boldsymbol{\mu}}_{sp} \cdot \hat{\mathbf{E}}_{loc}. \tag{6.15}$$

Here, the local field is induced by the exciton transition dipole leading to the following relation;

$$\hat{\mathbf{E}}_{loc} = \sum_n \mathbf{T_n} \cdot \boldsymbol{\mu}_n(\hat{b}^{\dagger}_n + \hat{b}_n), \tag{6.16}$$

containing a tensor $\mathbf{T_n}$ which asymptotically corresponds to the longitudinal electric field component of a dipole

$$\mathbf{T_n} \sim \frac{3\mathbf{nn} - \mathbf{I}}{4\pi\varepsilon_0\varepsilon r_n^3}. \tag{6.17}$$

In Eq. (6.17), $\mathbf{n} = \boldsymbol{r}_n/r_n$ (Fig. 6.1) and $\mathbf{I}$ is the 3×3 identity matrix. Substitution of Eq. (6.16) in Eq. (6.15) in the rotating wave approximation gives second and the third terms in the Hamiltonian $\hat{H}_{AF}$ (Eq. (6.1)) with the exciton-SP interaction energy:

$$\hbar g_n = \boldsymbol{\mu}_{sp} \cdot \mathbf{T_n} \cdot \boldsymbol{\mu}_n. \tag{6.18}$$

To find the relationship between the dyadic Green function and the exciton-SP interaction rate, g_n, we solve the frequency-domain equations of motion for the Hamiltonian system given by Eqs. (6.15) and (6.16), adding the SP nonradiative relaxation rate $\gamma_{sp}^{nr}/2$ via the second term of Eq. (6.3). The outcome is an expression for the local contribution to the SP dipole *induced* by the exciton dipole at site m,

$$\boldsymbol{\mu}_{sp}(\omega_m) = \alpha(\omega_m)\boldsymbol{e}_z(\boldsymbol{e}_z \cdot \mathbf{T_m} \cdot \boldsymbol{\mu}_m). \tag{6.19}$$

In Eq. (6.19), $\boldsymbol{e}_z$ is the polarization direction of the SP mode (Fig. 6.1) with polarizability

$$\alpha_{sp}(\omega) = \frac{\mu_{sp}^2}{\hbar(\omega - \omega_{sp} + i\gamma_{sp}/2)}. \tag{6.20}$$

The electric field at exciton site n due to the induced SP dipole is $\mathbf{E}_n = \mathbf{T_n} \cdot \boldsymbol{\mu}_{sp}$, so that formally,

$$\mathbf{E}_n = \alpha(\omega_m)\,(\mathbf{T_n} \cdot \boldsymbol{e}_z)\,(\boldsymbol{e}_z \cdot \mathbf{T_m} \cdot \boldsymbol{\mu}_m).$$

Alternatively, one could use the dyadic Green function to express the same field,

$$\mathbf{E}_n(\omega_m) = \mathbf{G}_{mn}(\omega_m) \cdot \boldsymbol{\mu}_m(\omega_m).$$

Comparison of the two expressions above shows that the dyadic Green function may be expressed in the form,

$$\mathbf{G}_{mn}(\omega) = \alpha_{sp}(\omega)\,(\boldsymbol{e}_m \cdot \mathbf{T_m} \cdot \boldsymbol{e}_z)\,(\boldsymbol{e}_z \cdot \mathbf{T_n} \cdot \boldsymbol{e}_n)\,. \tag{6.21}$$

The substitution of Eqs. (6.18) and (6.20) into Eq. (6.21) results in,

$$\boldsymbol{\mu}_n \cdot \mathbf{G}_{nm}(\omega) \cdot \boldsymbol{\mu}_m = \frac{\hbar g_n g_m^*}{\omega - \tilde{\omega}_{sp}}, \tag{6.22}$$

which is extensively used in Sec. 6.2.

Typically, the dyadic Green function is introduced as the solution to Maxwell's equations [NH12, VW06]. In our case, however, it is only the near field interactions defined by the Poisson equations that are responsible for the exciton-SP coupling and contribute to the Green function given by Eq. (6.21). We determine $\mathbf{G}_{mn}(\omega)$ numerically using the Boundary Element Method implemented in MNPBEM13 code [dAH02, HT12]. Values of the SP frequency ω_{sp} and the nonradiative decay rate γ_{sp} are extracted from the calculated SP absorption spectrum (excited by a z-polarized plane wave) as this is proportional to the imaginary part of $\mathbf{G}_{mn}(\omega)$. The SP transition dipole μ_{sp} can be determined analytically from the dyadic Green functions found in Eqs. (6.17), (6.20), and (6.21). In this calculation, a SWNT axis is separated from the MT by distance $d > 100$ nm to insure that the asymptotic Eq. (6.17) holds. For distances $d < 100$ nm, Eq. (6.17) breaks down and the absolute values of the coupling rates g_n must be determined from direct numerical simulations of $\mathrm{Im}(\boldsymbol{\mu}_n \cdot \mathbf{G}_{nn}(\omega_n) \cdot \boldsymbol{\mu}_n)$ with the help of Eq. (6.22). The sign of g_n is recovered by examining the derivative of the coupling rate, dg_n/dx.

6.2.3 Radiation Emission Pattern

To include spontaneous emission processes leading to PL, we extend our system Hamiltonian (Eq. (6.1)) by adding a term describing a quantized radiation mode interacting with material dipoles [Lou00, VW06]

$$\begin{aligned} \hat{H}_{RD} &= \sum_{\boldsymbol{q},\lambda=1,2} \hbar v|\boldsymbol{q}| \hat{a}^\dagger_{\boldsymbol{q}\lambda} \hat{a}_{\boldsymbol{q}\lambda} \\ &+ \hat{\boldsymbol{\mu}}_n \cdot \left(\hat{\boldsymbol{E}}^+(\boldsymbol{r}_n) + \hat{\boldsymbol{E}}^-(\boldsymbol{r}_n) \right) + \hat{\boldsymbol{\mu}}_{sp} \cdot \left(\hat{\boldsymbol{E}}^+(\boldsymbol{r}_{sp}) + \hat{\boldsymbol{E}}^-(\boldsymbol{r}_{sp}) \right). \end{aligned} \tag{6.23}$$

The free photon term explicitly depends on the photon energy $\hbar v|\boldsymbol{q}|$ where $v = c/\sqrt{\varepsilon}$ is the speed of light in the surrounding environment characterized by the dielectric constant ε. The operators $\hat{a}^{\dagger}_{\boldsymbol{q}\lambda}$ and $\hat{a}_{\boldsymbol{q}\lambda}$ respectively create and destroy modes with the wave vector $\boldsymbol{q}$ and polarization λ. The interaction terms contain exciton and SP transition dipole operators $\hat{\boldsymbol{\mu}}_n = \boldsymbol{\mu}_n \hat{b}^{\dagger}_n + \boldsymbol{\mu}^*_n \hat{b}_n$ and $\hat{\boldsymbol{\mu}}_{sp} = \boldsymbol{\mu}_{sp} \hat{a}^{\dagger}_{sp} + \boldsymbol{\mu}^*_{sp} \hat{a}_{sp}$, respectively, and the electric field operators are [Lou00],

$$\hat{\boldsymbol{E}}^{+}(\boldsymbol{r}) = i \sum_{\boldsymbol{q},\lambda=1,2} \sqrt{\frac{\hbar v|\boldsymbol{q}|}{2\varepsilon_0 \varepsilon V}} \boldsymbol{e}_{\boldsymbol{q}\lambda} \hat{a}_{\boldsymbol{q}\lambda} e^{i\boldsymbol{q}\cdot\boldsymbol{r}}, \tag{6.24}$$

and $\hat{\boldsymbol{E}}^{-} = (\hat{\boldsymbol{E}}^{+})^{\dagger}$, where V is a photon mode cavity volume, and ε_0 is the vacuum permittivity.

At this point, we are ready to calculate the distribution of emitted radiation. The power radiated per solid angle may be expressed as the averaged radiation intensity operator [Lou00],

$$\frac{dP}{d\Omega} = 2\varepsilon_0 \varepsilon v r^2 \mathrm{tr}\left(\hat{\boldsymbol{E}}^{-}(\boldsymbol{r},t)\hat{\boldsymbol{E}}^{+}(\boldsymbol{r},t)\hat{\rho}_{AF}\right). \tag{6.25}$$

In order to calculate the trace, we express the electric field operators in term of the exciton and SP operators, adopting the so-called source quantity representation. [Lou00, VW06] For this purpose, we solve Heisenberg equation of motion $i\hbar\dot{\hat{\boldsymbol{E}}}^{+} = [\hat{\boldsymbol{E}}^{+}, \hat{H}_{AF} + \hat{H}_{RD}]$ in the rotating-wave approximation to find,

$$\begin{aligned} \hat{\boldsymbol{E}}^{+}(\boldsymbol{r},t) &= \frac{\boldsymbol{\mu}_n - \mathbf{e}(\mathbf{e}\cdot\boldsymbol{\mu}_n)}{4\pi\varepsilon_0\varepsilon v^2 r} \omega_n \omega_m \chi_{nm} \hat{b}_m(t - r/v) \\ &+ \sum_{nm} \frac{\boldsymbol{\mu}_{sp} - \mathbf{e}(\mathbf{e}\cdot\boldsymbol{\mu}_{sp})}{4\pi\varepsilon_0\varepsilon v^2 r} \omega^2_{sp} \chi_{sp} \hat{a}(t - r/v). \end{aligned} \tag{6.26}$$

Here, $\mathbf{e} = \boldsymbol{r}/r$, where $\boldsymbol{r}$ is the vector from the center of the SWNT to the photon

detector. The quantities

$$\chi_{nm} = \int_0^\infty \frac{d\omega}{\pi} \frac{\omega^2}{\omega_n \omega_m} \mathrm{Im}\left\{\mathcal{G}_{nm}(\omega)\right\}, \tag{6.27}$$

$$\chi_{sp} = \int_0^\infty \frac{d\omega}{\pi} \frac{\omega^2}{\omega_{sp}^2} \mathrm{Im}\left\{\mathcal{G}_{sp}(\omega)\right\}, \tag{6.28}$$

account for the photon emission line shape, and are given by integrals over the imaginary parts of exciton and SP Green functions, $\mathcal{G}_{nm}$ and $\mathcal{G}_{sp}$, associated with the Anderson-Fano model.

The exciton Green function is associated with the equation of motion for the operator $\hat{b}_m$ as determined by $\hat{H}_{AH}$ (Eq. (6.1)). Its explicit form can be written in terms of the scattering matrix [Eco84],

$$\mathcal{G}_{nm}(\omega) = \delta_{nm}\mathcal{G}_n^{(0)}(\omega) + \mathcal{G}_n^{(0)}(\omega)\mathcal{T}_{nm}(\omega)\mathcal{G}_m^{(0)}(\omega), \tag{6.29}$$

where,

$$\mathcal{G}_n^{(0)}(\omega) = \frac{1}{\omega - \omega_n + i\epsilon}, \tag{6.30}$$

is the zero-order exciton Green function, and the exciton scattering matrix,

$$\mathcal{T}_{nm}(\omega) = \boldsymbol{\mu}_n \cdot \mathbf{G}_{nm}(\omega - \Sigma_{sp}(\omega)) \cdot \boldsymbol{\mu}_m, \tag{6.31}$$

may be written in terms of the SP dyadic Green function using Eq. (6.22), whose argument depends on the self-energy

$$\Sigma_{sp}(\omega) = \sum_n \boldsymbol{\mu}_n \cdot \mathbf{G}_{nn}(\omega - \omega_{n,sp}) \cdot \boldsymbol{\mu}_n. \tag{6.32}$$

The SP Green function can be calculated in the same manner, and has the form [Mah00],

$$\mathcal{G}_{sp}(\omega) = \frac{1}{\omega - \omega_{sp} - \Sigma_{sp}(\omega) + i\epsilon}. \tag{6.33}$$

Substitution of Eq. (6.26) along with the hermitian conjugate to Eq. (6.25) gives the final expression for the radiated power,

$$\begin{aligned}\frac{dP}{d\Omega} &= \sum_{nm} \hbar\omega_n \gamma_n^{rd} f_{nn}(\Omega) \chi_{nm}^2 N_m(t - r/v) \\ &+ \hbar\omega_{sp} \gamma_{sp}^{rd} f_{sp}(\Omega) \chi_{sp}^2 N_{sp}(t - r/v) + \sum_{nm} \sum_{n'm'} \hbar \sqrt{\omega_n \omega_m \gamma_n^{rd} \gamma_m^{rd}} \\ &\times \chi_{nn'} \chi_{mm'} X_{n'm'}(t - r/v) + \sum_{nm} \hbar \sqrt{\omega_{sp} \omega_n \gamma_{sp}^{rd} \gamma_n^{rd}} f_{n,sp}(\Omega) \chi_{nm} \chi_{sp} \\ &\times (Y_{m,sp}(t - r/c) + Y_{m,sp}^*(t - r/v)).\end{aligned} \tag{6.34}$$

We observe that the angular distribution is described as a superposition of following ellipsoidal patterns

$$f_{nm}(\Omega) = \frac{3}{8\pi} \left(1 - (\mathbf{e} \cdot \boldsymbol{e}_n)(\mathbf{e} \cdot \boldsymbol{e}_m)\right), \tag{6.35}$$

$$f_{sp}(\Omega) = \frac{3}{8\pi} \left(1 - |\mathbf{e} \cdot \boldsymbol{e}_{sp}|^2\right), \tag{6.36}$$

$$f_{n,sp}(\Omega) = -\frac{3}{8\pi} (\mathbf{e} \cdot \boldsymbol{e}_n)(\mathbf{e} \cdot \boldsymbol{e}_{sp}), \tag{6.37}$$

appropriately weighted by exciton and SP radiative decay (rd) rates

$$\gamma_n^{rd} = \frac{\omega_n^3 |\boldsymbol{\mu}_n|^2}{3\pi\hbar\epsilon_0 \epsilon v^3}, \tag{6.38}$$

$$\gamma_{sp}^{rd} = \frac{\omega_{sp}^3 |\boldsymbol{\mu}_{sp}|^2}{3\pi\hbar\epsilon_0 \varepsilon v^3}, \tag{6.39}$$

respectively. These rates comprise part of the total exciton and SP decay rates, $\gamma_{sp} = \gamma_{sp}^{nr} + \gamma_{sp}^{rd}$ and $\gamma_n = \gamma_n^{nr} + \gamma_n^{rd}$, appearing in the relaxation operator in our equations of motion, Eq. (6.3). The contribution to these rates from nonradiative decay, γ_{sp}^{nr} and γ_n^{nr}, are to be determined empirically from experiment.

Finally, for $\omega_n \sim \omega_{sp}$, the ratio of photon fluxes

$$R = \frac{\gamma_{sp}^{rd} \chi_{sp}^2 N_{sp}}{\sum_{nm} \gamma_n^{rd} \chi_{nm}^2 N_m}, \tag{6.40}$$

produced by the SP and the exciton states can be introduced. Provided the contribution of the coherences in Eq. (6.34) is negligible, this quantity is reflects variation of the radiation pattern as a function of the exciton-SP coupling strength. If $R \gg 1$ ($R \ll 1$) then the radiation is dominated by the SP (exciton) dipole emission and is referred as the SP (exciton) emission. For $R \sim 1$, the emission pattern represents a superposition of both emitting dipoles.

In summary, the populations and coherences entering Eqs. (6.34) are solutions of Eqs. (6.5)-(6.8). In the weak coupling regime the coherences are given by Eqs. (6.9) and (6.10) and the populations can be determined by solving Eqs.(6.11) and (6.12). These sets of equations along with the expression for radiative power represent main results of our theory. They will now be used in the numerical calculations described below.

6.3 Numerical Calculations

In this section we discuss the results of numerical calculations of the exciton population distribution and the associated radiation patterns for three (6,5) SWNTs of different sizes in the presence of SP mode excited in Ag MT. We consider first a nanotube of length $L = 300$ nm, which is on the order of the measured value $l_D = 202$ nm of the exciton diffusion length [ABC$^+$13, CDW$^+$12]. We also consider nanotubes of lengths $L = 2600$ nm and $L = 5200$ nm. These three will be referred below as SWNT-I, SWNT-II and SWNT-III, respectively.

6.3.1 Model Parameterization

For computational purposes, each nanotube is divided into $N = L/a - 1$ sites with lattice constant $a = 1.0$ nm. This is sufficiently small to resolve the spatial depen-

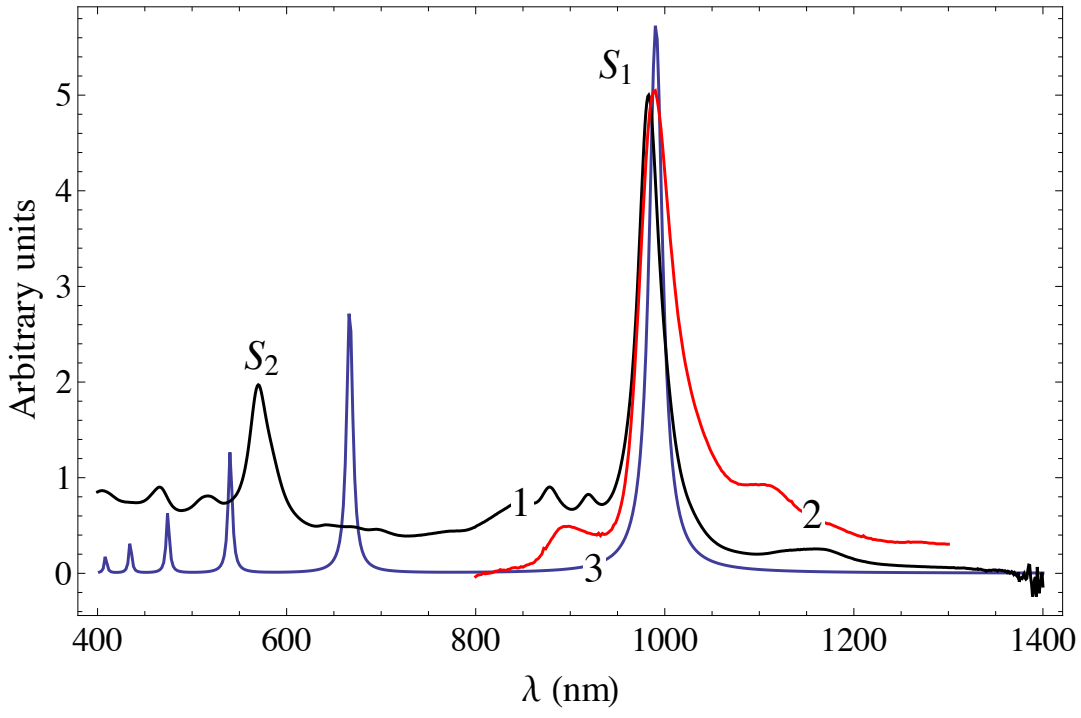

Figure 6.2: Comparison of experimentally measured [ABC$^+$13] (6,5) SWNT photoluminescence (red) and absorption (black) spectra with the simulated SP resonances polarized along z-direction (blue) for the adopted Ag MT geometry.

dencies in the Hamiltonian, but large enough to keep the calculation from becoming unwieldy. We assign a dipole moment $\mu_n = 10$ D to each of site (Fig. 6.1). Furthermore, we assume that the system is embedded into a solvent with the dielectric constant set to $\varepsilon = 1.36$. According to Eq. (6.38) the adopted dipole value corresponds to a radiative decay rate $\gamma_n^{rd} = 4.3 \times 10^{-5}$ ps^{-1} and associated decay time $\tau_n^{rd} = 23$ ns. The value of the nonradiative decay rate is set to $\gamma_n^{nr} = 1.8 \times 10^{-2}$ ps^{-1} in order to reproduce the experimentally measured [ABC$^+$13, CDW$^+$12] photoluminescence decay time $\tau_{PL} = 55$ ps. Dephasing effects due to exciton scattering are neglected in our calculations, i.e., $\tilde{\gamma}_n = 0$. Finally, the diffusion rate $D = l_D^2/a^2\tau_{PL} = 750$ ps^{-1} is determined from the measured diffusion length $l_D = 220$ nm.

To model the SP response, we consider Ag MT with the Ag bulk dielectric function represented by the Drude formula in which the parameters are fit to experiment

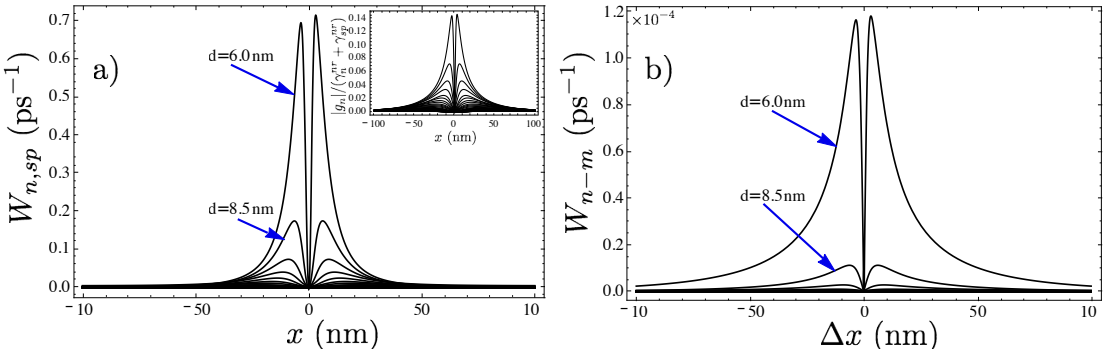

Figure 6.3: Calculated (a) exciton-SP population transfer rate (Eq. (6.13)) vs nanotube coordinate $x = na$ and (b) the SP-assisted exciton site transfer rate (Eq. (6.14)) vs $\Delta x = a(m - n)$ for various SWNT-MT distances, d. Here, we mark $d = 6$ nm and $d = 8.5$ curves only. All subsequent curves are obtained for d increased by $\Delta d = 2.5$ nm up to $d_{max} = 100$ nm. The inset shows the dimensionless parameter $|g_n|/(\gamma_n^{nr} + \gamma_{sp}^{nr})$ determining exciton-SP coupling regime. The variation in d is the same.

[JC72]. The surface coordinates, $\rho = \sqrt{x^2 + y^2}$ and z, of the MT rounded cone (Fig. 6.1) obey the equations $z = t_0 z_0 - d - t_0\sqrt{z_0^2 + \rho^2}$, where we set $t_0 = 1/8$, $z_0 = 10$ nm, and vary $0 \leq \rho \leq 400$ nm. For this MT, numerical simulations of the SP response, carried out as outlined in section 6.2.2, result in the SP resonance progression shown as a blue curve in Fig. 6.2. We identify the lowest energy SP mode $\hbar\omega_{sp} = 1.25$ eV ($\lambda = 985$ nm) as asymptotically corresponding to the SP dipole response. For the adopted parameters this SP mode is in resonance with the lowest energy S_1 exciton band and therefore interacts with the exciton states participating in the diffusion process and photon emission. Fitting the SP response with Lorentzian profile (Eq. 6.20), we find a SP nonradiative decay rate $\gamma_{sp}^{nr} = 33.4$ ps^{-1} ($\tau_{sp}^{nr} = 30$ fs) and a transition dipole moment $\mu_{sp} = 12128$ D. According to Eq. (6.39), the SP radiative decay rate becomes $\gamma_{sp}^{rd} = 56.8$ ps^{-1} ($\tau_{sp}^{rd} = 18$ fs).

Photoluminescence is typically excited via high energy S_2 absorption at $\lambda = 570$ nm followed by rapid internal conversion to the S_1 band [ABC+13]. According to Fig. 6.2 The S_2 band does not overlap with any SP resonances of the MT. As

a result this model consistently accounts for the SP effect on the exciton diffusion and emission within the S_1 band only, and does not require consideration of SP enhancement of the exciton photo-generation processes. Assuming that SWNT is photo-excited homogeneously, we set the exciton population gain $I_n = \gamma_n^{nr}$, for all n.

With the parameters as discussed above, we solve numerically Eqs. (6.11)-(6.13). The solutions were benchmarked against solutions of Eqs. (6.5)–(6.8) and found to be indistinguishable, indicating that the weak exciton-SP coupling approximation is valid. Numerical evaluation of the integral quantities χ_{nm} and χ_{sp} (Eqs. (6.27) and (6.28)) shows that $\chi_{nm} \approx \delta_{nm}$ and $\chi_{sp} \approx 1$ for the parameter range of interest.

6.3.2 Simulation Results

Key quantities defining the effect of the SP on exciton diffusion, such as exciton-SP and the SP-assisted exciton site transfer rates, are plotted in panels (a) and (b) of Fig. 6.3. The plot shows that the effective exciton-SP interaction range is constrained to an interval of $\sim$ 100 nm around the origin. Increasing d leads to a rapid decrease of the rates and the effective interaction length. The diffusion rate ($D = 750$ ps^{-1}) significantly exceeds the population transfer rate which in turn has significant effect on the exciton populations profile, as we show below. On the other hand, the SP-assisted exciton site transfer rate (panel (b)) is small compared to the exciton-SP transfer rate (panel (a)), and has weak effect. Finally, we find that the dimensionless parameter, $|g_n|/(\gamma_n^{nr} + \gamma_{sp}^{nr})$ is below 0.15 for all n, which is consistent with the weak exciton-SP coupling assumption made in deriving of the approximate rate Eqs. (6.11)-(6.14).

Let us first examine how the exciton-SP interaction influences the steady state exciton distribution, N_n, obtained from solution of Eqs. (6.11)-(6.14). This quantity is plotted in panels (a), (b), and (c) of Fig. 6.4 for SWNT-I, II, and III, respectively. The diffusion boundary conditions [CDW$^+$12] require vanishing populations

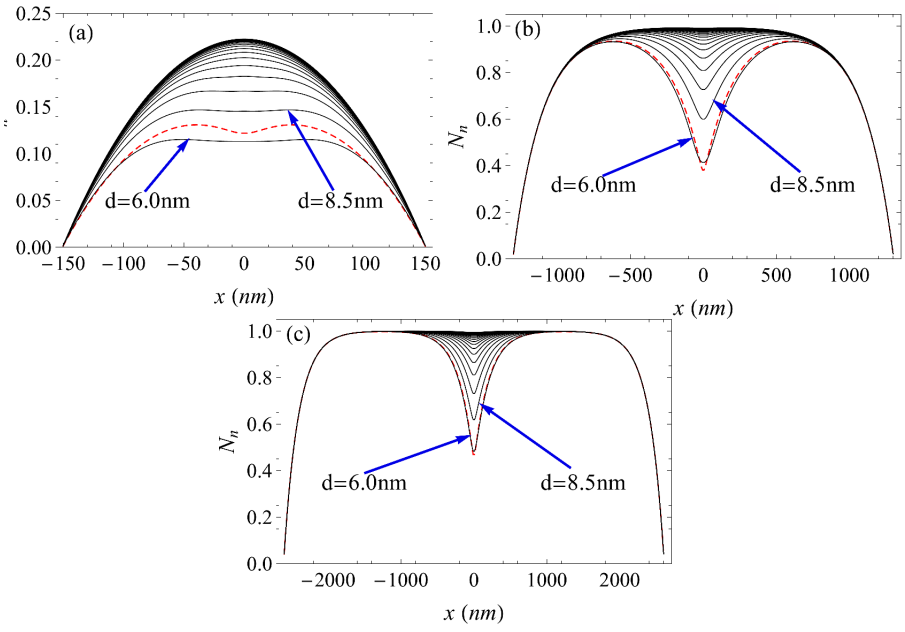

Figure 6.4: Calculated steady state exciton distribution along (a) SWNT-I, (b) SWNT-II, and (c) SWNT-III as a function of SWNT coordinate $x = na$. Here, we mark $d = 6$ nm and $d = 8.5$ curves. All subsequent curves are obtained with the distance increased by $\Delta d = 2.5$ nm up to $d_{max} = 100$ nm. Red dash shows the exciton population in the absence of the SP-assisted exciton site population transfer with the rate W_{nm} for $d = 6$ nm.

at the SWNT ends. As a result, the SP-uncoupled excitons population distributions ($d \sim 100$ nm) deviate from a rectangular profile, showing a smooth drop of the end populations, the effect being strong in shorter nanotubes. Interaction with the SP modes causes a population dip around $x = 0$, reaching maximum depth at small d. We find that the main contribution to this dip is from the exciton-SP population transfer at the rate $W_{n,sp}$ (Eqs. (6.11) and (6.12)). The SP-assisted exciton site transfer at the rate W_{nm} slightly changes the dip. This is seen from the behavior of the red dashed curve representing the solution of Eqs. (6.11) and (6.12) with W_{nm} set to zero. We find a tiny ratio of N_{sp} to the exciton population within the SP-dip, showing that most of the exciton energy transferred to the SP is dissipated to heat (Ohmic loss).

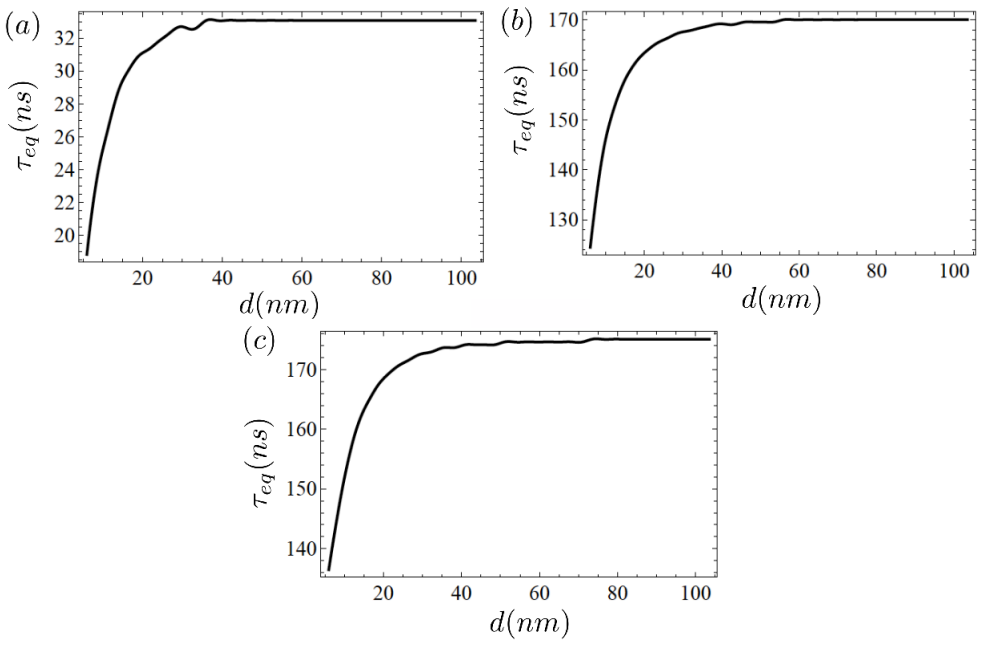

Figure 6.5: Variation of the equilibration time, τ_{eq}, required to reach the steady state exciton populations as a function of SWNT-MT separation, d, for (a) SWNT-I, (b) SWNT-II, and (c) SWNT-III.

Next, we examine the transient population dynamics characterized by the exciton equilibration time, τ_{eq}, required to reach the steady state solutions (Fig. 6.4). We present τ_{eq} vs d in panels (a), (b), and (c) of Fig. 6.5 for SWNT-I, II, and III, respectively. At large MT-SWNT separation ($d \sim 100$ nm), this quantity approaches the equilibration time for uncoupled excitons. The SWNT size (boundary) imposes an upper limit on the equilibration time which is faster for short SMNTs (compare panel (a) with (b) and (c)). The SP induced reduction in τ_{eq} is noticeable for $d \lesssim$ 50 nm regardless of the tube length. We also examined the effect of SP-assisted exciton transfer (not shown in the plot) and found it to be negligible. We thus conclude that the SP modifies transient dynamics primarily from the exciton-SP population transfer, accompanied by Ohmic loss.

At this point we turn our attention to the radiation emission properties of the SWNT-MT system by examining the photon flux ratio, R, (Eq. (6.40)) and the

associated radiation angular distribution (Eqs. (6.34)–(6.38)) due to the steady state exciton and SP populations (Fig. 6.4). As pointed out in Sec. 6.2.3, R distinguishes between the SP ($R \gg 1$) and exciton ($R \ll 1$) emissions if the contribution of the coherences $Y_{n,sp}$ and X_{nm} to Eq. (6.34) is negligible. This is exactly the case if $\omega_n = \omega_{sp}$, but it is also true if $\omega_n \neq \omega_{sp}$ provided that ω_n is a random variable (reflecting diagonal energy disorder) with a mean value equal to ω_{sp}. If there is a fixed frequency detuning $\Delta\omega = \omega_n - \omega_{sp}$ for all n, one can apply symmetry arguments, including the fact that the coupling frequency g_n is antisymmetric function, i.e., $g_n = -g_{-n}$, to make the case that for the MT located at the center (or more specifically away from the ends) of the nanotube (Fig. 6.1), the coherences vanish identically. This can be easily demonstrated by looking at the dipole-dipole interaction form for g_n and has been numerically validated for small d when this approximation beaks down.

Panels (a), (b), and (c) in Fig. 6.6 present R plotted vs d for SWNT-I, SWNT-II, and SWNT-III, respectively. The radiation emission is dominated by the SP dipole (red segments) with the angular distribution shown by red curves in the inset to panel (b) for d in a range of a few tens nanometers. For the short SWNT-I, SP-dominated emission occurs for $d \lesssim 40$ nm, whereas, for the long SWNT-II and SWNT-III, it occurs for $d \lesssim 20$ nm and $d \lesssim 10$ nm, respectively. This observation can be rationalized by examining the exciton population distribution shown in Fig. 6.4. For SWNT-I, the exciton-SP interaction range (Fig. 6.3 (a)) is about the size of the nanotube. According to Fig. 6.4 (a), this results in a significant reduction of the exciton population across the SWNT-I. Therefore, the total exciton contribution to the radiated power decreases. In contrast, for long SWNT-II and III (Fig. 6.4 (b) and (c)) only the excitons near the center of the nanotube suffer drastic population reduction, and there is significant photoexcited exciton population outside the interaction region that enhances the exciton emission component. This shows that a stronger coupling (i.e.,smaller d) is needed to reach the SP-dominated emission regime.

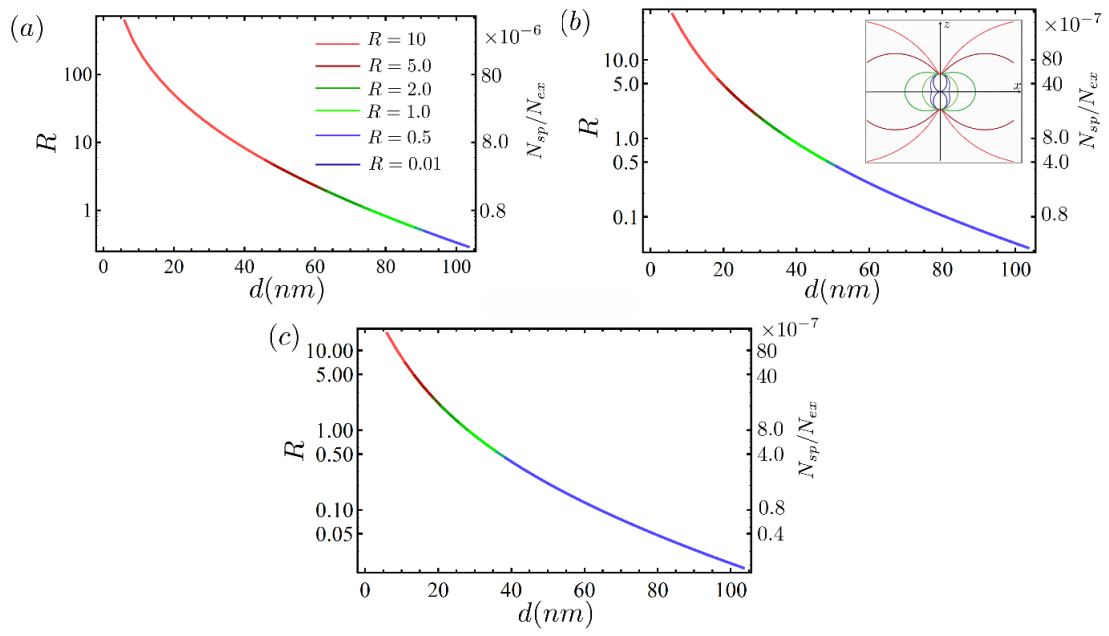

Figure 6.6: The ratio of the SP and the exciton radiation fluxes, R, and associated ratio of the state populations, N_s/N_{ex}, where $N_{ex} = \sum_n N_n$, for (a) SWNT-I (b) SWNT-II, and (c) SWNT-III as a function of the SWNT-MT separation d. The inset in panel (a) shows color code for different segments of the cure distinguishing SP (red) and exciton (blue) emissions. The green segment denotes the crossover regime. This color code applies to all panels including the inset in (b) which shows the associated radiation angular distributions.

According to Eq. (6.40), there are two main quantities determining the angular distribution of emitted radiation. One is the ratio of the steady state SP and exciton populations, N_{sp}/N_{ex} with $N_{ex} = \sum_n N_n$, plotted in Fig. 6.6 (right scale). The other is the ratio of their radiative decay rates, $\gamma_{sp}^{rd}/\gamma_n^{rd} = 1.3 \times 10^6$. Fig. 6.6 shows that the total population transferred to the SP state from the coupled exciton states is five to seven orders of magnitude less than the exciton population, a consequence of weak coupling. However, a large ratio of the radiative decay rates (associated with the large values of the SP transition dipoles) compensates for the low population, allowing the SP state to dominate the angular distribution at small d. In other words, it is primarily the fast SP emission rate that causes the angular distribution to be SP-dominated. Increasing d leads to a rapid SP population drop, causing a shift to

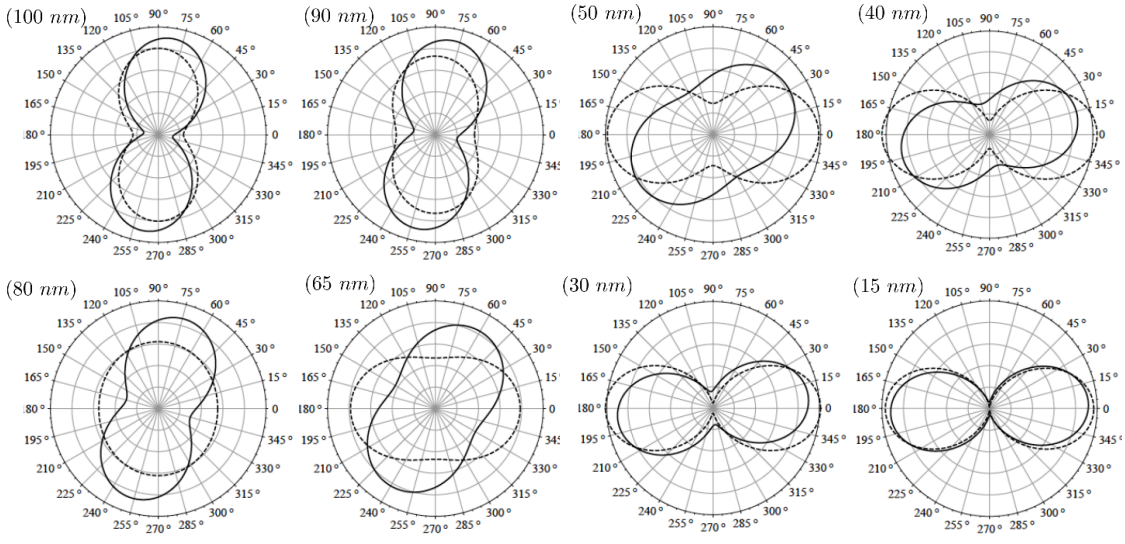

Figure 6.7: Radiation angular distribution of SWNT-I with the energy detuned to $\hbar\Delta\omega = 10$ meV plotted for various SWNT-MT distances ranging between $d = 100$ nm and $d = 15$ nm as indicated in parenthesis. The angle is measured with respect to the x-axis in Fig. 6.1. Solid lines mark the distributions associated with the MT placed at the end of the nanotube, i.e., $x = 150$ nm. Dashed lines are for the MT located at the center, i.e., $x = 0$.

the exciton-dominated emission regime (blue segments in Fig. 6.6). The evolution of the radiation angular distribution as a function of d can be seen in the inset to Fig. 6.6 (b).

Finally, we note that the coherences can have a strong influence on the orientation of the radiation diagram when the inversion symmetry is broken, especially in small nanotubes in which the emission from excitons outside the interaction region is minimized. For example, let us break the symmetry of the g_n in SWNT-I by placing the MT at the end of the tube, at $x = 150$ nm, and let us also detune the exciton energy from the SP by $\hbar\Delta\omega = 10$ meV. Our results are shown in Fig. 6.7, where we compare the radiation angular distributions associated with the MT placed at the end (solid lines), and at the center (dash lines), of the nanotube, parametric in d. The general trend is that the nonvanishing coherences induce rotation of the radiation diagram. The effect is strongest for the distance range corresponding to $R \sim 1$, which is the

crossover regime (green segment) in Fig. 6.6. Our data analysis also indicates that the dominant contribution to the diagram rotation originates from $Y_{n,sp}$. The X_{nm} contribution to the radiated power is weak because the system is in the regime of weak coupling. In this case X_{nm} is a perturbative correction to $Y_{n,sp}$. This effect is similar to what we observed comparing contributions of $W_{n,sp}$ associated with $Y_{n,sp}$ and W_{nm} associated with the X_{nm}.

To rationalize this effect we should recall that an exciton dipole behaving *incoherently*, i.e., without any information about its oscillation phase, merely transfers energy to the SP dipole. As a result, the exciton and SP dipoles become excited together, but the overall radiation pattern is a superposition of their intensities (see inset to Fig. 6.6 (b)). In contrast, a sustained oscillation of the coherences introduces a phase shift in the exciton and SP dipoles, and they behave as a *a single* superposition dipole whose orientation depends on the phase shift. Such a phase shift corresponds to the radiation diagram of a rotated effective dipole as observed in Fig. 6.7. Quantum mechanically this effect can be explained as the emission associated with spatially reoriented superposition dipole whose matrix elements are calculated in the dressed exciton-SP eigenstates. The effect is most noticeable in the crossover regime because the net contribution of the excitons and SP to the emitted power are about the same.

6.4 Conclusion

We have developed a general theoretical approach to study exciton transport and emission in a SWNT in the presence of a localized SP mode within a MT interacting via near-field coupling. Our primary result is a set of quantum mechanical equations of motion (Eqs. (6.5)–(6.8)) that account for the exciton, SP, and the environment (including radiation mode) on the same footing. These material equations are complemented by the expressions for the radiated power (Eqs. (6.34)–(6.38))

which depends on the exciton and SP populations and coherences, allowing for an examination of the angular distribution (and spectrum) of the emitted radiation. The model is capable of describing both strong and weak exciton-SP coupling regimes, as well as the transition from ballistic to diffusive transport, thus spanning a broad range of behaviors in low-dimensional semiconductor materials.

In this Chapter, the weak exciton-SP limit has been examined in detail. Using a perturbation approach, with the exciton-SP coupling frequency normalized per dissipation rate as the expansion parameter, we have derived a minimal set of rate equations (Eq. (6.11)–(6.14)) for the exciton and SP populations. These equations account for the exciton-SP population transfer and SP-assisted exciton site transfer processes with their associated rates given by Eqs. (6.13) and (6.14), respectively. The expressions for the rates are represented in terms of the dyadic Green function, which is determined via numerical calculations of the SP response, allowing for consideration of a Ag tip in the shape of a rounded cone. The exciton-SP and site exciton transfer matrix elements required in this model have been extensively considered in the literature and Chapter 3 in the context of the Förster energy transfer to metal and between donor and acceptor sites. In fact, master equations with rates determined by the dyadic Green function have been introduced in the same manner [GLK07, DRKS08, ZLS$^+$13, PS11]. The difference (and advantage) of the present treatment is that the steady state coherences (Eqs. (6.9) and (6.10)) have been retained in expressions for the radiated power. They play an important role in its analysis, as demonstrated in Sec. 6.3.2. Furthermore, we have established a simple relationship (Eq. (6.22)) between the dyadic Green function and the exciton-SP coupling frequency that allows one to obtain the latter quantity from simulation.

Numerical simulations for various sizes of (6,5) SWNT and Ag MT have been performed using our proposed methodology. We have found that the near-field interaction between the exciton-SP is efficient on 100 nm lengthscales or less and occurs in the weak coupling regime with diffusion processes being much faster than the exciton-

SP population exchange. Exciton-SP population transfer dominates over SP-assisted site exciton transfer, resulting in fast energy transfer to the MT with subsequent dissipation (i.e., Förster energy transfer). The exciton-SP energy transfer also causes a reduction in equilibration time for excitons to reach their steady sate distributions. Analysis of radiation emission properties shows that the radiation diagram is dominated by SP emission for a SWNT-MT separation of a few tens of nanometers. In small SWNTs, whose length is on the order of the effective exciton-SP interaction range, this effect requires weaker coupling to the plasmon than in long SWNTs for which delocalized excitons provide an additional contribution to the radiated power. We have found that the SP population in the steady state regime is orders of magnitude below the exciton population, and yet the fast SP radiative decay rate still makes the SP emission more efficient. Finally, we found that breaking the inversion-symmetry of the exciton-SP interaction by moving the MT away from the center of the SWNT causes a rotation in the radiation pattern that depends on the strength of the coherences.The rotation can be understood as the emission pattern of a tilted dipole comprised of hybridized exciton-SP eigenstates.

In conclusion, exciton diffusion in SWNT affected by a localized SP mode has been systematically modeled using a unified approach. We have calculated the influence of exciton-SP energy transfer and dissipation on radiative power and angular distribution. We find that the shape of the radiation pattern depends on the interplay between the exciton-SP state populations and radiative decay rates, and that a high ratio of the SP to exciton radiative rates is what causes the emission to be SP-dominated. We demonstrate that the coherences can play significant role in the pattern orientation.

Chapter 7

Conclusion

We have explored some topics of transport in nanoscale systems coupled to metal surfaces. First we looked at the effect of SP resonances on the FRET rate between QDs. We found that amount of enhancement depends greatly on the material properties and geometry of MNPs. In Chapter 4, we explored the dynamics of a charge moving above a metal slab. We developed a Hamiltonian formalism suited for both classical and quantum descriptions of low energy electron-SP interactions. From a classical perspective we were able to convert a non-linear intergro-differential equation into a set of first ordered equations by transforming the problem into a Hamiltonian system. Based on this, we then developed a theory of QSPs that is applicable in the adiabatic (slow electron, fast SP) limit. We showed that the conclusions reached by previous authors regarding the SP repulsion are flawed, because they failed to properly account for the adiabatic nature of the effect they were describing [ŠTL72, RM72]. In Chapter 5, we then expanded the formalism, and considered a charge carrier in a SWNT coupled to a MNP. We show the existence of a zero-point repulsion due to the ground state energy of the QSP, and proposed an experimental setup to test for the existence of this effect. In Chapter 6, we reported on the systematic investigation of the effects of a localized SP mode on exciton transport and emission properties in

a SWNT. We again approached the problem from a quantum perspective and found the that it mapped onto the well known Fano-Anderson model. We showed that the population dynamics between excitons and SPs leads to measurable changes in the emission spectrum.

The main theme of this work has been to explore the transport properties of charge carriers and energy in the presence of SPs. We have focused on some of the novel effects that can occur when the SP is treated as a quantum mechanical oscillator. We hope that the methods developed in this thesis can be expanded upon and used to further explore the unique properties of semi-conductor/SP coupled hybrid nano-structures.

References

[AB08] Ryan D Artuso and Garnett W Bryant, *Optical response of strongly coupled quantum dot- metal nanoparticle systems: Double peaked fano structure and bistability*, Nano letters **8** (2008), no. 7, 2106–2111.

[ABC+13] Michael S Arnold, Jeffrey L Blackburn, Jared J Crochet, Stephen K Doorn, Juan G Duque, Aditya Mohite, and Hagen Telg, *Recent developments in the photophysics of single-walled carbon nanotubes for their use as active and passive material elements in thin film photovoltaics*, Physical Chemistry Chemical Physics **15** (2013), no. 36, 14896–14918.

[Ach10] Marc Achermann, *Exciton- plasmon interactions in metal- semiconductor nanostructures*, The Journal of Physical Chemistry Letters **1** (2010), no. 19, 2837–2843.

[AD12] Hadiseh Alaeian and Jennifer A Dionne, *Plasmon nanoparticle superlattices as optical-frequency magnetic metamaterials*, Optics Express **20** (2012), no. 14, 15781–15796.

[AE05] Andrea Alù and Nader Engheta, *Achieving transparency with plasmonic and metamaterial coatings*, Physical Review E **72** (2005), no. 1, 016623.

[AM05] Neil W Ashcroft and N David Mermin, *Solid state physics (holt, rinehart and winston, new york, 1976)*, There is no corresponding record for this reference (2005).

[AMY+07] AV Akimov, A Mukherjee, CL Yu, DE Chang, AS Zibrov, PR Hemmer, H Park, and MD Lukin, *Generation of single optical plasmons in metallic nanowires coupled to quantum dots*, Nature **450** (2007), no. 7168, 402–406.

[ANP+13] Chellachamy Anbalagan Amarnath, Sitansu Sekhar Nanda, Georgia C Papaefthymiou, Dong Kee Yi, and Ungyu Paik, *Nanohybridization of*

low-dimensional nanomaterials: Synthesis, classification, and application, Critical Reviews in Solid State and Materials Sciences **38** (2013), no. 1, 1–56.

[Bar77] G Barton, *Quantum mechanics of charged particles near a plasma surface*, Journal of Physics A: Mathematical and General **10** (1977), no. 4, 601.

[Bar79] _____, *Some surface effects in the hydrodynamic model of metals*, Reports on Progress in Physics **42** (1979), no. 6, 963.

[BDE03] William L Barnes, Alain Dereux, and Thomas W Ebbesen, *Surface plasmon subwavelength optics*, Nature **424** (2003), no. 6950, 824–830.

[BGL+99] Dieter Bimberg, Marius Grundmann, Nikolai N Ledentsov, et al., *Quantum dot heterostructures*, vol. 471973882, John Wiley Chichester, 1999.

[BH57] HAH Boot and RBRS Harvie, *Charged particles in a non-uniform radio-frequency field*, Nature **180** (1957), no. 4596, 1187.

[BH70] D Beaglehole and O Hunderi, *Study of the interaction of light with rough metal surfaces. i. experiment*, Physical Review B **2** (1970), no. 2, 309.

[BHG+10] Miriam Böhmler, Nicolai Hartmann, Carsten Georgi, Frank Hennrich, Alexander A Green, Mark C Hersam, and Achim Hartschuh, *Enhancing and redirecting carbon nanotube photoluminescence by an optical antenna*, Optics express (2010), no. 16, 16443–16451.

[Bir70] John B Birks, *Photophysics of aromatic molecules*.

[Boy68] Timothy H Boyer, *Quantum electromagnetic zero-point energy of a conducting spherical shell and the casimir model for a charged particle*, Physical Review **174** (1968), no. 5, 1764.

[BP55] John Bardeen and David Pines, *Electron-phonon interaction in metals*, Physical Review **99** (1955), no. 4, 1140.

[BRB55] A. W. Blackstock, R. H. Ritchie, and R. D. Birkhoff, *Mean free path for discrete electron energy losses in metallic foils*, Phys. Rev. **100** (1955), 1078–1083.

[BS03] David J Bergman and Mark I Stockman, *Surface plasmon amplification by stimulated emission of radiation: quantum generation of coherent surface plasmons in nanosystems*, Physical review letters **90** (2003), no. 2, 027402.

[BS04] DJ Bergman and MI Stockman, *Can we make a nanoscopic laser?*, LASER PHYSICS-LAWRENCE- **14** (2004), no. 3, 409–411.

[BVD+06] Sergey I Bozhevolnyi, Valentyn S Volkov, Eloise Devaux, Jean-Yves Laluet, and Thomas W Ebbesen, *Channel plasmon subwavelength waveguide components including interferometers and ring resonators*, Nature **440** (2006), no. 7083, 508–511.

[CA74] Michele Cini and P Ascarelli, *Quantum size effects in metal particles and thin films by an extended rpa*, Journal of Physics F: Metal Physics **4** (1974), no. 11, 1998.

[CDW+12] Jared J Crochet, Juan G Duque, James H Werner, Brahim Lounis, Laurent Cognet, and Stephen K Doorn, *Disorder limited exciton transport in colloidal single-wall carbon nanotubes*, Nano letters **12** (2012), no. 10, 5091–5096.

[Cle03] Andrew N Cleland, *Foundations of nanomechanics: from solid-state theory to device applications*.

[CPD13] Charles Cherqui, Andrei Piryatinski, and David Dunlap, *Nanoscale effects on charge transport due to surface-plasmon induced quantum image forces*, Bulletin of the American Physical Society **58** (2013).

[CPS78] RR Chance, A Prock, and R Silbey, *Molecular fluorescence and energy transfer near interfaces*, Adv. Chem. Phys **37** (1978), no. 1, 65.

[CR68] Julian Crowell and RH Ritchie, *Radiative decay of coulomb-stimulated plasmons in spheres*, Physical Review **172** (1968), 436–440.

[CSHL05] DE Chang, AS Sorensen, PR Hemmer, and MD Lukin, *Quantum optics with surface plasmons*, arXiv preprint quant-ph/0506117 (2005).

[dAH02] FJ García de Abajo and A Howie, *Retarded field calculation of electron energy loss in inhomogeneous dielectrics*, Physical Review B **65** (2002), no. 11, 115418.

[Das77] Basab B Dasgupta, *Surface plasmon dispersion for very small metallic spheres: A quantum mechanical formulation*, Zeitschrift für Physik B Condensed Matter **27** (1977), no. 1, 75–79.

[Deb10] Peter Debye, *Zur theorie der elektronen in metallen*, Annalen der Physik **338** (1910), no. 13, 441–489.

[Dir47] Paul Adrien Maurice Dirac, *The principles of quantum mechanics*, The International Series of Monographs on Physics, Oxford: Clarendon Press, 1947 **1** (1947).

[dLSC+12] Nathalie P de Leon, Brendan J Shields, L Yu Chun, Dirk E Englund, Alexey V Akimov, Mikhail D Lukin, and Hongkun Park, *Tailoring light-matter interaction with a nanoscale plasmon resonator*, Physical Review Letters **108** (2012), no. 22, 226803.

[Dor64] RH Doremus, *Plasma resonances in small metallic particles*, Journal of Applied Physics **35** (1964), 3456.

[DRKS08] Maxim Durach, Anastasia Rusina, Victor I Klimov, and Mark I Stockman, *Nanoplasmonic renormalization and enhancement of coulomb interactions*, New Journal of Physics **10** (2008), no. 10, 105011.

[Eco84] Eleftherios N Economou, *Green's functions in quantum physics*, vol. 3, Springer, 1984.

[ELG+98] Thomas W Ebbesen, HJ Lezec, HF Ghaemi, T Thio, and PA Wolff, *Extraordinary optical transmission through sub-wavelength hole arrays*, Nature **391** (1998), no. 6668, 667–669.

[EN74] EN Economou and KI Ngai, *Surface plasma oscillations and related surface effects in solids*, Adv. Chem. Phys **27** (1974), 265–354.

[ER70] JM Elson and RH Ritchie, *Photon-surface plasmon coupling at a dielectric solid*, Physics Letters A **33** (1970), no. 4, 255–256.

[ERBI81] P. M. Echenique, R. H. Ritchie, N. Barberán, and John Inkson, *Semiclassical image potential at a solid surface*, Phys. Rev. B **23** (1981), 6486–6493.

[ERW+05] Florian Evers, Christoph Rakete, Kazuo Watanabe, Dietrich Menzel, and Hans-Joachim Freund, *Two-photon photoemission from silver nanoparticles on thin alumina films: Role of plasmon excitation*, Surface science **593** (2005), no. 1, 43–48.

[ES] Ulrich Eckern and Éric Suraud, *Quantum dissipation and decoherence of collective excitations in metallic nanoparticles.*

[EU91] PM Echenique and ME Uranga, *Image potential states at surfaces*, Surface Science **247** (1991), no. 2, 125–132.

[Fer58] Richard A Ferrell, *Predicted radiation of plasma oscillations in metal films*, Physical Review **111** (1958), no. 5, 1214.

[FKI67] Fuminori Fujimoto, Ken-ichiro Komaki, and Kohtaro Ishida, *Surface plasma oscillation in aluminum fine particles*, Journal of the Physical Society of Japan **23** (1967), no. 5, 1186–1186.

[För48] Th Förster, *Zwischenmolekulare energiewanderung und fluoreszenz*, Annalen der physik **437** (1948), no. 1-2, 55–75.

[För60] ———, *Transfer mechanisms of electronic excitation energy*, Radiation Research Supplement (1960), 326–339.

[Frö54] H Fröhlich, *Electrons in lattice fields*, Advances in Physics **3** (1954), no. 11, 325–361.

[FTS+07] Y Fedutik, VV Temnov, O Schöps, U Woggon, and MV Artemyev, *Exciton-plasmon-photon conversion in plasmonic nanostructures*, Physical review letters **99** (2007), no. 13, 136802.

[Gat12] Malte C Gather, *A rocky road to plasmonic lasers*, Nature Photonics **6** (2012), no. 11, 708–708.

[GBQ+09] Carsten Georgi, Miriam Böhmler, Huihong Qian, Lukas Novotny, and Achim Hartschuh, *Probing exciton propagation and quenching in carbon nanotubes with near-field optical microscopy*, physica status solidi (b) **246** (2009), no. 11-12, 2683–2688.

[Ger71] E. Gerlach, *Equivalence of van der waals forces between solids and the surface-plasmon interaction*, Phys. Rev. B **4** (1971), 393–396.

[GH09] R Gans and H Happel, *Zur optik kolloidaler metallösungen*, Annalen der Physik **334** (1909), no. 7, 277–300.

[GLK07] Alexander O Govorov, Jaebeom Lee, and Nicholas A Kotov, *Theory of plasmon-enhanced förster energy transfer in optically excited semiconductor and metal nanoparticles*, Physical Review B **76** (2007), no. 12, 125308.

[GN80] Joel Gersten and Abraham Nitzan, *Electromagnetic theory of enhanced raman scattering by molecules adsorbed on rough surfaces*, The Journal of Chemical Physics **73** (1980), no. 7, 3023.

[Gol62] Herbert Goldstein, *Classical mechanics*.

[GRJ+65] Izrail Solomonovich Gradshteyn, Iosif Moiseevich Ryzhik, Alan Jeffrey, Daniel Zwillinger, and Scripta Technica, *Table of integrals, series, and products*.

[GTG+98] HF Ghaemi, Tineke Thio, DE e al Grupp, Thomas W Ebbesen, and HJ Lezec, *Surface plasmons enhance optical transmission through subwavelength holes*, Physical Review B **58** (1998), no. 11, 6779.

[GVMD09] DE Gomez, KC Vernon, Paul Mulvaney, and TJ Davis, *Surface plasmon mediated strong exciton- photon coupling in semiconductor nanocrystals*, Nano letters **10** (2009), no. 1, 274–278.

[GVMD10] ———, *Coherent superposition of exciton states in quantum dots induced by surface plasmons*, Applied Physics Letters **96** (2010), no. 7, 073108–073108.

[GZ13] Pavel Ginzburg and Anatoly V Zayats, *Linewidth enhancement in spasers and plasmonic nanolasers*, Optics express **21** (2013), no. 2, 2147–2153.

[Hal86] WP Halperin, *Quantum size effects in metal particles*, Reviews of Modern Physics **58** (1986), no. 3, 533.

[HB70] O Hunderi and D Beaglehole, *Study of the interaction of light with rough metal surfaces. ii. theory*, Physical Review B **2** (1970), no. 2, 321.

[HB80] Lillian H Hoddeson and Gordon Baym, *The development of the quantum mechanical electron theory of metals: 1900-28*, Proceedings of the Royal Society of London. A. Mathematical and Physical Sciences **371** (1980), no. 1744, 8–23.

[HL94] Wen Chu Huang and Juh Tzeng Lue, *Quantum size effect on the optical properties of small metallic particles*, Physical Review B **49** (1994), no. 24, 17279.

[HLO07] Joel Henzie, Min Hyung Lee, and Teri W Odom, *Multiscale patterning of plasmonic metamaterials*, Nature nanotechnology **2** (2007), no. 9, 549–554.

[HO77] J Hubbard and L Onsager, *Dielectric dispersion and dielectric friction in electrolyte solutions. i.*, The Journal of Chemical Physics **67** (1977), 4850.

[Hol59] Th Holstein, *Studies of polaron motion: Part i. the molecular-crystal model*, Annals of Physics **8** (1959), no. 3, 325–342.

[HS03] Encai Hao and George C Schatz, *Electromagnetic fields around silver nanoparticles and dimers*, The Journal of chemical physics **120** (2003), no. 1, 357–366.

[HT12] Ulrich Hohenester and Andreas Trügler, *Mnpbem–a matlab toolbox for the simulation of plasmonic nanoparticles*, Computer Physics Communications **183** (2012), no. 2, 370–381.

[HWD82] A Hartstein, ZA Weinberg, and DJ DiMaria, *Experimental test of the quantum-mechanical image-force theory*, Physical Review B **25** (1982), no. 12, 7174.

[JC72] Peter B Johnson and R-W_ Christy, *Optical constants of the noble metals*, Physical Review B **6** (1972), no. 12, 4370.

[JF99] John David Jackson and Ronald F Fox, *Classical electrodynamics*, American Journal of Physics **67** (1999), 841.

[Jon80] M Jonson, *The dynamical image potential for tunneling electrons*, Solid State Communications **33** (1980), no. 7, 743–746.

[JS69] SN Jasperson and SE Schnatterly, *Photon-surface-plasmon coupling in thick ag foils*, Physical Review **188** (1969), no. 2, 759.

[JS11] Zubin Jacob and Vladimir Shalaev, *Plasmonics goes quantum.*

[KBR+08] Vamsi K Komarala, A Louise Bradley, Yury P Rakovich, Stephen J Byrne, Yurii K Gunko, and Andrey L Rogach, *Surface plasmon enhanced förster resonance energy transfer between the cdte quantum dots*, Applied Physics Letters **93** (2008), no. 12, 123102–123102.

[KF69] U Kreibig and C v Fragstein, *The limitation of electron mean free path in small silver particles*, Zeitschrift für Physik **224** (1969), no. 4, 307–323.

[KF74] KL Kliewer and R Fuchs, *Theory of dynamical properties of dielectric surfaces*, Adv. Chem. Phys **27** (1974), 355–541.

[KG85] U Kreibig and L Genzel, *Optical absorption of small metallic particles*, Surface Science **156** (1985), 678–700.

[KGB+09] Roman Kolesov, Bernhard Grotz, Gopalakrishnan Balasubramanian, Rainer J Stöhr, Aurélien AL Nicolet, Philip R Hemmer, Fedor Jelezko, and Jörg Wrachtrup, *Wave–particle duality of single surface plasmon polaritons*, Nature Physics **5** (2009), no. 7, 470–474.

[KK66] Arisato Kawabata and Ryogo Kubo, *Electronic properties of fine metallic particles. ii. plasma resonance absorption*, J. Phys. Soc. Jpn **21** (1966), 1765–1772.

[KKK84] Ryogo Kubo, Arisato Kawabata, and Shun-ichi Kobayashi, *Electronic properties of small particles*, Annual Review of Materials Science **14** (1984), no. 1, 49–66.

[KM97] Charles L Kane and EJ Mele, *Size, shape, and low energy electronic structure of carbon nanotubes*, Physical Review Letters **78** (1997), no. 10, 1932.

[KMK89] Leonid Veniaminovich Keldysh, Alexei A Maradudin, and DA Kirzhnitz, *The dielectric function of condensed systems*.

[KPG+98] T Klar, M Perner, S Grosse, G Von Plessen, W Spirkl, and J Feldmann, *Surface-plasmon resonances in single metallic nanoparticles*, Physical Review Letters **80** (1998), no. 19, 4249.

[Kre92] Vitaly V Kresin, *Collective resonances and response properties of electrons in metal clusters*, Physics reports **220** (1992), no. 1, 1–52.

[KSS09] AS Kirakosyan, MI Stockman, and TV Shahbazyan, *Surface plasmon lifetime in metal nanoshells*, arXiv preprint arXiv:0908.0647 (2009).

[KTS+13] Arunandan Kumar, Priyanka Tyagi, Ritu Srivastava, DS Mehta, and MN Kamalasanan, *Energy transfer process between exciton and surface plasmon: Complete transition from forster to surface energy transfer*, Applied Physics Letters **102** (2013), 203304.

[Kub62] Ryogo Kubo, *Electronic properties of metallic fine particles. i.*, Journal of the Physical Society of Japan **17** (1962), 975.

[Kum13] Ashok Kumar, *Ponderomotive self-focusing of surface plasma wave*, Plasmonics (2013), 1–5.

[Kup63] Charles Goethe Kuper, *Polarons and excitons*, Physics Today **16** (1963), 106.

[KWK+97] Katrin Kneipp, Yang Wang, Harald Kneipp, Lev T Perelman, Irving Itzkan, Ramachandra R Dasari, and Michael S Feld, *Single molecule detection using surface-enhanced raman scattering (sers)*, Physical review letters **78** (1997), no. 9, 1667.

[KZ70] Uwe Kreibig and Peter Zacharias, *Surface plasma resonances in small spherical silver and gold particles*, Zeitschrift für Physik **231** (1970), no. 2, 128–143.

[LBB96] W Klopper Leutwyler, S Leutwyler Bürgi, and HB Burgl, *Semiconductor clusters, nanocrystals, and quantum dots*, Science **271** (1996), no. 5251, 933–937.

[LBU+08] Fei Le, Daniel W Brandl, Yaroslav A Urzhumov, Hui Wang, Janardan Kundu, Naomi J Halas, Javier Aizpurua, and Peter Nordlander, *Metallic nanoparticle arrays: a common substrate for both surface-enhanced raman scattering and surface-enhanced infrared absorption*, ACS nano **2** (2008), no. 4, 707–718.

[LF63] IG Lang and Yu A Firsov, *Kinetic theory of semiconductors with low mobility*, Soviet Journal of Experimental and Theoretical Physics **16** (1963), 1301.

[LL60] LD Landau and EM Lifshitz, *Classical mechanics*.

[LLL+09] H Liu, YM Liu, T Li, SM Wang, SN Zhu, and X Zhang, *Coupled magnetic plasmons in metamaterials*, physica status solidi (b) **246** (2009), no. 7, 1397–1406.

[LLSB05] Kuiru Li, Xiangting Li, Mark I Stockman, and David J Bergman, *Surface plasmon amplification by stimulated emission in nanolenses*, Phys. Rev. B **71** (2005), no. 11, 115409.

[Lou00] Rodney Loudon, *The quantum theory of light*, Oxford university press, 2000.

[LPK06] Nanguo Liu, Bradley S Prall, and Victor I Klimov, *Hybrid gold/silica/nanocrystal-quantum-dot superstructures: synthesis and analysis of semiconductor-metal interactions*, Journal of the American Chemical Society **128** (2006), no. 48, 15362–15363.

[LRC+10] Qiang Lin, Jessie Rosenberg, Darrick Chang, Ryan Camacho, Matt Eichenfield, Kerry J Vahala, and Oskar Painter, *Coherent mixing of mechanical excitations in nano-optomechanical structures*, Nature Photonics **4** (2010), no. 4, 236–242.

[LŠ76] Z Lenac and M Šunjić, *Quantum-mechanical approach to the point-charge capacitor problem*, Il Nuovo Cimento B Series 11 **33** (1976), no. 2, 681–698.

[LTLL12] Changhyoup Lee, Mark Tame, James Lim, and Jinhyoung Lee, *Quantum plasmonics with a metal nanoparticle array*, Physical Review A **85** (2012), no. 6, 063823.

[Luc79] AA Lucas, *Self-image excitation mechanism for fast ions scattered by metal surfaces at grazing incidence*, Physical Review B **20** (1979), no. 12, 4990.

[LWM+09] Na Liu, Thomas Weiss, Martin Mesch, Lutz Langguth, Ulrike Eigenthaler, Michael Hirscher, Carsten So nnichsen, and Harald Giessen, *Planar metamaterial analogue of electromagnetically induced transparency for plasmonic sensing*, Nano letters **10** (2009), no. 4, 1103–1107.

[Mah00] Gerald D Mahan, *Many particle physics*.

[Mah10] GD Mahan, *Quantization of surface polaritons*, Physical Review B **82** (2010), no. 16, 165318.

[Mah12] ———, *Image potential from a free electron metal*, Surface Science **606** (2012), no. 19, 1542–1549.

[Mai07] Stefan A Maier, *Plasmonics: fundamentals and applications*.

[MAN11] Alejandro Manjavacas, FJ Garci a de Abajo, and Peter Nordlander, *Quantum plexcitonics: strongly interacting plasmons and excitons*, Nano letters **11** (2011), no. 6, 2318–2323.

[MGMM12] Fabian Mohn, Leo Gross, Nikolaj Moll, and Gerhard Meyer, *Imaging the charge distribution within a single molecule*, Nature nanotechnology **7** (2012), no. 4, 227–231.

[Mie08] Gustav Mie, *Beiträge zur optik trüber medien, speziell kolloidaler metallösungen*, Annalen der physik **330** (1908), no. 3, 377–445.

[Mil77] DL Mills, *Image force on a moving charge*, Physical Review B **15** (1977), no. 2, 763.

[MKN+12] DC Marinica, AK Kazansky, Peter Nordlander, Javier Aizpurua, and Andrei G Borisov, *Quantum plasmonics: Nonlinear effects in the field enhancement of a plasmonic nanoparticle dimer*, Nano letters **12** (2012), no. 3, 1333–1339.

[MKZ+08] Jörg Merlein, Matthias Kahl, Annika Zuschlag, Alexander Sell, Andreas Halm, Johannes Boneberg, Paul Leiderer, Alfred Leitenstorfer, and Rudolf Bratschitsch, *Nanomechanical control of an optical antenna*, Nature Photonics **2** (2008), no. 4, 230–233.

[MML+69] AU MacRae, K Müller, JJ Lander, J Morrison, and JC Phillips, *Electronic and lattice structure of cesium films adsorbed on tungsten*, Physical Review Letters **22** (1969), no. 20, 1048.

[MNMI09] Sadahiro Masuo, Hiroyuki Naiki, Shinjiro Machida, and Akira Itaya, *Photon statistics in enhanced fluorescence from a single cdse/zns quantum dot in the vicinity of silver nanoparticles*, Applied Physics Letters **95** (2009), no. 19, 193106–193106.

[Mor81] Feshbach Morse, *Methods of theoretical physics (2-volume set)*.

[MPP86] J Mahanty, KN Pathak, and VV Paranjape, *Self-energy of a moving charge in the presence of a metal surface*, Physical Review B **33** (1986), no. 4, 2333.

[MR81] JR Manson and RH Ritchie, *Self-energy of a charge near a surface*, Physical Review B **24** (1981), no. 8, 4867.

[Muk99] Shaul Mukamel, *Principles of nonlinear optical spectroscopy (oxford series on optical and imaging sciences)*.

[NE97] Shuming Nie and Steven R Emory, *Probing single molecules and single nanoparticles by surface-enhanced raman scattering*, science **275** (1997), no. 5303, 1102–1106.

[NEC70] K. L. Ngai, E. N. Economou, and Morrel H. Cohen, *Theory of surface plasmon excitation in low-energy electron diffraction and in photoemission*, Phys. Rev. Lett. **24** (1970), 61–64.

[NH78] RM Nieminen and CH Hodges, *Plasmon model for image-potential-induced surface states with an application to positrons at metal surfaces*, Physical Review B **18** (1978), no. 6, 2568.

[NH12] Lukas Novotny and Bert Hecht, *Principles of nano-optics*.

[NLON09] Prashant Nagpal, Nathan C Lindquist, Sang-Hyun Oh, and David J Norris, *Ultrasmooth patterned metals for plasmonics and metamaterials*, Science **325** (2009), no. 5940, 594–597.

[NP58] Philippe Nozieres and David Pines, *Electron interaction in solids. general formulation*, Physical Review **109** (1958), no. 3, 741.

[PB52] David Pines and David Bohm, *A collective description of electron interactions: Ii. collective* vs *individual particle aspects of the interactions*, Phys. Rev. **85** (1952), 338–353.

[PGC+13] Young-Shin Park, Yagnaseni Ghosh, Yongfen Chen, Andrei Piryatinski, Ping Xu, Nathan H Mack, Hsing-Lin Wang, Victor I Klimov, Jennifer A Hollingsworth, and Han Htoon, *Super-poissonian statistics of photon emission from single cdse-cds core-shell nanocrystals coupled to metal nanostructures*, Physical Review Letters **110** (2013), no. 11, 117401.

[Pin56] David Pines, *Collective energy losses in solids*, Rev. Mod. Phys. **28** (1956), 184–198.

[Pow68] CJ Powell, *Characteristic energy losses of 8-kev electrons in liquid al, bi, in, ga, hg, and au*, Physical Review **175** (1968), no. 3, 972.

[PRHN03] E Prodan, C Radloff, NJ Halas, and P Nordlander, *A hybridization model for the plasmon response of complex nanostructures*, Science **302** (2003), no. 5644, 419–422.

[PS59a] C. J. Powell and J. B. Swan, *Origin of the characteristic electron energy losses in aluminum*, Phys. Rev. **115** (1959), 869–875.

[PS59b] ———, *Origin of the characteristic electron energy losses in magnesium*, Phys. Rev. **116** (1959), 81–83.

[PS09] Vitaliy N Pustovit and Tigran V Shahbazyan, *Cooperative emission of light by an ensemble of dipoles near a metal nanoparticle: The plasmonic dicke effect*, Physical review letters **102** (2009), no. 7, 077401.

[PS10] ———, *Plasmon-mediated superradiance near metal nanostructures*, Physical Review B **82** (2010), no. 7, 075429.

[PS11] ———, *Resonance energy transfer near metal nanostructures mediated by surface plasmons*, Physical Review B **83** (2011), no. 8, 085427.

[PSCE07] JM Pitarke, VM Silkin, EV Chulkov, and PM Echenique, *Theory of surface plasmons and surface-plasmon polaritons*, Reports on progress in physics **70** (2007), no. 1, 1.

[RACH68] RH Ritchie, ET Arakawa, JJ Cowan, and RN Hamm, *Surface-plasmon resonance effect in grating diffraction*, Physical Review Letters **21** (1968), no. 22, 1530.

[Rae67] H Raether, *Surface plasma oscillations as a tool for surface examinations*, Surface Science **8** (1967), no. 1, 233–246.

[RCDP14] Oleksiy Roslyak, Charles Cherqui, DH Dunlap, and Andrei Piryatinski, *Effect of localized surface-plasmon mode on exciton transport and radiation emission in carbon nanotubes*, Journal of Physical Chmistry B (submitted) (2014).

[RCJ11] Alejandro W Rodriguez, Federico Capasso, and Steven G Johnson, *The casimir effect in microstructured geometries*, Nature photonics **5** (2011), no. 4, 211–221.

[RDSF+10] A Ridolfo, O Di Stefano, N Fina, R Saija, and S Savasta, *Quantum plasmonics with quantum dot-metal nanoparticle molecules: influence of the fano effect on photon statistics*, Physical review letters **105** (2010), no. 26, 263601.

[Rit57] R. H. Ritchie, *Plasma losses by fast electrons in thin films*, Phys. Rev. **106** (1957), 874–881.

[Rit72] RH Ritchie, *Surface plasmons and the image force in metals*, Physics Letters A **38** (1972), no. 3, 189–190.

[RM72] R Ray and GD Mahan, *Dynamical image charge theory*, Physics Letters A **42** (1972), no. 4, 301–302.

[Rut42] Gerhard Ruthemann, *Elektronenbremsung an röntgenniveaus*, Naturwissenschaften **30** (1942), no. 9, 145–145.

[Rut48] _____, *Elektronenbremsung an röntgenniveaus*, Annalen der Physik **437** (1948), no. 3-4, 135–146.

[SAI13] René IP Sedmik, Attaallah Almasi, and Davide Iannuzzi, *Locality of surface interactions on colloidal probes*, Physical Review B **88** (2013), no. 16, 165429.

[SDMT98] Julian Seymour Schwinger, Lester L DeRaad, Kimball A Milton, and Wu-yang Tsai, *Classical electrodynamics*.

[SF60] E. A. Stern and R. A. Ferrell, *Surface plasma oscillations of a degenerate electron gas*, Phys. Rev. **120** (1960), 130–136.

[SFB02] Mark I Stockman, Sergey V Faleev, and David J Bergman, *Coherent control of femtosecond energy localization in nanosystems*, Physical review letters **88** (2002), no. 6, 067402.

[SGEKD13] Jonathan A Scholl, Aitzol García-Etxarri, Ai Leen Koh, and Jennifer A Dionne, *Observation of quantum tunneling between two plasmonic nanoparticles*, Nano letters **13** (2013), no. 2, 564–569.

[SHE+12] Kevin J Savage, Matthew M Hawkeye, Rubén Esteban, Andrei G Borisov, Javier Aizpurua, and Jeremy J Baumberg, *Revealing the quantum regime in tunnelling plasmonics*, Nature **491** (2012), no. 7425, 574–577.

[SKB+06] Y Sugawara, TA Kelf, JJ Baumberg, ME Abdelsalam, and PN Bartlett, *Strong coupling between localized plasmons and organic excitons in metal nanovoids*, Physical review letters **97** (2006), no. 26, 266808.

[SKD12] Jonathan A Scholl, Ai Leen Koh, and Jennifer A Dionne, *Quantum plasmon resonances of individual metallic nanoparticles*, Nature **483** (2012), no. 7390, 421–427.

[SMNG12] Peng Song, Sheng Meng, Peter Nordlander, and Shiwu Gao, *Quantum plasmonics: Symmetry-dependent plasmon-molecule coupling and quantized photoconductances*, Physical Review B **86** (2012), no. 12, 121410.

[SMPP91] B Singla, MR Monga, KN Pathak, and VV Paranjape, *Self-energy of a moving charged particle in the presence of a metal surface*, Physical Review B **44** (1991), no. 16, 9012.

[SOF67] JB Swan, A Otto, and H Fellenzer, *Observed retardation effects on the energy of the $\omega+$-surface plasmons in thin aluminium foils*, physica status solidi (b) **23** (1967), no. 1, 171–176.

[Som16] Arnold Sommerfeld, *Zur quantentheorie der spektrallinien*, Annalen der Physik **356** (1916), no. 17, 1–94.

[Sön01] Carsten Sönnichsen, *Plasmons in metal nanostructures*.

[SS69] Neville V Smith and William E Spicer, *Photoemission observation of surface-plasmon excitation in the alkali metals*, Physical Review Letters **23** (1969), no. 14, 769.

[SSS94] Ramamurti Shankar, Ravi Shankar, and Ramamurti Shankar, *Principles of quantum mechanics*.

[Sta70] JL Stanford, *Determination of surface-film thickness from shift of optically excited surface plasma resonance*, JOSA **60** (1970), no. 1, 49–53.

[ŠTL72] M Šunjic, G Toulouse, and AA Lucas, *Dynamical corrections to the image potential*, Solid State Communications **11** (1972), no. 12, 1629–1631.

[Sto08] Mark I Stockman, *Spasers explained*, Nature Photonics **2** (2008), no. 6, 327–329.

[Sto11] ———, *Nanoplasmonics: past, present, and glimpse into future*, Optics express **19** (2011), no. 22, 22029–22106.

[Str07] Julius Adams Stratton, *Electromagnetic theory*.

[Sun72] M Sunjic, *Dynamical corrections to the image potential*, Solid State Communications **11** (1972), 1629–1631.

[THW+13] Lars Thylenai, Petter Holmstrtima, Lech Wosinskiaic, Bozena Iaskorzynskaa, Makoto Narused'e, Tadashi Kawazoeeif, Motoichi OhIsue, Min Yana, Marco Fiorentino, and Urban Westergrena, *Nanophotonics for lovv-fovver switches*, Optical Fiber Telecommunications Volume VIA: Components and Subsystems (2013), 205.

[TKB79] JC Tsang, JR Kirtley, and JA Bradley, *Surface-enhanced raman spectroscopy and surface plasmons*, Physical Review Letters **43** (1979), 772–775.

[TMÖ+13] MS Tame, KR McEnery, ŞK Özdemir, J Lee, SA Maier, and MS Kim, *Quantum plasmonics*, Nature Physics **9** (2013), no. 6, 329–340.

[VAP+12] Aleksei Perovich Vinogradov, Evgenii Sergeevich Andrianov, Aleksandr Aleksandrovich Pukhov, Aleksandr Viktorovich Dorofeenko, and AA Lisyansky, *Quantum plasmonics of metamaterials: loss compensation using spasers*, Physics-Uspekhi **55** (2012), no. 10, 1046–1053.

[VK95] M Vollmer and U Kreibig, *Optical properties of metal clusters*, Springer Ser. Mat. Sci **25** (1995).

[VW06] Werner Vogel and Dirk-Gunnar Welsch, *Quantum optics*, John Wiley & Sons, 2006.

[Wag86] Max Wagner, *Unitary transformations in solid state physics*.

[Wil15] William Wilson, *Lxxxiii. the quantum-theory of radiation and line spectra*, The London, Edinburgh, and Dublin Philosophical Magazine and Journal of Science **29** (1915), no. 174, 795–802.

[WIN+10] Paul R West, Satoshi Ishii, Gururaj V Naik, Naresh K Emani, Vladimir M Shalaev, and Alexandra Boltasseva, *Searching for better plasmonic materials*, Laser & Photonics Reviews **4** (2010), no. 6, 795–808.

[WS10] Edo Waks and Deepak Sridharan, *Cavity qed treatment of interactions between a metal nanoparticle and a dipole emitter*, Physical Review A **82** (2010), no. 4, 043845.

[YLZ+13] Hugen Yan, Tony Low, Wenjuan Zhu, Yanqing Wu, Marcus Freitag, Xuesong Li, Francisco Guinea, Phaedon Avouris, and Fengnian Xia, *Damping pathways of mid-infrared plasmons in graphene nanostructures*, Nature Photonics **7** (2013), no. 5, 394–399.

[ZGB06] Wei Zhang, Alexander O Govorov, and Garnett W Bryant, *Semiconductor-metal nanoparticle molecules: hybrid excitons and the nonlinear fano effect*, Physical review letters **97** (2006), no. 14, 146804.

[ZGW+08] Shuang Zhang, Dentcho A Genov, Yuan Wang, Ming Liu, and Xiang Zhang, *Plasmon-induced transparency in metamaterials*, Physical Review Letters **101** (2008), no. 4, 47401.

[ZLS+13] Tianyue ZHANG, Guowei LU, Hongming SHEN, Jie LIU, and Qihuang GONG, *Bright fluorescent probe based on plasmonic enhanced two-photon fluorescence with gold nanoshells*.

[ZPN10] Jorge Zuloaga, Emil Prodan, and Peter Nordlander, *Quantum plasmonics: optical properties and tunability of metallic nanorods*, ACS nano **4** (2010), no. 9, 5269–5276.

[ZRM89] Xiang-Yang Zheng, RH Ritchie, and JR Manson, *High-order corrections to the image potential*, Physical Review B **39** (1989), 79120–13513.

[Zwa70] Robert Zwanzig, *Dielectric friction on a moving ion. ii. revised theory*, The Journal of Chemical Physics **52** (1970), 3625.